



HAL
open science

Guidance of radioembolization procedures in the context of interventional oncology

Houda Hammami

► **To cite this version:**

Houda Hammami. Guidance of radioembolization procedures in the context of interventional oncology. Other. Université de Rennes, 2021. English. NNT : 2021REN1S121 . tel-03707320

HAL Id: tel-03707320

<https://theses.hal.science/tel-03707320v1>

Submitted on 28 Jun 2022

HAL is a multi-disciplinary open access archive for the deposit and dissemination of scientific research documents, whether they are published or not. The documents may come from teaching and research institutions in France or abroad, or from public or private research centers.

L'archive ouverte pluridisciplinaire **HAL**, est destinée au dépôt et à la diffusion de documents scientifiques de niveau recherche, publiés ou non, émanant des établissements d'enseignement et de recherche français ou étrangers, des laboratoires publics ou privés.

THESE DE DOCTORAT DE

L'UNIVERSITE DE RENNES 1

ECOLE DOCTORALE N° 601
*Mathématiques et Sciences et Technologies
de l'Information et de la Communication*
Spécialité : *Signal, Image, Vision*

Par

Houda HAMMAMI

Guidance of radioembolization procedures in the context of interventional oncology

Thèse présentée et soutenue à Rennes, le 16 décembre 2021
Unité de recherche : LTSI INSERM U1099
Thèse N° :

Rapporteurs avant soutenance :

Céline FOUARD MCU, TIMC-GMCAO, Université Grenoble Alpes, La Tronche, France
Christophe LOHOU PR, Institut Pascal, IUT Clermont Auvergne, Le Puy-En-Velay, France

Composition du Jury :

Président :

Examineurs :	Céline FOUARD	MCU, TIMC-GMCAO, Université Grenoble Alpes, La Tronche, France
	Christophe LOHOU	PR, Institut Pascal, IUT Clermont Auvergne, Le Puy-En-Velay, France
	Jérôme SZEWCZYK	PR, ISIR, Sorbonne Universités – UPMC, Paris, France
	Yan ROLLAND	MD, PhD, LTSI, Centre Eugène Marquis, Rennes, France
Dir. de thèse :	Pascal HAIGRON	PR, LTSI, Université de Rennes 1. Rennes, France.
Co-dir. de thèse :	Antoine PETIT	Ingénieur R&D, Société Therenva SAS, Rennes, France

ACKNOWLEDGEMENTS

LIST OF FIGURES.....	7
LIST OF TABLES	14
LIST OF ABBREVIATIONS	15
Résumé long en français	17
Introduction	25
1 Computer-assisted radioembolization: clinical context & proposed approach.....	27
1.1 Clinical context	28
1.1.1 Liver anatomy	28
1.1.2 Liver cancer & treatment.....	34
1.2 Image-guided radioembolization.....	37
1.2.1 Transarterial radioembolization	37
1.2.2 Typical radioembolization image guidance	39
1.3 Proposed approach	43
2 Pretreatment assessment intervention guidance.....	47
2.1 Registration approach.....	48
2.1.1 2D/3D Registration	50
2.1.2 Proposed multiresolution intensity-based registration	53
2.2 Celiac trunk access	56
2.2.1 Experiments.....	57
2.2.2 Results	59
2.3 Injection site access.....	61
2.3.1 Experiments.....	63
2.3.2 Results	65
2.4 Discussion and conclusion	67

3 Treatment intervention guidance: injection site reproduction.....	71
3.1 2D/2D Registration approach.....	72
3.2 Experiments.....	77
3.3 Results	78
3.4 Discussion and conclusion	81
4 Hepatic arterial tree repositioning	83
4.1 Dynamic roadmap correction	84
4.1.1 Related works	85
4.1.2 Liver motion and arterial deformation	87
4.2 Catheter tip tracking	88
4.2.1 Approximation of vessel motion by catheter motion	88
4.2.2 Interventional tools tracking.....	90
4.2.3 A CNN based tracking	91
4.3 Experiments.....	93
4.3.1 Catheter tip detection evaluation metric.....	93
4.3.2 Hepatic arterial tree repositioning assessment	94
4.4 Results	95
4.4.1 Clinical data and dataset composition.....	95
4.4.2 Catheter tip detection	96
4.4.3 Hepatic arterial repositioning	103
4.5 Conclusion.....	106
Conclusion and perspectives	107
Published Papers	111
Bibliography.....	113

LIST OF FIGURES

Figure 1 – Guidage assisté par ordinateur. Le volume CTA préopératoire est segmenté semi-automatiquement à l'aide d'endosize®, obtenant soit un volume osseux 3D, soit un volume vasculaire délimité. Au cours de l'intervention de prétraitement, le CTA est d'abord aligné avec l'image fluoroscopique temps réel suivant un recalage osseux 3D/2D (a), et l'aorte abdominale (AA) ainsi que les origines du tronc cœliaque et mésentérique supérieure sont projetés pour aider l'accès au tronc cœliaque (b). Au niveau du tronc cœliaque, un produit de contraste est injecté et une angiographie est acquise et alignée au CTA à travers un recalage vasculaire (c), et l'arbre artériel hépatique est projeté pour aider l'accès au site d'injection (d). Une fois atteint le site d'injection, une image fluoroscopique est capturée (e), et ultérieurement alignée avec l'image fluoroscopique pendant l'intervention de traitement, pour aider la reproduction du site d'injection (f, g). 19

Figure 2 - Évaluation de l'accès au tronc cœliaque pour deux cas de patients différents. Le volume CTA préopératoire est aligné avec l'image fluoroscopique peropératoire au moyen d'un recalage osseux (a) (d). La projection de l'aorte abdominale et des branches latérales (b) (e) entraîne un chevauchement de l'ostium du tronc cœliaque et du cathéter dans le premier cas (c) alors qu'un léger décalage entre les deux composantes est noté dans le second cas (f). 20

Figure 3 - L'angiographie (a) et l'arbre artériel hépatique sont alignés suivant un recalage vasculaire basé-intensité (b). Une bonne correspondance anatomique est obtenue lors de la projection de l'arbre artériel hépatique (c). 21

Figure 4 - Recalage 2D/2D et évaluation basée sur des marqueurs. La fluoroscopie de prétraitement capturée une fois que le cathéter a atteint le site d'injection (a) est alignée sur l'image fluoroscopique peropératoire de traitement (b). Ce recalage aide la reproduction du trajet du cathéter ainsi que le site d'injection (c). Les points marqués (points de couleur

<i>rouge dans (a) et points de couleur bleue dans (b)) qui sont définis par l'expert et utilisés pour l'évaluation sont visualisés dans les images.</i>	<i>23</i>
<i>Figure 5 - Ligamentous attachments of the liver</i>	<i>30</i>
<i>Figure 6 - Anterior and posterior surfaces of liver illustrating functional division of the liver following Couinaud's segmental classification (from [4])......</i>	<i>31</i>
<i>Figure 7 - Blood supply of the liver (from [5]).</i>	<i>32</i>
<i>Figure 8 - Portal vein anatomy. The portal vein is formed by the confluence of the splenic and superior mesenteric veins. The inferior mesenteric vein drains into the splenic vein. The coronary (left gastric) vein drains into the portal vein in the vicinity of the confluence. v. = vein (from [4]).</i>	<i>33</i>
<i>Figure 9 – Arterial anatomy of the upper abdomen and liver, including the celiac trunk and hepatic artery branches. LHA = left hepatic artery; RHA = right hepatic artery (from [4])...</i>	<i>34</i>
<i>Figure 10 - Radioembolization intervention overview (inspired by [29]).</i>	<i>39</i>
<i>Figure 11 - Radioembolization image guidance.</i>	<i>40</i>
<i>Figure 12 - Interventional radiology suite (from [32]).</i>	<i>41</i>
<i>Figure 13 – Proposed navigation system. During pretreatment intervention, the preoperative arterial phase Computed Tomography (CTA) images (a) are firstly registered to the real-time fluoroscopic image (b), and the abdominal aorta (AA) as well as the celiac trunk and the superior mesenteric origins are projected to assess the celiac trunk catheterization (c). At the level of the celiac trunk, a contrast product is injected and a DSA is acquired (d) and registered to the CTA based on a delimited vascular-structure, and the hepatic arterial tree is projected to assess the IS access (e). Once reaching the IS, a fluoroscopic image is captured (f), and registered to the real time fluoroscopic image (g) during the treatment intervention, to assess the IS reproduction (h)......</i>	<i>46</i>
<i>Figure 14 - Early arterial phase CT images are post processed on an independent workstation by semiautomatic segmentation, obtaining the VR model of abdominal aorta and splanchnic arteries (A). The 3Dmodel is then manually registered to the real-time</i>	

List of figures

fluoroscopic image using the bone structures as reference (B), and it is used to catheterize the celiac trunk (C) and the proper hepatic artery (D, E). Only at this time is 3 mL of contrast medium injected to check the correct catheter position (F). It is possible to notice how the VR model allows visualizing the hepatic structure, not enhanced in 2D fluoroscopic images. From [57]..... 49

Figure 15 - EndoNaut® navigation device, THERENVA. 50

Figure 16 - Intensity-based registration framework with its main components. Preoperative arterial phase Computed Tomography (CTA) images are semi-automatically segmented using endosize®, obtaining either a 3D bony-structure or delimited vascular-structure (1). DRR image is generated from the preprocessed volume (2) and compared to the 2D intraoperative image through a similarity metric presenting a quantitative criterion describing how well the input images are similar (3). For optimization, the 3D volume is intermediately transformed following an exhaustive search and the transformation result is progressively refined following a multiresolution scheme (4). The final 3D/2D transformation corresponds to the transformation giving the best achieved similarity measure (5)..... 53

Figure 17 - An exmple of preoperative CTA (a) segmentation. The bone structure extracted from CTA (b) corresponds to the anatomical structure visible in intraoperative fluoroscopic image (c), while the vascular structure extracted from CTA (d) corresponds to the anatomical structure visible in intraoperative angiography (e)..... 54

Figure 18 - preoperative CTA segmentation using Endosize®, sizing software, THERENVA. The segmentation process takes about 10 min. 54

*Figure 19 - Geometric configuration used for registration. **Sw** is the world coordinate system, **Si** is the intraoperative image coordinate system, **Sv** is the preoperative volume coordinate system and **Sa** is the coordinate system where: **Oxz** is the plane parallel to the plane of intraoperative image and **Oy** is aligned with the main axis of c-arm. **tx** and **tz** correspond to in-plane translations and **ty** corresponds to the out-plane translation (along the axes of **Sa**). **rx** and **rz** correspond to the out-plane rotations and **ry** corresponds to the in-plane rotation (around the axes of **Sa**).....* 56

Figure 20 - Boxplot of the mean errors obtained with each SM for 20 patient cases 60

Figure 21 - Celiac trunk access assessment for two different patient cases. Preoperative CTAs are registered to intraoperative fluoroscopic images based on bony-structures (a) (d). The projection of AA and side branches (b) (e) results in a celiac trunk ostium and catheter overlap in the first case (c) whereas a slight shift between the two components is noticed in the second case (f). 61

Figure 22 - Preoperative and intraoperative vascular-structure visualization for a typical patient case. To access the IS, several fluoroscopic images showing incomplete vasculature are acquired with contrast injection at different locations of the catheter tip: i1 (celiac trunk origin), i2 (proper hepatic artery) and i3 (right hepatic artery) (a). A more complete vasculature is visualized in the CTA extracted volume (b). 62

Figure 23 - Three dimensional volume-rendering (3D VR) generated from CTA showing the hepatic arterial anatomic structures. CHA = common hepatic artery, GDA = gastroduodenal artery, PHA = proper hepatic artery, LHA = left hepatic artery and RHA = right hepatic artery 64

Figure 24 - Boxplot of the mean errors obtained with each SM considering only HVS for the 19 patient cases 65

Figure 25 - Influence of the SM on vessel-based registration. The DSA (a) and the HVS are correctly registered with GD (b). A good anatomical correspondence is obtained when projecting the hepatic arterial tree (c). The registration result is degraded with NCC (d). ... 67

Figure 26 - Injection site reproduction in treatment intervention. 73

Figure 27 - Injection site reproduction strategy. 74

Figure 28 - Intensity-based registration framework with its main components. 2D pretreatment assessment and treatment fluoroscopic images are enhanced through preprocessing (1). 2D pretreatment assessment fluoroscopy is compared to the 2D intraoperative treatment fluoroscopy through a similarity metric presenting a quantitative criterion describing how well the input images are similar (2). For optimization, the 2D

List of figures

pretreatment assessment fluoroscopy is intermediately transformed following an exhaustive search and the transformation result is progressively refined following a multiresolution scheme (3). The final 2D/2D transformation corresponds to the transformation giving the best achieved similarity measure (4)..... 76

Figure 29 - Boxplot of the mean landmark errors obtained with GD for image-based registrations 79

Figure 30 - Marked-based evaluation. Pretreatment assessment fluoroscopy captured once the catheter reached the injection site (a) is registered to the intraoperative real-time fluoroscopic image (b) during the treatment intervention. The registration results in a reproduction of the catheter path as well as the IS (c). Marked points (red colored points in (a) and blue colored points in (b)) which are defined by expert are highlighted in the images 80

Figure 31 - Pretreatment catheter path reproduced in treatment fluoroscopic image. Intraoperative real-time fluoroscopic image (left) is augmented with the pretreatment catheter segmented from the transformed preoperative fluoroscopy (right) 80

Figure 32 – Overview of proposed navigation approach. Preoperative arterial phase Computed Tomography (CTA) images are semi-automatically segmented using endosize®, obtaining either a 3D bony or delimited vascular volume. During pre-treatment intervention, the CTA is firstly registered to the real-time fluoroscopic image based on the bony-structure (a), and the abdominal aorta (AA) as well as the celiac trunk and the superior mesenteric origins are projected to assess the celiac trunk catheterization (b). At the level of the celiac trunk, a contrast product is injected and a DSA is acquired and registered to the CTA based on a delimited vascular-structure (c), and the hepatic arterial tree is projected to assess the IS access (d). Once reaching the IS, a fluoroscopic image is captured (e), and registered to the real time fluoroscopic image during the treatment intervention, to assess the IS reproduction (f, g)..... 82

Figure 33 – Global overview: vessels/catheter extraction and 2D/3D registration. From [29]. 86

<i>Figure 34 - roadmap correction for hepatic artery catheterizations. (a) displays the 3D static roadmap of the hepatic arteries. (b) shows a 2D fluoroscopy image. (c) illustrates the projection of 3D static roadmap onto a frame in the 2D fluoroscopy image sequence without motion correction. (d) indicates the projection of 3D static roadmap onto the frame with motion correction. From [62].</i>	86
<i>Figure 35 - Patient and C-arm positioning during radioembolization procedure. From [98].</i>	88
<i>Figure 36 – Liver catheterization procedure in radioembolization</i>	89
<i>Figure 37 - X-Ray fluoroscopy visualizing the guiding catheter in radioembolization</i>	90
<i>Figure 38 – R-CNN, Fast-RCNN and Faster-RCNN architectures [106]–[108].</i>	92
<i>Figure 39 – Object detection using YOLO [109].</i>	93
<i>Figure 40 - Intersection over Union (IoU)</i>	94
<i>Figure 41 – Inclusion Rate (IR) calculation in a single frame: micro-catheter used points</i>	95
<i>Figure 42 - image annotation using labeling.</i>	96
<i>Figure 43 - IoU on different frames of sequence RE 01. Blue bounding boxes correspond to the ground truth whereas red bounding boxes correspond to the tracking output.</i>	98
<i>Figure 44 - IoU on different frames of sequence RE 02: Blue bounding boxes correspond to the ground truth whereas red bounding boxes correspond to the tracking output.</i>	99
<i>Figure 45 - examples of non-detected catheter tip in RE 01 (a) and RE 02 (b)</i>	100
<i>Figure 46 - Horizontal displacement of the catheter tip in sequence RE 01: « Frames » axis presents the frame index in which the catheter tip is detected and “pixels” axis presents the catheter tip horizontal position</i>	101
<i>Figure 47 - Vertical displacement of the catheter tip in sequence RE 01: : « Frames » axis presents the frame index in which the catheter tip is detected and “pixels” axis presents the catheter tip vertical position</i>	101

List of figures

Figure 48 - Horizontal displacement of the catheter tip in sequence RE 02: « Frames » axis presents the frame index in which the catheter tip is detected and “pixels” axis presents the catheter tip horizontal position 102

Figure 49 - Vertical displacement of the catheter tip in sequence RE 02: « Frames » axis presents the frame index in which the catheter tip is detected and “pixels” axis presents the catheter tip vertical position 103

Figure 50 – Hepatic vasculature repositioning result on different frames of sequence RE 01 104

Figure 51 - Hepatic vasculature repositioning result on different frames of sequence RE 02 105

LIST OF TABLES

<i>Table 1- Parameters used during the optimization phases (r = resolution of the discretized range of the parameters).....</i>	<i>57</i>
<i>Table 2 - Bone-based registration results using different similarity measures. Global mean error is calculated on registrations obtaining a mean 2D Euclidean distance $< T$</i>	<i>60</i>
<i>Table 3 - Parameters used during the optimization phases (r = resolution of the discretized range of the parameters).....</i>	<i>63</i>
<i>Table 4 - Vessel-based registration results using different similarity measures. Global mean error is calculated on registrations obtaining a mean 2D Euclidean distance $< T$</i>	<i>66</i>
<i>Table 5 - Parameters used during the optimization phases (r = resolution of the discretized range of the parameters).....</i>	<i>77</i>
<i>Table 6 - catheter tip detection results</i>	<i>97</i>

LIST OF ABBREVIATIONS

RE	Radioembolization
^{99m}Tc-MAA	^{99m} Tc macro aggregated albumin
Y90	Yttrium-90
166Ho	Holmium-166
DSA	Digitally Subtracted Angiography
CTA	Computer Tomography Angiography
HVS	hepatic vascular-structure
HVSS	HVS along with the splenic artery
GI	Gradient Information
GD	Gradient Difference
GC	Gradient Correlation
NCC	Normalized Cross Correlation
MI	Mutual Information
GS	Gold Standard
IoU	Intersection Over Union
IR	Inclusion Rate

Résumé long en français

La radioembolisation est une intervention mini-invasive réalisée pour traiter le cancer du foie. Cette thérapie vise à détruire sélectivement les cellules cancéreuses en administrant des microsphères radioactives incorporant soit de l'Yttrium-90 (90Y) soit du Holmium-166 (166Ho). Afin d'optimiser le traitement, la procédure est réalisée en deux séances : intervention de prétraitement et intervention de traitement. L'intervention de prétraitement présente une simulation préalable de traitement. Elle est principalement réalisée pour : localiser le site d'injection, évaluer la distribution intrahépatique des microsphères 90Y/166Ho, détecter le shunt extrahépatique et réaliser une évaluation dosimétrique. L'intervention de traitement est effectuée une à deux semaines après l'intervention de prétraitement pour la délivrance d'une dose appropriée de microsphères 90Y/166Ho dans le site d'injection préalablement localisé.

Lors des deux interventions, les radiologues interventionnels manipulent soigneusement le cathéter sous un guidage fluoroscopique. Les images fluoroscopiques bidimensionnelles utilisées visualisent des informations de base sur l'anatomie du patient (essentiellement la structure osseuse) et les outils d'intervention insérés. Cependant, la visualisation de la structure vasculaire non permanente nécessite l'acquisition répétitive d'angiographies bidimensionnelles réalisées par injection de produit de contraste, dont une dose excessive peut être néfaste pour le patient. En raison de la complexité du système vasculaire hépatique, la manipulation du cathéter reste une tâche difficile pour les radiologues.

Dans cette thèse, nous proposons une stratégie de guidage assistée par ordinateur conçue pour augmenter progressivement l'image fluoroscopique peropératoire avec les informations appropriées. Cette approche est en mesure d'assurer une navigation fiable du cathéter et a le potentiel de réduire non seulement l'administration de produits de contraste, mais aussi le l'exposition aux rayonnements et le temps d'intervention.

Notre approche est conçue pour guider l'intervention de prétraitement et l'intervention de traitement, présentant nos deux premières contributions principales.

Au cours de l'intervention de prétraitement, pour faciliter l'accès au tronc cœliaque, l'aorte et les origines de ses branches latérales sont extraites du volume CTA tridimensionnel préopératoire et projetées sur la fluoroscopie bidimensionnelle peropératoire suivant une méthode de recalage osseux basé-intensité. Par la suite, pour aider à la localisation du site d'injection, une approche similaire consiste à projeter le système vasculaire hépatique du CTA tridimensionnel sur l'angiographie bidimensionnelle peropératoire suivant un recalage vasculaire basé-intensité.

Enfin, pendant l'intervention de traitement, le site d'injection sélectionné lors de l'intervention de prétraitement est reproduit à travers un recalage 2D/2D des images fluoroscopiques de prétraitement et de traitement. Les trois étapes de fusion sont représentées dans (*Figure 1*).

La projection statique de la structure vasculaire hépatique sur l'angiographie peropératoire, notamment illustrée dans (*Figure 1 – (d)*), peut ajouter des informations pertinentes et fournir une visualisation plus complète de la scène chirurgicale dans les procédures de radioembolisation. Les organes abdominaux, y compris le foie, changent continuellement leurs positions en raison de la respiration du patient. Un système de guidage précis doit prendre en considération ce déplacement par une mise à jour continue de l'alignement spatial du système vasculaire hépatique préopératoire avec la position du système vasculaire hépatique peropératoire.

Dans cette thèse, notre troisième contribution principale consiste à présenter une méthode pour mettre à jour la position du système vasculaire 3D projeté en fonction de la détection de l'extrémité du cathéter visualisée en séquence fluoroscopique bidimensionnelle peropératoire. La méthode proposée est basée sur le réseau neuronal convolutif (CNN) et se déroule en temps réel.

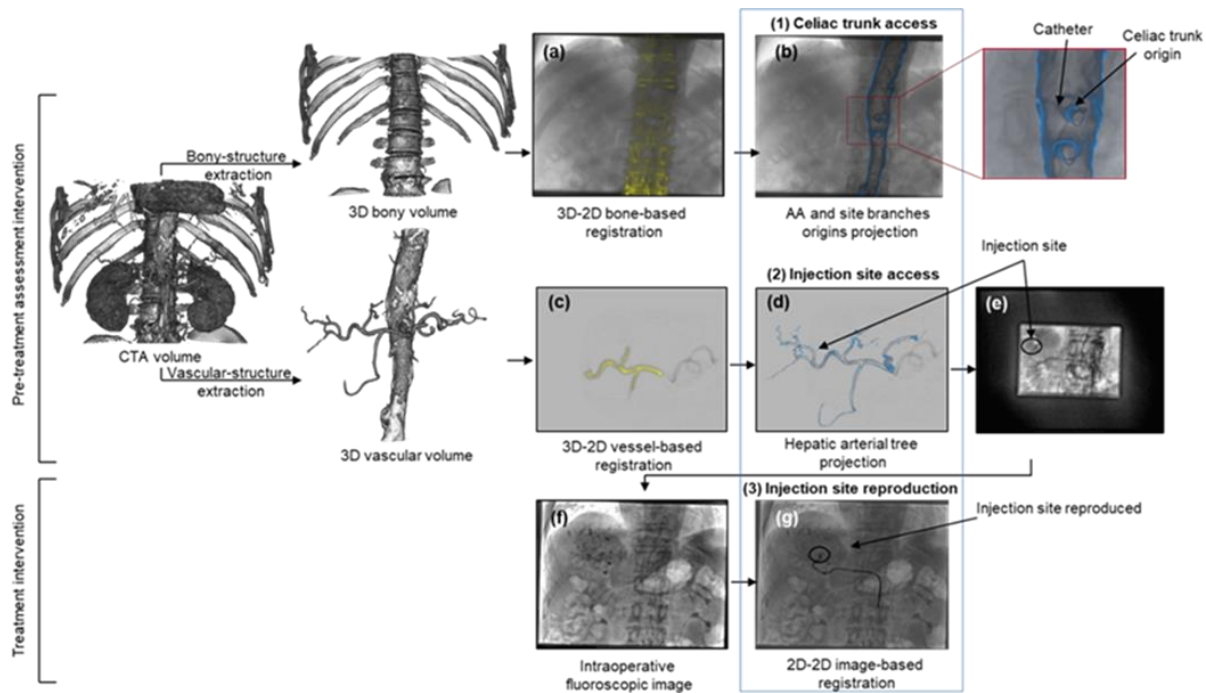


Figure 1 – Guidage assisté par ordinateur. Le volume CTA préopératoire est segmenté semi-automatiquement à l'aide d'Endosize®, obtenant soit un volume osseux 3D, soit un volume vasculaire délimité. Au cours de l'intervention de prétraitement, le CTA est d'abord aligné avec l'image fluoroscopique temps réel suivant un recalage osseux 3D/2D (a), et l'aorte abdominale (AA) ainsi que les origines du tronc cœliaque et mésentérique supérieure sont projetés pour aider l'accès au tronc cœliaque (b). Au niveau du tronc cœliaque, un produit de contraste est injecté et une angiographie est acquise et alignée au CTA à travers un recalage vasculaire (c), et l'arbre artériel hépatique est projeté pour aider l'accès au site d'injection (d). Une fois atteint le site d'injection, une image fluoroscopique est capturée (e), et ultérieurement alignée avec l'image fluoroscopique pendant l'intervention de traitement, pour aider la reproduction du site d'injection (f, g).

• Première contribution: Guidage de l'intervention de prétraitement

L'approche proposée repose sur une méthode de recalage 3D/2D basée intensité, guidée par les structures anatomiques d'intérêt (DRR générée à partir d'un prétraitement de l'image 3D préopératoire) et mettant en œuvre une recherche exhaustive multi résolution. Dans ce contexte, l'exactitude et la précision du recalage (osseux et vasculaire) dépendent de la sélection de la mesure de similarité. Nos expériences ont permis de montrer qu'une mesure de similarité basée sur la différence de gradient est la plus appropriée.

Résumé long en français

Les deux étapes de fusion conçues pour guider l'intervention de prétraitement par l'aide à l'accès au tronc cœliaque et au site d'injection ont été évaluées indépendamment sur des sous-ensembles de 20 et 19 patients, respectivement. L'approche a abouti à des correspondances anatomiques qualitativement appropriées lors de la projection des structures préopératoires sur les images peropératoires. Avec la meilleure configuration, les étapes de recalage ont montré la précision et la faisabilité de l'alignement des données, avec des erreurs moyennes globales de 1,59 mm et 2,32 mm, respectivement, un temps de calcul qui n'a jamais dépassé 5 s et 25 s, respectivement, et une interaction utilisateur limitée à l'initialisation manuelle du recalage 3D/2D. La projection de l'aorte et de la structure vasculaire hépatique, semble être précise pour manipuler le cathéter et, par conséquent, a le potentiel de réduire l'administration de produit de contraste et l'exposition aux rayonnements (*Figure 2 et Figure 3*).

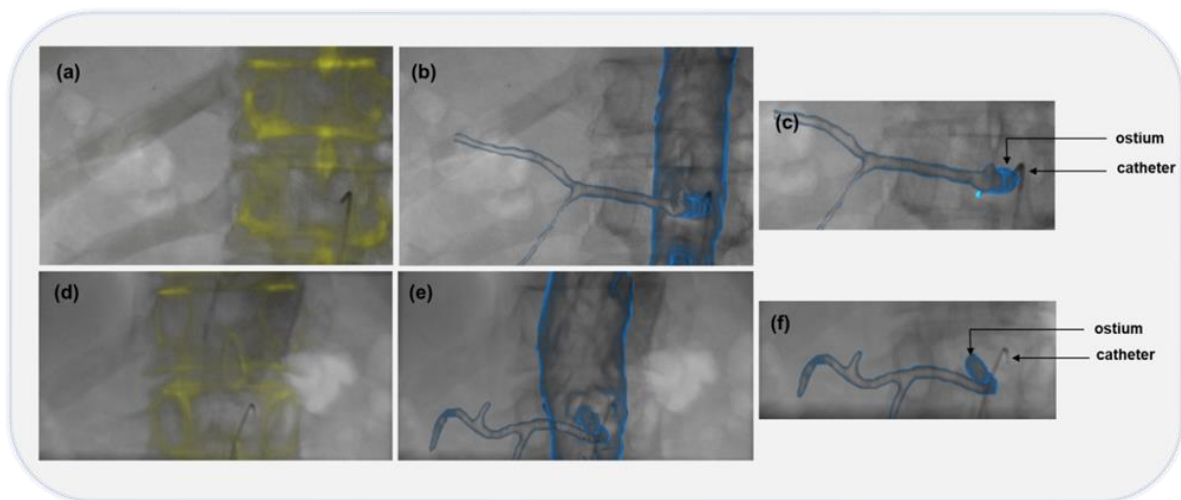


Figure 2 - Évaluation de l'accès au tronc cœliaque pour deux cas de patients différents. Le volume CTA préopératoire est aligné avec l'image fluoroscopique peropératoire au moyen d'un recalage osseux (a) (d). La projection de l'aorte abdominale et des branches latérales (b) (e) entraîne un chevauchement de l'ostium du tronc cœliaque et du cathéter dans le premier cas (c) alors qu'un léger décalage entre les deux composantes est noté dans le second cas (f).

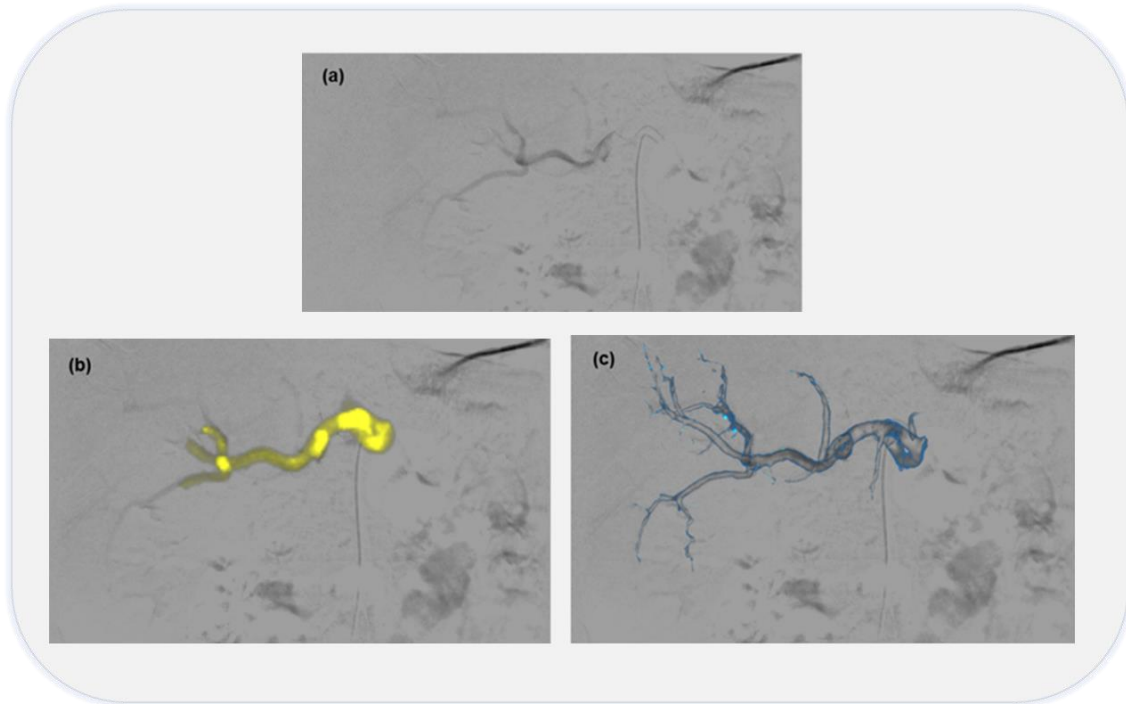


Figure 3 - L'angiographie (a) et l'arbre artériel hépatique sont alignés suivant un recalage vasculaire basé-intensité (b). Une bonne correspondance anatomique est obtenue lors de la projection de l'arbre artériel hépatique (c).

Même si le recalage osseux (*Figure 2*) est effectué avec une erreur de recalage moyenne globale relativement faible, la projection de l'origine du tronc cœliaque peut aussi être inexacte dans certains cas. Nous avons remarqué occasionnellement un léger désalignement entre le tronc cœliaque projeté et le cathéter inséré observé sur l'image fluoroscopique. Cela peut s'expliquer par le repositionnement du patient entraînant un décalage vasculaire. Cette erreur de projection résultante a le potentiel de diminuer la précision de la localisation de la pointe du cathéter. Une solution possible pourrait consister à estimer une plage moyenne de désalignement de l'origine du tronc cœliaque en calculant, pour plusieurs patients, la distance entre l'ostium projeté (appartenant à l'aorte abdominale) et le cathéter 2D visualisé sur l'image fluoroscopique 2D. La marge obtenue pourrait alors être utilisée pour mieux mettre en évidence la zone d'origine du tronc cœliaque où le cathéter doit être inséré.

Concernant l'accès au site d'injection par projection d'arbres hépatiques (*Figure 3*), afin de réaliser correctement la méthode de recalage, il a été remarqué, dans notre étude, qu'il est nécessaire de privilégier les structures préopératoires rigides ainsi que les structures qui apparaissent sur l'image peropératoire. Dans ce contexte, l'approche pourrait être améliorée par une méthode automatique permettant de segmenter uniquement les structures 3D préopératoires visibles sur l'image peropératoire (structures vasculaires injectées).

• **Deuxième contribution : Guidage de l'intervention de traitement**

Reproduire le site d'injection prédéfini avec précision lors de l'intervention de prétraitement est encore une tâche difficile pour les radiologues. En effet, afin d'éviter les écarts de distribution de dose, le site d'injection doit être reproduit le plus fidèlement possible.

Jusqu'à présent, lors de l'intervention de traitement, les radiologues se réfèrent à leur capacité à comprendre le système vasculaire, à manipuler efficacement le cathéter à l'intérieur et à localiser mentalement le site d'injection. Une mauvaise perception peropératoire des structures anatomiques et une reproduction inappropriée de la position du site d'injection peuvent certainement entraîner des écarts de distribution de dose $^{90}\text{Y}/^{166}\text{Ho}$.

La reproduction automatique du site d'injection n'ayant pas été étudiée dans la littérature, dans cette thèse, nous avons étendu notre approche de guidage pour proposer une reproduction automatique de ce site en augmentant l'image fluoroscopique 2D peropératoire du traitement avec le trajet du cathéter extrait de la fluoroscopie de prétraitement au moyen d'un recalage 2D/2D (*Figure 4*). La visualisation du trajet du cathéter pourrait simultanément aider à spécifier la position d'origine du tronc cœliaque et l'emplacement du site d'injection.

Ce recalage 2D/2D de l'image fluoroscopique de prétraitement avec l'image fluoroscopique de traitement a été évalué sur un sous-ensemble de 5 patients. L'approche a montré la précision et la faisabilité de l'alignement des données, avec une erreur moyenne globale de

2,17 mm, un temps de calcul qui n'a jamais dépassé 11 s, de manière complètement automatique (sans aucune interaction avec l'utilisateur).

Dans la plupart des cas, le modèle de transformation rigide 2D/2D s'est avéré suffisant pour le recalage d'images fluoroscopiques de prétraitement et de traitement. La projection du cathéter, semble être précise pour faciliter la manipulation du cathéter et reproduire le site d'injection et donc, réduire l'administration de produit de contraste, l'exposition aux rayonnements et le risque de dépôt inadéquat de $^{90}\text{Y}/^{166}\text{Ho}$.

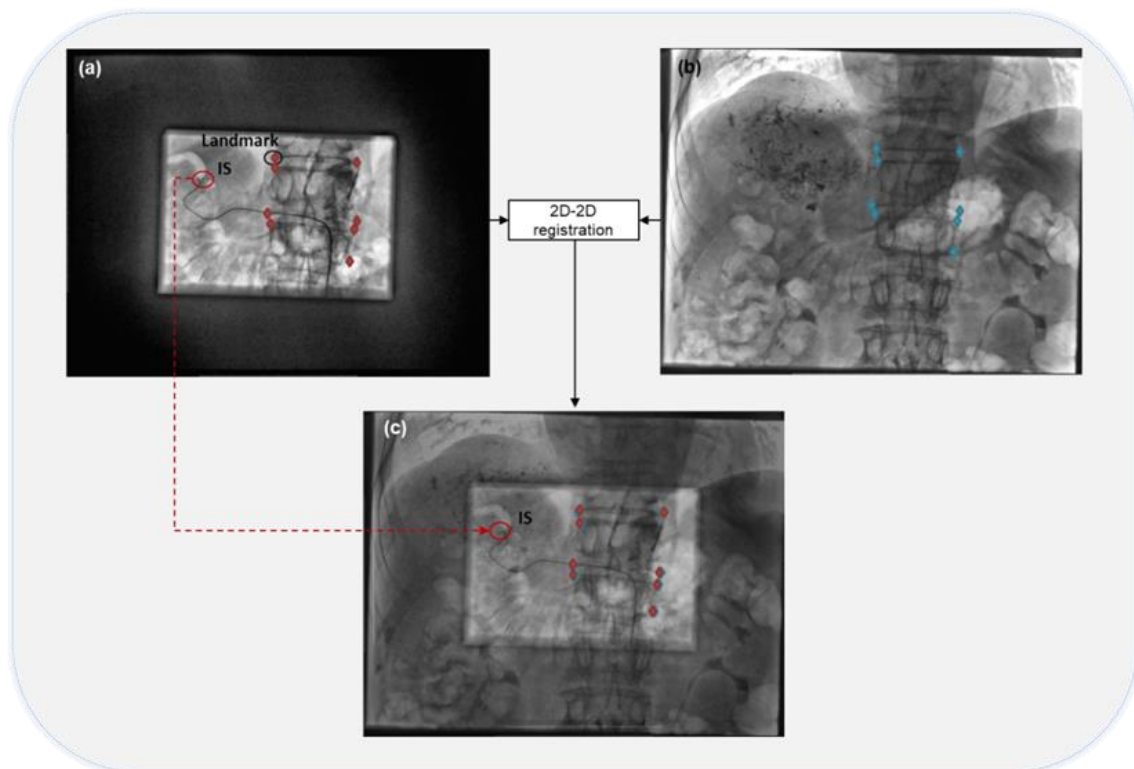


Figure 4 - Recalage 2D/2D et évaluation basée sur des marqueurs. La fluoroscopie de prétraitement capturée une fois que le cathéter a atteint le site d'injection (a) est alignée sur l'image fluoroscopique peropératoire de traitement (b). Ce recalage aide la reproduction du trajet du cathéter ainsi que le site d'injection (c). Les points marqués (points de couleur rouge dans (a) et points de couleur bleue dans (b) qui sont définis par l'expert et utilisés pour l'évaluation sont visualisés dans les images.

• **Troisième contribution : Repositionnement de la structure hépatique projetée**

A ce niveau nous abordons le problème du suivi dynamique de la structure vasculaire sur l'image fluoroscopique augmentée. Afin de repositionner l'arbre artériel hépatique sur la séquence fluoroscopique, la structure vasculaire hépatique préopératoire est tout d'abord alignée avec l'angiographie peropératoire selon la méthode de recalage vasculaire 3D/2D présentée. La structure vasculaire 3D est ensuite projetée sur la séquence fluoroscopique et sa position dans le plan est mise à jour en fonction de l'emplacement 2D de l'extrémité du cathéter. Celle-ci est localisée dans chaque trame de la séquence en utilisant une approche de suivi basée sur un réseau de neurones convolutif (CNN).

Le CNN a été entraîné sur quatre séquences fluoroscopiques et la méthode de suivi proposée a été évaluée sur deux séquences fluoroscopiques réelles de deux patients différents. Dans les deux cas, la méthode de suivi a montré une précision et faisabilité de la détection de l'extrémité du cathéter en temps réel, avec un taux de détection de 87 % et 66 %, un indice de recouvrement de 0,74 et 0,69, et une erreur moyenne de 0,6 mm et 0,69 mm, respectivement. Le repositionnement de l'arbre hépatique a abouti à des correspondances anatomiques appropriées démontrées par un taux d'inclusion rapporté à 90 % et 82 %, respectivement. L'approche globale ne nécessite pas d'interaction manuelle de l'utilisateur.

Ces résultats montrent que la méthode utilisée pour le suivi de l'extrémité du cathéter est robuste, malgré les difficultés liées au manque des caractéristiques discriminantes, le faible contraste et la faible taille de l'extrémité du cathéter. Le repositionnement de l'arbre artériel hépatique a également montré son efficacité. L'approche proposée ne nécessite pas d'injection de produit de contraste / d'images angiographiques 2D ni d'interaction avec l'utilisateur. Elle permet d'intégrer le mouvement lié à la respiration lors de l'augmentation de l'image fluoroscopique peropératoire, et ainsi de faciliter le cathétérisme de l'arbre artériel hépatique lors des procédures de radioembolisation.

Introduction

Minimally invasive interventions include the techniques that limit the size of the incisions and thus reduce the pain, the wound healing time, the associated infection risk[1] and other traditional/ open surgeries related complications. They have proven to be safer and have become increasingly integrated into the regular practice of cardiac, neurological, orthopedic, endovascular, oncological and many other procedures. The advancement of medical technologies, along with refinements in minimally invasive surgery technique, have significantly expanded the scope of this practice over time. In fact, thanks to the availability of interventional imaging, it has become possible for radiologists to manipulate the interventional tools such as catheters and guidewires to access to the region of interest without direct eyesight.

Radioembolization is a minimally-invasive intervention performed to treat liver cancer. This therapy aims to selectively destroy cancer cells by administering radioactive microspheres embedding either Yttrium-90 (90Y) or Holmium-166 (166Ho) while sparing healthy tissue. In order to optimize radioembolization outcomes, the procedure is carried out in two sessions: pretreatment intervention and treatment intervention. The pretreatment assessment intervention is a prior procedure mainly performed to: locate the injection site, assess 90Y/166Ho microspheres intrahepatic distribution, detect extrahepatic shunting and perform dosimetry evaluation. The treatment intervention is performed to inject the estimated proper dose of 90Y/166Ho microspheres in the injection site previously located during the pretreatment intervention.

Due to the hepatic vasculature complexity, interventional radiologists carefully manipulate the catheter, during the two interventions, under intraoperative 2D X-Ray fluoroscopy guidance. Knowing that, this interventional medical imaging modality suffers from lack of information, catheter navigation during both interventions, and more specifically celiac trunk and injection site access, remains a challenging task. In order to highlight vessels, radiologists resort to frequent contrast media injection. Radiation long exposure can

be harmful for both radiologists and patients and contrast media excessive injection can cause severe reactions for the patient.

To plan the intervention, preoperative 3D image modalities visualizing the full hepatic vasculature are acquired some weeks before the intervention. The main objective of this thesis consists in introducing a strategy that may improve image guidance during radioembolization interventions by augmenting intraoperative images by relevant information from preoperative data.

Due to the patient's respiration, the liver changes its position continuously. In this context, we also intend to extend the strategy to a dynamic update of the spatial alignment of the preoperative hepatic vasculature with the intraoperative hepatic vasculature position.

In the first chapter of this thesis we will introduce the clinical context of radioembolization as well as the most prominent challenges that may encounter radiologists during the procedure.

In the second chapter, we address the issue of 3D/2D registration to correctly align and project vascular structures extracted from preoperative CTA onto 2D intraoperative X-Ray images. The proposed registration method is evaluated on clinical data.

The third chapter describes the employment of a 2D/2D image-based registration between pretreatment and treatment fluoroscopic images performed to reproduce the injection site located beforehand during the pretreatment assessment intervention.

The fourth chapter deals with the dynamic overlay of the projected 3D vascular structures on the intraoperative fluoroscopy to improve catheter navigation by integrating the liver motion induced by breathing. To this end, a CNN-based method is more particularly investigated to detect the catheter position in real-time.

Lastly, we summarize our contribution and present perspectives to improve the proposed computer-assisted navigation approach.

1 Computer-assisted radioembolization: clinical context & proposed approach

We present, in this chapter, an overview of the clinical context of radioembolization while describing the liver anatomy, the hepatic cancer development and characteristics, and the radioembolization procedure. Subsequently, we outline a description of radioembolization typical image-based intervention guidance while mentioning the main limits of using fluoroscopic images, to better understand how our guidance strategy could improve the visualization in such procedures. The complete proposed guiding strategy which constitutes the foundation of this thesis is being introduced and depicted at the end of this chapter.

1.1 Clinical context

1.1.1 Liver anatomy

The liver is the largest organ in the human body, accounting for approximately 2% to 3% of average body weight [2]. It is able to perform a wide range of complex and vital functions such as:

- Glycogen storage: excessive entered glucose to the body is stored in the liver as glycogen which can be converted back to glucose and released into the blood when needed (in case of glucose levels fall).
- Bile production: bile is greenish yellow fluid, formed in the liver to aid the small intestine in breaking down and absorbing cholesterol, fats and some vitamins. The bile can be stored in the gallbladder before being released into the small intestine. In this case, it becomes more concentrated, which increases its potency and intensifies its effect.
- Production of certain proteins: the liver produces hundreds of different proteins, each of which has a specific function: prealbumin carries thyroid hormones in the blood, albumin has many functions like providing nourishment of tissues, transferrin presents the principal transport protein for iron, retinol-binding protein is responsible for transporting vitamin A from the liver to other body tissues, etc.
- Blood detoxification and purification: the liver filters the blood by removing toxins and harmful substances like drugs, alcohol etc.

- Immunity: kupffer cells, presenting one of the most important types of liver cells, aid in removing bacteria, worn blood cells, parasites and fungi from the blood.

Anatomical position

The liver mainly covers the right upper quadrant of the abdomen cavity, within the rib cage. More specifically, it lies in the right hypochondriac region, epigastric region and extends to the left hypochondriac region. To maintain its position, the liver is attached to the surrounding structures through peritoneal reflections called ligamentous attachments (*Figure 5*).

Ligaments of the liver

The falciform ligament attaches the anterior surface of the liver to the anterior abdominal wall. The coronary ligament connects the central superior surface of the liver to the interior surface of the diaphragm while delimiting the bare area. As shown in (*Figure 5*), the anterior and posterior layers of the coronary ligament join to form two triangular ligaments located on the lateral borders of the liver. These left and right triangular ligaments attach the upper surface of the left and right lobes of the liver, respectively, to the diaphragm. The liver is connected to the lesser curvature of the stomach and a part of the duodenum by hepatogastric ligament and hepatoduodenal ligament, respectively.

Liver surface

The liver's upper (diaphragmatic) surface is entirely related to the diaphragm and its visceral surface rests against the gallbladder, right kidney and suprarenal gland, stomach, duodenum and the hepatic flexure. The posterior liver surface is in touch with the inferior vena cava and the esophagus.

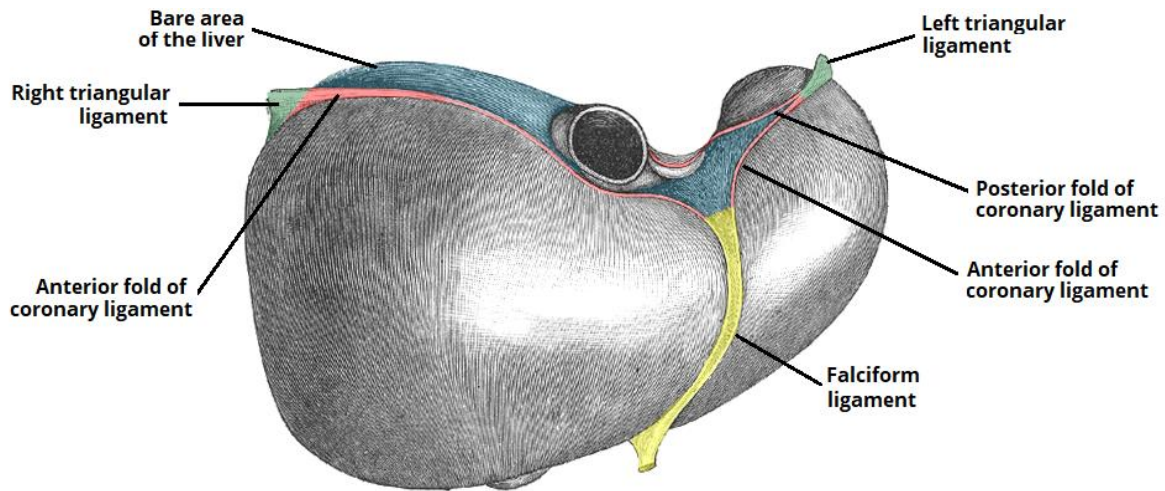


Figure 5 - Ligamentous attachments of the liver. From <https://teachmeanatomy.info/abdomen/viscera/liver/>

Liver structure

The liver is composed of four lobes -the right, left, quadrate and caudate lobe (*Figure 6*). The right and left lobes are the main and largest lobes and are separated by the falciform ligament. The left lobe is 5 to 6 times smaller than the right lobe. The quadrate and caudate lobes are superficial lobes and are located on the posterior underside of the right lobe. The quadrate lobe wraps around the gallbladder and the caudate lobe wraps around the inferior vena cava (IVC).

Couinaud's classification [3] divides the liver into eight independent functional segments, based on the fact that each segment has its own blood supply and bile duct, and a separate hepatic venous branch that provides outflow. As shown in (*Figure 6*), segments II, III and IV make up the functional left lobe, V, VI, VII and VIII make up the functional right lobe and the caudate lobe, located posteriorly, is made up by the segment I.

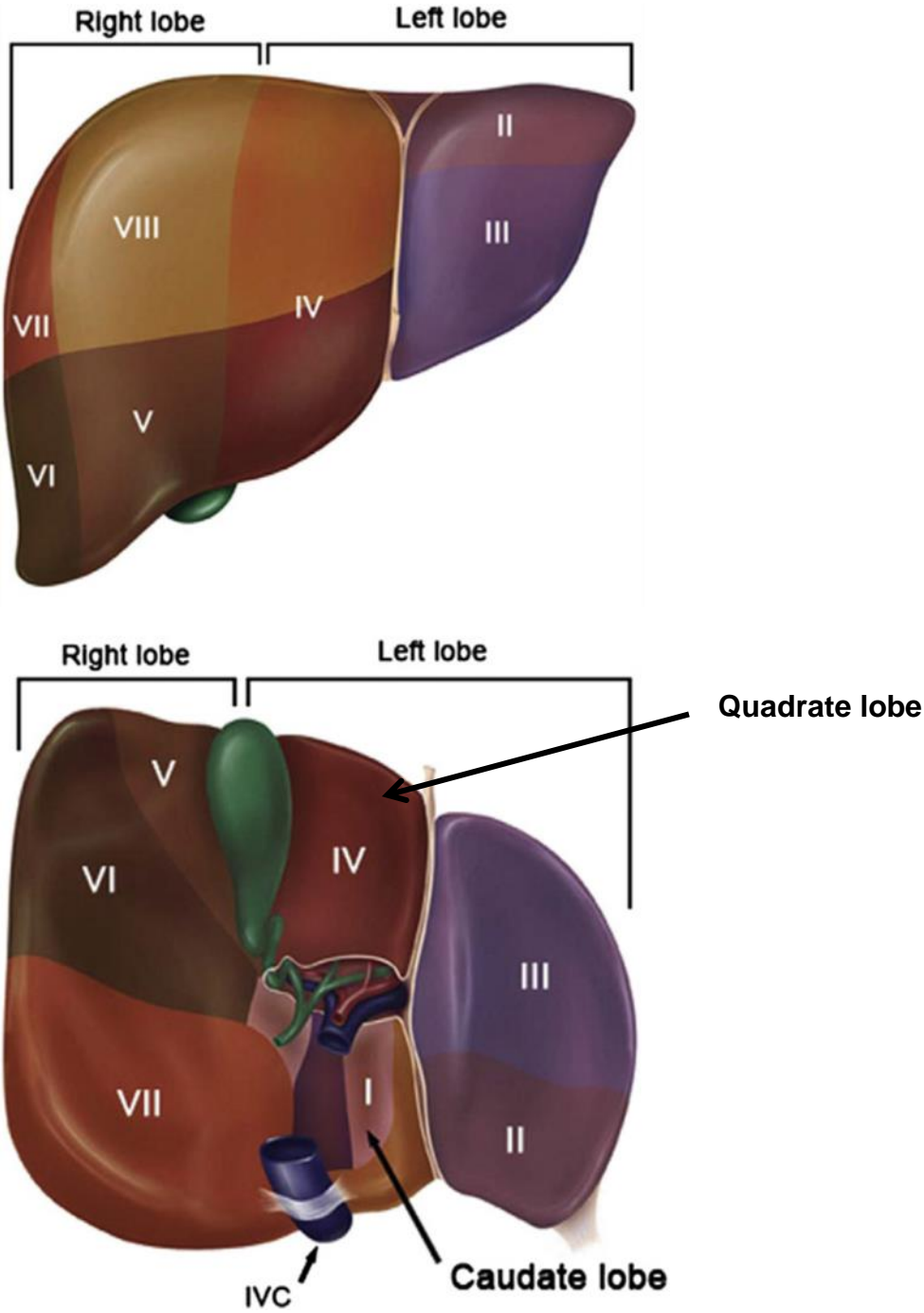


Figure 6 - Anterior and posterior surfaces of liver illustrating functional division of the liver following Couinaud's segmental classification (Inspired by [4]).

Hepatic vasculature

The liver receives blood mainly from two sources: hepatic artery (20-40%) and portal vein (60-80%), except in the case of hepatic tumors where a higher proportion of liver blood is derived from hepatic artery (*Figure 7*). The hepatic artery supplies the liver with oxygen-rich blood (pumped from the heart) needed for hepatic cells survive while portal vein collects nutrients with blood from the digestive system including: intestine, stomach, gallbladder, pancreas and spleen. The blood is drained to the heart through the hepatic vein, leading to the inferior vena cava.

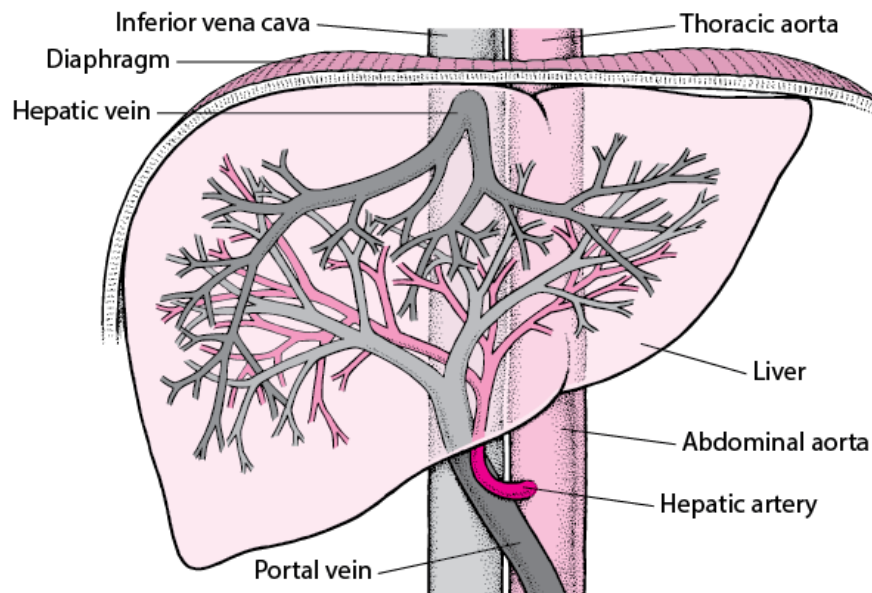


Figure 7 - Blood supply of the liver (from [5]).

Venous vasculature

On normal configuration, the portal vein (PV), or sometimes called the splenic mesenteric confluence, is formed by the union of the splenic vein (SV) and the superior mesenteric vein (SMV). As shown in *Figure 8*, before dividing into left and right portal veins (LPV and RPV), the PV gives rise to left gastric vein (LGV), right gastric vein (RGV) and superior pancreatic duodenal veins. The cystic vein is a tributary of the LPV. RPV is divided into anterior and posterior branches (RPPV and LPPV).

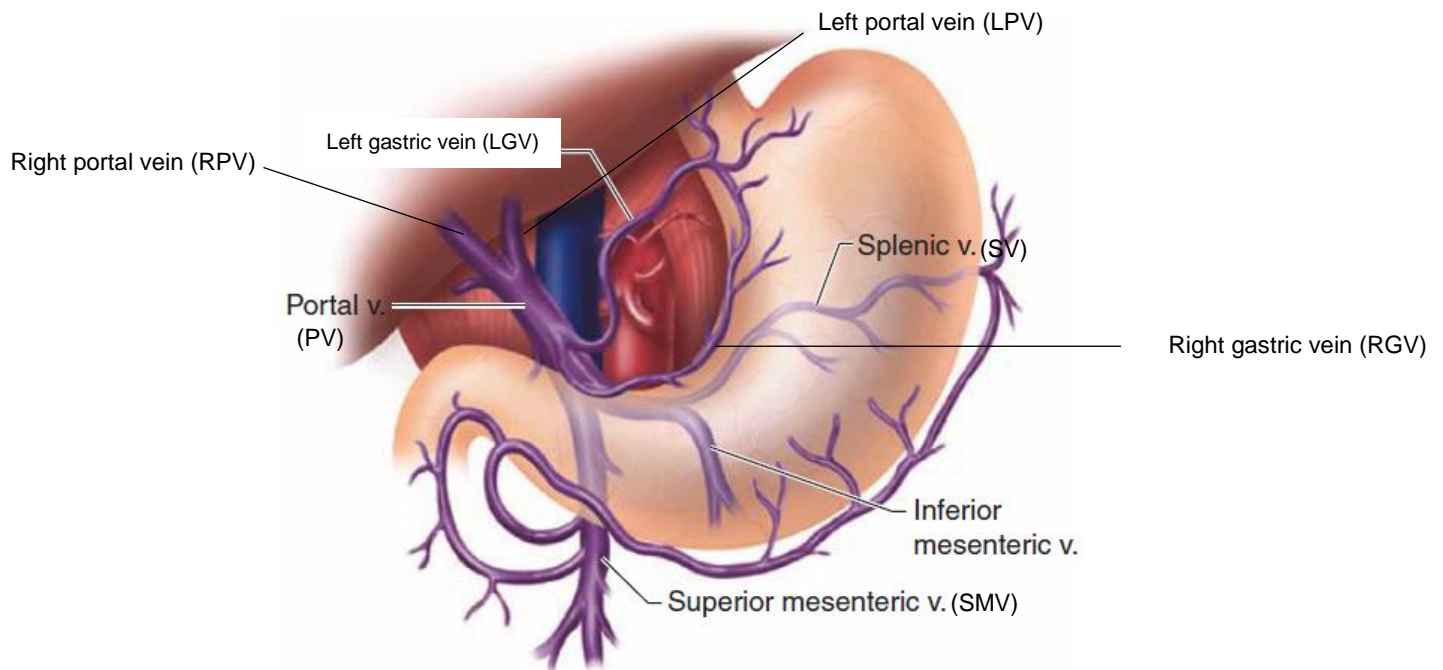


Figure 8 - Portal vein anatomy. The portal vein is formed by the confluence of the splenic and superior mesenteric veins. The inferior mesenteric vein drains into the splenic vein. The coronary (left gastric) vein drains into the portal vein in the vicinity of the confluence. v. = vein (inspired by [4]).

Arterial vasculature

Although the hepatic vasculature is variable, in the most common configuration, the common hepatic artery (CHA), along with the splenic artery (SA) and the left gastric, originate from the celiac trunk which is branched from the abdominal aorta. As illustrated in *Figure 9*, CHA proceeds laterally and divides into the gastroduodenal artery (GDA) and the proper hepatic artery (PHA). GDA proceeds to supply the pylorus of the stomach, the proximal duodenum and the pancreas. PHA branches, itself, to right hepatic artery (RHA) and left hepatic artery (LHA) to supply the corresponding liver lobes. RHA gives rise to an artery called “cystic artery” to supply the gallbladder.

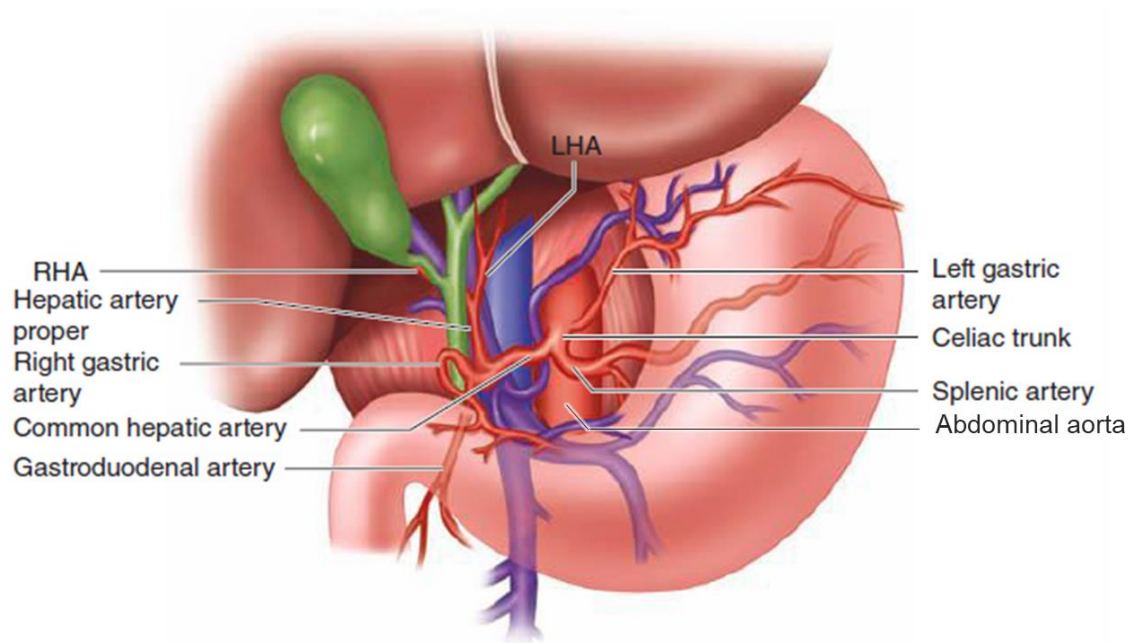


Figure 9 – Arterial anatomy of the upper abdomen and liver, including the celiac trunk and hepatic artery branches. LHA = left hepatic artery; RHA = right hepatic artery (from [4]).

1.1.2 Liver cancer & treatment

Due to different factors, the liver can be damaged in a variety of ways. Different diseases can disturb the liver functions; we can categorize them by their causes:

- Infection: viruses can infect the liver and cause inflammation. Among the most common types of liver infections are hepatitis A, B and C.
- Immune system abnormality: instead of attacking viruses and bacteria, the immune system might attack the liver (autoimmune), causing a chronic inflammation and serious hepatic cells damage. Autoimmune liver diseases include primary biliary cirrhosis, primary sclerosing cholangitis and autoimmune hepatitis.
- Genetics: some abnormal genes inherited from one or both parents can cause genetic liver diseases like Wilson's disease, Alpha-1 antitrypsin deficiency and hemochromatosis.

- Lifestyle factors: alcohol heavy use, obesity, diabetes and improper medication use can contribute to cirrhosis, nonalcoholic fatty liver disease, the infiltration and growth of cancerous or noncancerous cells and many other hepatic problems.

Cancer is the second-leading cause of death in the world, presents abnormal cells that grow and divide uncontrollably and has the ability to infiltrate and destroy healthy tissue. Cancer can develop in the liver, destroy its cells and interfere with its ability to function normally. Besides that it can primarily be formed in the liver (primary cancer), hepatic cancer can begin in another organ (e.g. lung, colon or breast) and spreads to the liver (metastatic cancer). Each year, over 800.000 people are diagnosed with liver cancer throughout the world. It presents a leading cause of cancer deaths, with more than 700.000 deaths every year [6].

The most known primary cancer type, which is considered as the sixth most common malignancy worldwide and represents about 80% of primary liver cancer cases, is called hepatocellular carcinoma (HCC)[7]. HCC is a hypervascular tumor which begins in hepatocyte, presenting the main liver cell type. Unlike normal liver vascularization, HCC is almost exclusively arterially vascularized. HCC often occurs in persons with chronic liver diseases, such as cirrhosis caused by hepatitis B or hepatitis C infection[8] and nonalcoholic fatty liver disease mainly caused by diabetes or obesity[9]. Some other factors may raise the risk of cancer development such as: alcohol heavy drinking and certain drugs use like anabolic steroids (body building steroids). Hepatic cancer diagnosis is generally performed mostly for vulnerable people for which the presence of other diseases that may have the same symptoms are ruled out. Biopsy, blood tests or imaging tests are generally recommended for diagnosis.

Liver cancer treatment options are determined by considering the cancer stage, describing the tumor widespread, and the patient's overall general health. The stage is generally determined following a specific staging system: e.g. Barcelona Clinic Liver Cancer (BCLC) classification system [10], the tumor-node-metastasis (TNM) system[11], Okuda system[12], or the Cancer of the Liver Italian Program (CLIP) system[13].

In general, all types of liver cancer are among the most difficult diseases to be treated, except the case of a primary cancer diagnosed in an early stage. In such case, the tumor can be removed by curative treatment (i.e. surgery) whose recovery chance is high. Curative treatment options include:

- Partial liver resection (hepatectomy): part of liver containing the tumor(s) is removed. The hepatectomy is recommended when the tumor(s) is located in one lobe of the liver. The remaining lobe takes over the functions of the entire liver. The resected part of liver may grow back again within a few weeks.
- Liver transplantation: consists in replacing the cancerous liver by a healthy liver provided by a specific donor. Transplantation is generally used for unresectable (inoperable) liver tumors in patients with advanced cirrhosis.
- Local ablative therapy: used for tumors no larger than 3 cm across. The tumor is destroyed without removal, either by freezing, heat, electrical pulses or by the introduction of pure alcohol. Among local ablative therapies there is radiofrequency ablation where high frequency electrical currents are passed through a needle electrode resulting in a heat that is able to “burn out” the tumor [14]. A non-invasive novel technique, called high-intensity focused ultrasound (HIFU), is also used for tumor ablation [15]. The technique is based on directing an ultrasound beam to the targeted tissue, resulting in a local temperature increase that induces a coagulative necrosis without damaging the surrounding healthy tissue.

Unfortunately, in most cases, curative treatments cannot be performed, either because the cancer size has become too large or because it has spread in many different parts of the liver (i.e. intermediate or advanced stage cancer). These conditions lead to an inclination toward palliative therapies, having the potential to escalate survival and improve the quality of life. Palliative therapies include:

- Radiotherapy [16]: Tumors are treated by high-energy rays delivered by special equipment. The radiation can affect healthy cells.
- Chemotherapy [17]: Tumors are treated by the introduction (injected or ingested) of chemotherapeutic drug that is designed to attack the whole body or specific region fast-growing cells including cancer cells.
- Embolization [18], [19]: Tumors are selectively treated by the direct introduction of specific substances into specific liver artery.
- Targeted drugs: Tumors are treated by the introduction (injected or ingested) of targeted drugs that are designed to attack the whole body changed cells that cause cancer.
- Immunotherapy [20]: Tumors are treated by a patient's own immune system that is boosted by some dedicated medicines. Immunotherapy for the treatment of various cancer types has advanced rapidly in recent years.

Some liver cancer treatments, in particular transarterial radioembolization, are performed by minimally invasive interventions, where interventional tool are introduced under X-Ray image guidance. In the following, we introduce the main principle of radioembolization treatment as well as the typical intervention guidance. Then, we present the proposed approach designed to improve the image guidance during the procedure.

1.2 Image-guided radioembolization

In this section, we present the radioembolization treatment characteristics and workflow, then, we describe the typical intervention image guidance and mention its related issues.

1.2.1 Transarterial radioembolization

Radioembolization (RE), or selective internal radiation therapy, is a minimally-invasive intervention performed to treat unresectable primary and metastatic liver cancer. The treatment relies mainly on the delivery of radioactive glass (TheraSphere, MDS Nordion, Toronto, Canada) or resin (SIR-Spheres, Sirtex Medical, Sidney, Australia) microspheres embedding either Yttrium-90 (90Y) or Holmium-166 (166Ho) isotope into hepatic tumors. The small beads are selectively injected into the hepatic feeding arteries of the tumor by a

trans-femoral catheter in order to retrograde the blood flow and emit a radiation dose that is able to treat the cancer cells. RE has been introduced after the emergence of hepatic artery-directed therapies for HCC in 1950s, when investigators found that hepatic tumors are mainly fed via hepatic arteries (80% of their blood supply is derived from the hepatic artery while normal parenchyma receives its blood from portal vein)[21]–[23]. Due to its demonstrated safety and efficacy by extending the survival of patient to a median reaching 31.9 months [19], [24]–[26], RE has been adopted across BCLC stages. Over recent years, it has emerged as a surrogate of Transarterial Chemoembolization (TACE) [18] [27], the standard therapy used for intermediate stage cancer (BCLC B). RE and TACE procedures mainly differ in terms of injected agent and interventional protocol.

In order to ensure patient eligibility for RE, a pretreatment assessment intervention consisting in catheterizing the arterial tree is performed one to two weeks before the actual therapy. Indeed, a technetium ^{99m}Tc macro aggregated albumin (^{99m}Tc -MAA) is injected as a surrogate of the $^{90}\text{Y}/^{166}\text{Ho}$ to be able to precisely: locate the injection site, detect potential extrahepatic shunting and perform activity planning [28]. During the pretreatment assessment intervention, the injection of ^{99m}Tc -MAA performed through a catheterization procedure plays an essential role in estimating the absorbed dose and activity value of the $^{90}\text{Y}/^{166}\text{Ho}$ microspheres. In fact, the ^{99m}Tc -MAA is used to predict $^{90}\text{Y}/^{166}\text{Ho}$ microspheres distribution during the treatment intervention. An accurate determination and localization of the injection site, in both pretreatment and treatment procedures, directly impact the treatment outcome.

To access the ^{99m}Tc -MAA injection site, an incision is carried out in the common femoral artery with a needle, and then a catheter sheath is inserted so the guidewire, catheter and micro-catheter can be introduced. A trans-femoral flexible catheter is introduced through the sheath with the guidance of a thin guidewire, threaded up to the aorta and selectively catheterizes the celiac trunk. A micro-catheter is then passed into the catheter, pushed through the common hepatic artery, and advanced eventually in the arterial supply of the tumor (*Figure 10*). The ^{99m}Tc -MAA substance is then delivered to the tumor via the inserted micro-catheter.

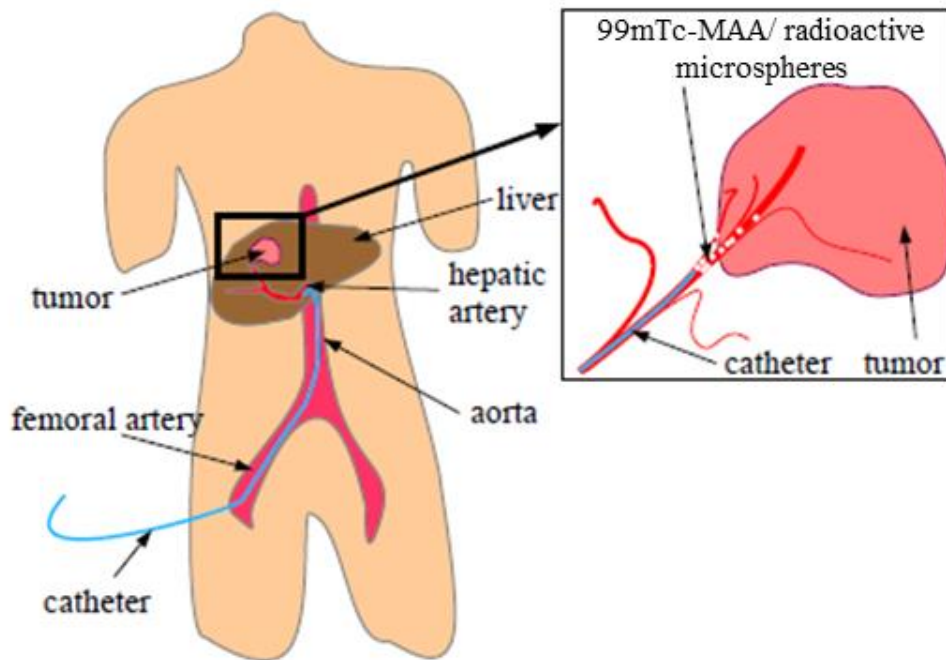


Figure 10 - Radioembolization intervention overview (inspired by [29]).

The catheterization procedure and the confirmed injection site position are carefully reproduced during the treatment intervention for the delivery of $^{90}\text{Y}/^{166}\text{Ho}$ microspheres. Based on the performed $^{99\text{m}}\text{Tc}$ -MAA distribution, a proper $^{90}\text{Y}/^{166}\text{Ho}$ activity is delivered.

Radioembolization has a low rate of serious reactions. Generally, patients may only experience some mild side effects like: abdominal pain, fever, nausea and fatigue, but they may be discharged from the hospital within a day or two after the procedure.

1.2.2 Typical radioembolization image guidance

The main goal of radioembolization is to deliver a customized $^{90}\text{Y}/^{166}\text{Ho}$ activity to the liver tumors with maximum radiation focus, allowing minimizing exposure for the remaining healthy liver parenchyma. The catheterization procedure is performed under image guidance

(Figure 11), as direct eyesight is not possible. In this subsection, we describe the typical radioembolization intervention using image guidance.

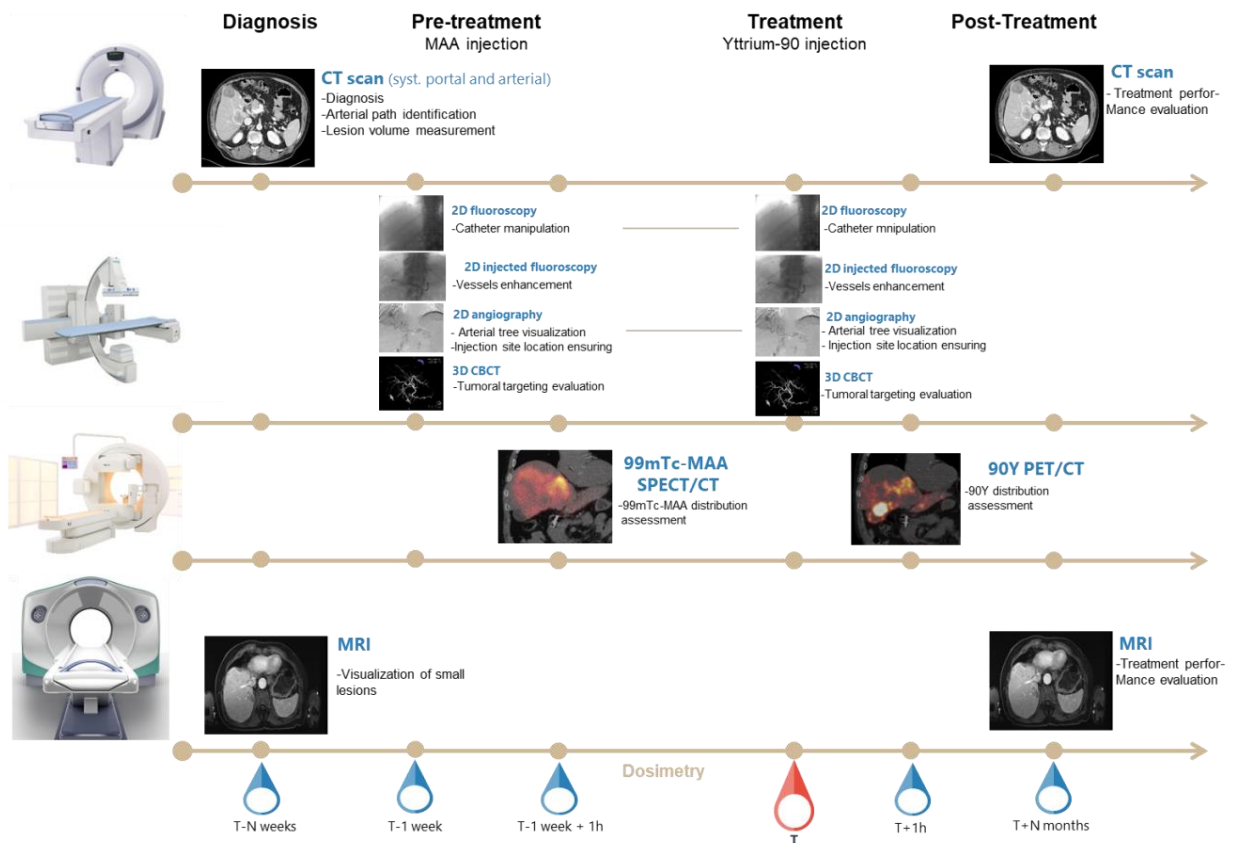


Figure 11 - Radioembolization image guidance.

To prepare the procedure, a prior evaluation of the tumor(s) (i.e. volume, location) is performed preoperatively using various image modalities [30], [31]. Preoperative images, particularly computer tomography angiography (CTA) and Magnetic Resonance Angiography (MRA) generally acquired within few weeks before the intervention, have the potential to identify significant information about the hepatic arterial tree, the tumor location and volume as well as the tumor feeding-vessels. Tumors and vessels are visualized by the administration

Image-guided radioembolization

of contrast agent. This information can help radiologists for disease diagnosis, treatment and follow-up.

The pretreatment and treatment interventions are performed in a room called interventional radiology suite (*Figure 12*), under X-Ray image guidance acquired with a C-arm system. Such a system is able to acquire 2D and 3D reconstructed X-Ray images either with or without contrast agent administration.



Figure 12 - Interventional radiology suite (from [32]).

We can divide the catheter manipulation guidance into five main parts:

- 1- The catheter is manipulated from the femoral artery until reaching the celiac trunk (i.e. departure/ entrance of hepatic arterial tree) while observing predominantly 2D intra-interventional fluoroscopic images. Contrast product is frequently injected in order to localize the celiac trunk origin.
- 2- The celiac trunk originates from the aorta and divides into the splenic artery and the common hepatic artery. In general, once the catheter is inserted in the celiac trunk, the radiologist performs a 2D DSA by injecting the contrast product in order to visualize

the overall structure. The performed 2D enhanced vessel tree is used as a roadmap to assist the common hepatic artery access and to manipulate the micro-catheter inside the hepatic arterial tree.

- 3- At that level, the micro-catheter is inserted to be able to access the hepatic arterial tree. The manipulation of the micro-catheter is performed under 2D fluoroscopic images. For guidance, the radiologist mentally reconstructs the hepatic arterial tree previously visualized in the performed 2D DSA. Contrast product is still continuously injected to enhance the blood vessels and assist the catheter manipulation.
- 4- By reaching the injection site belonging to tumor feeding vessels, another 2D DSA is performed to ensure the location of this determined injection site and finally, ^{99m}Tc -MAA (during the pretreatment assessment intervention) or $^{90}\text{Y}/^{166}\text{Ho}$ (during treatment intervention) substances are injected.
- 5- At the end, a CBCT is acquired to evaluate the perfused tissue and the tumoral targeting and lastly, the micro-catheter and the catheter are smoothly pulled off.

As part of treatment protocol, a ^{99m}Tc -MAA single-photon emission computed tomography (SPECT/CT) is acquired after the pretreatment assessment interventions for ^{99m}Tc -MAA distribution assessment and ^{90}Y dosimetry prediction, performed by the calculation of the ^{90}Y activity that would get an optimal tumor response [33]–[36]. A positron emission tomography with integrated computed tomography PET/CT [37] is acquired after the treatment intervention for the assessment of the treatment success by visualizing the ^{90}Y microspheres distribution, tumor targeting, and quantifying the absorbed dose.

For follow-up, CTA and MRA are also acquired few months after radioembolization in order to ensure the treatment performance in treating lesions.

As described above, interventional radiologists are used to manipulate the catheter while observing predominantly 2D intra-interventional fluoroscopic images, along with 2D digital subtraction angiography images (DSAs) which are acquired to occasionally visualize the arterial tree. Due to the vasculature complexity, the catheter manipulation and more specifically the access to the celiac trunk origin as well as to the injection site, during pretreatment and treatment interventions, is challenging task. The contrast agent used to

highlight vessels is relatively toxic and its continuous or excessive injection can cause severe reactions for the patient. Besides, the continuous radiation exposure for a long procedure can be harmful for both patient and radiologist. Reducing contrast agent use and radiation exposure is still highly dependent on the radiologist experience as well as his ability to understand the vasculature and efficiently manipulate the catheter inside.

Another challenge that can face radiologists is the reproduction of the injection site located during the pretreatment intervention in the treatment intervention. In order to prevent dose distribution deviations, the injection site should be reproduced as identically as possible. In general, the radiologist mentally re-locates the injection site while resorting to X-Ray images (i.e., fluoroscopy and DSA) acquired during the pretreatment assessment intervention when the catheter is being inserted in its final position. In this case, unmatched injection site locations risk is very high.

1.3 Proposed approach

In general, minimally-invasive interventions are performed under image guidance, as direct eyesight of the region to be treated is not possible. Radiologists have generally recourse to intraoperative medical imaging modalities such as X-Ray to manipulate their instruments inside the patient's body. Image guidance can be improved by augmented navigation process that takes benefits of the acquired image modalities or other available measuring devices. In neurovascular procedures, the fusion of preoperative images likes 3DRA, CT or MR with intraoperative fluoroscopic images allows more accurate guidance by providing detailed 3D information regarding the vascular morphology and pathology [38]. In the context of structural cardiac interventions, the overlay of 3D CT data onto the real-time catheterization fluoroscopy proved to be feasible to aid procedure guidance [39]. Moreover, the fusion of echocardiographic and fluoroscopic images provides also precise catheter manipulations under fluoroscopy guidance by visualizing critical tissue anatomy [40]. Indeed, many approaches rely on the fusion of different image modalities in order to augment and complement the radiologist's ability to understand the spatial structure of the anatomy [41]–[46].

To our knowledge, no catheter navigation support approach dedicated to the RE intervention and its specific issues has been introduced in the literature so far. The purpose of our work, in this thesis, is to improve the image guidance in radioembolization interventions by assisting the celiac trunk and injection site access and minimizing the injection site reproduction inaccuracy. The proposed guidance strategy will be detailed in next chapters.

In the context of liver catheterization, some methods have been introduced to align preoperative 3D volumes with 2D intraoperative images using either rigid or deformable registration. Due to the respiration motion, the liver undergoes mainly a cranio-caudal translation [47], [48], while deformation occurs mainly in the superior and inferior liver areas [49], [50]. Thus, some guidance approaches are limited to rigid-body registration to align pre- and intraoperative hepatic structures. In the context of chemoembolization, which is similar to RE except the injected substances (i.e. combination of embolic and chemotherapeutic agents) [27], Ambrosini et al. [29] designed a 3D/2D real-time rigid registration method between 3D rotational angiography (3DRA) and 2D fluoroscopy based on 3D extracted vessels and 2D catheter shape. The study demonstrates that the accuracy is highly depending on the 2D catheter segmentation precision, which might fail due to the variety of surgical scenes. In order to be robust against the segmentation error, the authors proposed the use of a probabilistic model to track the catheter tip inside the patient's 3D vessel tree [51]. Bargellini et al. [52] proposed a rigid registration technique of relevant 3D structures, segmented from a CTA volume, with the 2D intra-interventional fluoroscopy based on the lumbar spine. Their method demonstrates its benefit to provide confident hepatic arterial catheterization. The main drawback lies, nevertheless, in the fact that the proposed registration is performed manually.

Deformable registration methods have also shown promising results for aligning vessels despite excessive deformations due to artifacts and noise. Guevara et al. [53] suggested a solution based on a biomechanical model in order to preserve the physical behavior of the liver and to avoid the inappropriate deformations. Their approach aims at aligning the preoperative CT with the intraoperative CBCT images, thanks to a graph matching technique. However, the computation time (i.e. 7.3 min) makes the method not compatible with the context of interventional guidance.

To our knowledge, there is no X-Ray image augmentation solution for catheter manipulation and target site reproduction specifically dedicated to RE intervention guidance. In this context, we intend to develop and evaluate a novel guidance strategy that promises a simplification and accuracy of the catheter navigation during the pretreatment assessment, as well as during the treatment interventions. As part of RE clinical routine, 3D CTA is acquired to plan the intervention. The vascular system is visualized in this 3D image by the injection of contrast product. Our proposed navigation system processes preoperative (*i.e.* CTA) and intraoperative images to achieve intraoperative image fusion through a rigid registration technique. This approach is designed to: 1) assist the celiac trunk access, 2) assist the injection site access and 3) automatically reproduce the injection site during the proper intervention.

The three fusion steps are depicted in (*Figure 13*) and will be presented in the next two chapters. Image registrations are designed to guide the pretreatment assessment intervention by projecting the celiac trunk and the hepatic arterial tree on 2D X-Ray images and to guide the treatment intervention by reproducing the injection site path.

Augmenting 2D intraoperative X-Ray images, by projecting relevant information from either 3D preoperative CTA or pretreatment X-Ray images, has the potential to enhance the visual guidance while providing precision and safety to the catheter manipulation. However, due to respiration motion, the liver undergoes a continuous displacement [47], [48], [50], hampering the arterial tree static projection. In this context, our objective is also to deal with dynamic overlay of the projected 3D vessels onto fluoroscopy despite the respiration motion.

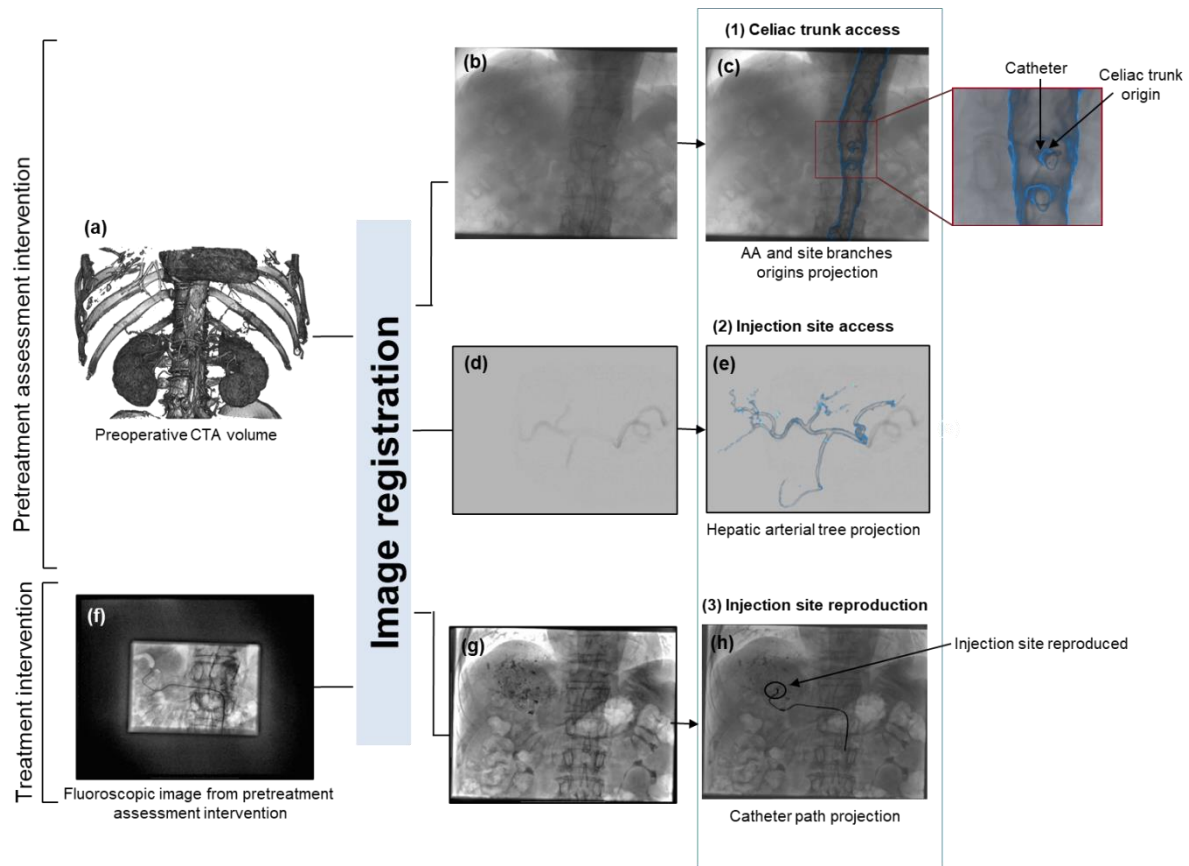


Figure 13 – Proposed navigation system. During pretreatment intervention, the preoperative arterial phase Computed Tomography (CTA) images (a) are firstly registered to the real-time fluoroscopic image (b), and the abdominal aorta (AA) as well as the celiac trunk and the superior mesenteric origins are projected to assess the celiac trunk catheterization (c). At the level of the celiac trunk, a contrast product is injected and a DSA is acquired (d) and registered to the CTA based on a delimited vascular-structure, and the hepatic arterial tree is projected to assess the IS access (e). Once reaching the IS, a fluoroscopic image is captured (f), and registered to the real time fluoroscopic image (g) during the treatment intervention, to assess the IS reproduction (h).

2 Pretreatment assessment intervention guidance

2D intraoperative fluoroscopic images provide basic information about the patient's anatomy (i.e. bone structure) and inserted interventional tools, whereas, as described in section 1.2.2.), the nonpermanent vascular structure visualization is still dependent on contrast medium injection (i.e. angiographic images). Computer-aided image guidance solutions have been introduced to enable the enhancement of visualization and to provide a more comprehensive feedback of the surgical scene. In particular, these solutions enable the augmentation of intraoperative 2D X-Ray images (i.e. fluoroscopic and angiographic images) by combining them with 3D medical images, preoperatively acquired, using 2D/3D registration.

The registration of the two image modalities can be handled in different manners. In this chapter, we provide an overview of registration methods used to augment 2D X-Ray images and we expose the proposed registration framework (section 2.1.) being used in our computer-assisted navigation approach. In sections 2.2. and 2.3., we present the first two fusion steps being designed to guide the pretreatment assessment intervention by assisting the celiac trunk access and the injection access, respectively.

2.1 Registration approach

The 2D X-Ray images intrinsic nature often requires the clinicians' capacity to mentally construct the 3D surgical scene. In fact, this procedure is not always reliable due to the anatomical variability. In order to conceive a better visualization of a specific patient surgical scene, many acquisitions from different angles may be performed by a C-arm before starting the intervention. However, these acquisitions might be time consuming and lead to an increased radiation exposure. In this context, many studies focus on taking advantage of preoperative 3D images and register them, either manually or automatically, to intraoperative X-Ray images in order to provide a more extensive view beyond the visible anatomy [54]–[57] (an example is illustrated in *Figure 14*). The enhanced visualization by 2D X-Ray augmentation has the potential to reduce the intervention time, contrast medium injection and the radiation exposure. This has been demonstrated by [58], who performed a comparison between classic thoracic endovascular aortic repair procedures (TEVAR) and TEVAR procedures performed with 2D/3D image registration.

Registration approach

Different 2D/3D registration methods are introduced in the literature. Our investigated method requires speed and accuracy as two important aspects of performance in the context of RE image guidance. Our overall proposed solution is intended to be integrated in EndoNaut®, THERENVA for the guidance of radioembolization interventions. EndoNaut® is an intraoperative navigation solution device provided by THERENVA and used for aortoiliac and peripheral artery disease procedures (*Figure 15*).

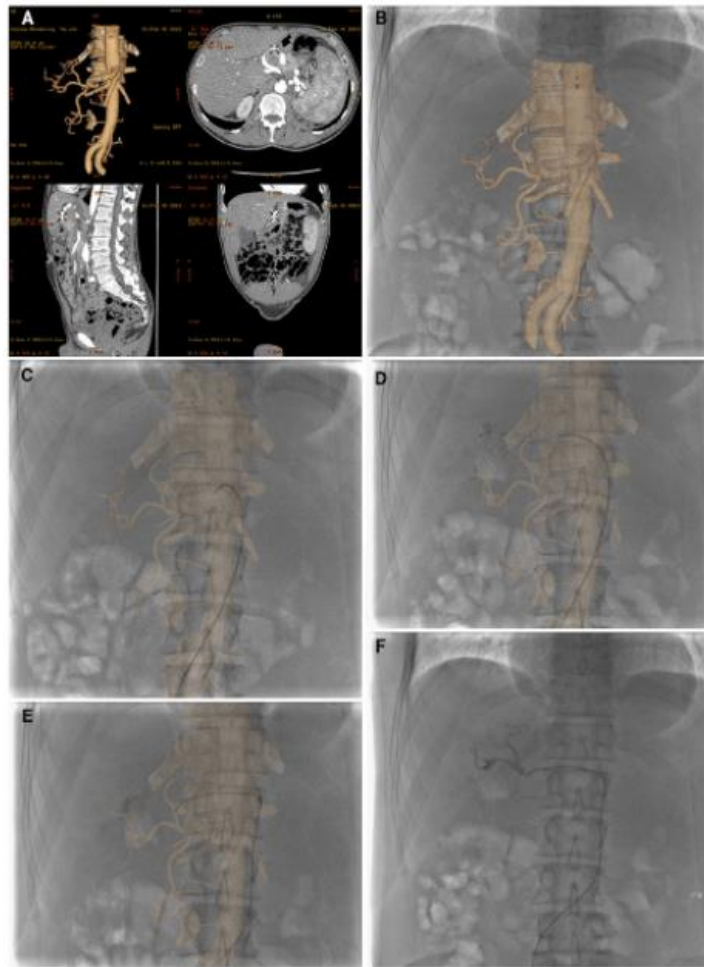


Figure 14 - Early arterial phase CT images are post processed on an independent workstation by semiautomatic segmentation, obtaining the VR model of abdominal aorta and splanchnic arteries (A). The 3D model is then manually registered to the real-time fluoroscopic image using the bone structures as reference (B), and it is used to catheterize the celiac trunk (C) and the proper hepatic artery (D, E). Only at this time is 3 mL of contrast medium injected to check the correct catheter position (F). It is possible to notice how the VR model allows visualizing the hepatic structure, not enhanced in 2D fluoroscopic images.

From [57]



Figure 15 - EndoNaut® navigation device, THERENVA.

2.1.1 2D/3D Registration

2D/3D image registration can be defined as a search for the spatial transformation that brings the 3D preoperative data and 2D intraoperative data into the same coordinate system [59]. Other than manual registrations which are imperfect by definition, an overview of automatic 2D/3D registration methods can be found in [59]–[61]. In the following, we summarize the classification of 2D/3D registration methods.

As presented by [59], we can classify 2D/3D registration methods into calibration-based, extrinsic, or intrinsic. Calibration-based methods rely on the use of known device calibration to align the 2D intraoperative X-Ray image with the 3D preoperative image [38], [62]. This approach requires the use of same 2D and 3D image acquisition device.

Extrinsic methods generally rely on external markers, presenting external objects attached to the patient, for registration [63] while intrinsic methods rely on anatomical structures as bone structures or vascular structures to register images. We can further classify registration approaches into feature-based and intensity-based.

Feature-based approaches consist in computing a geometric distance between features (e.g. vessel centerlines, contours, bifurcations, etc.) extracted from 2D images and projected features of the 3D preoperative images [29], [55], [64]–[67]. Feature extraction usually requires a segmentation step. For example, in vessel based registration methods where vasculature is used for registration, a segmentation of the both vasculatures visualized in 2D intraoperative X-Ray image (i.e. angiography) and preoperative 3D image are required to extract some features like centerlines, contours and bifurcations before performing the registration. Feature-based approaches have proven to be accurate and fast since they don't evaluate a matching criterion on every image pixel, but rather rely on a relatively small number of features. However, these approaches can suffer from robustness issues depending on segmentation precision. In intraoperative X-Ray augmentation, anatomical structures may vary from patient to another, decreasing automatic segmentation performance accuracy. Moreover, a manual segmentation process could be time consuming and hence, not compatible with the clinical workflow. This drawback can be partially overcome by intensity-based methods, which do not require any intraoperative segmentation step.

Intensity-based approaches count on all image pixels intensities by evaluating and optimizing a similarity measure between the intraoperative X-Ray image and the projection of the 3D preoperative image [46], [68]–[71]. Different similarity measures have been proposed and evaluated for this purpose [70]. Intensity-based methods are also proven to be accurate but their accuracy can depend on the 3D preoperative image projection quality as evoked by [59] and [61], when there is no correspondence between intraoperative X-Ray and preoperative projection images. They might also be more computationally demanding and tend to converge slowly, preventing their integration into clinical workflow [46], [72].

Unlike feature-based registration approaches requiring intraoperative image segmentation which is a limitation for interventional application, our work will focus on investigating a rigid intensity-based approach.

Furthermore, to determine the performance, the limitations as well as the validity for clinical use of a proposed registration method, a rigorous evaluation experiment must be performed.

Validation can be performed using a qualitative or quantitative method to qualify or quantify the registration error [73]. Visual inspection consists in using structures overlays, side-by-side viewing or checkerboard displays [74], [75]. This type of evaluation is subjective and can be used for small database. Quantification methods can employ either ground truth or gold standard for validation. Ground truth presents an exact definition of the correct transformation and gold standard uses an approximation of it. The ground truth is hard to be defined and few methods can truly provide it. Validation approaches that are based on phantoms [76] or simulated images [77] are able to potentially define a ground-truth, however, these methods suffer from lack of realism, making them less significant for clinical applications. Most of methods rely on gold standard for validation. Many gold standard based validation approaches consist in aligning corresponding anatomical structures belonging to the fixed and transformed images or volumes (after registration). This alignment can be defined by different quantitative measures such as overlap [78]. This validation approach accuracy depends on the feasibility of defining these structures and their segmentation precision.

Validation can be also performed by measuring the distance between corresponding points that belong to the fixed and moving images. These points can correspond to anatomical landmarks or tailor-made markers. This validation method provides a direct measure of how well corresponding points line up after registration. However, it only measures registration accuracy at these specific points' locations (i.e. anatomical landmarks or tailor-made markers) and not at non-points locations. Hence, a dense population of points is required to get a better estimation of the registration accuracy [78].

In our context, we will favor a gold standard based approach to evaluate the registration method performance.

In the next subsections, we present the proposed registration approach and provide the validation method details.

2.1.2 Proposed multiresolution intensity-based registration

In our work we propose to investigate an optimized structure-driven intensity-based approach to perform preoperative and intraoperative image fusion (*Figure 16*). In order to improve the registration, this approach consists in segmenting a 3D preoperative CTA before the intervention in order to generate a projection image, a Digitally Reconstructed Radiograph (DRR), corresponding to the anatomical structure visible in the real X-ray image (*Figure 17*). The CTA volume segmentation is performed using Endosize®, THERENVA sizing software [79] (*Figure 18*).

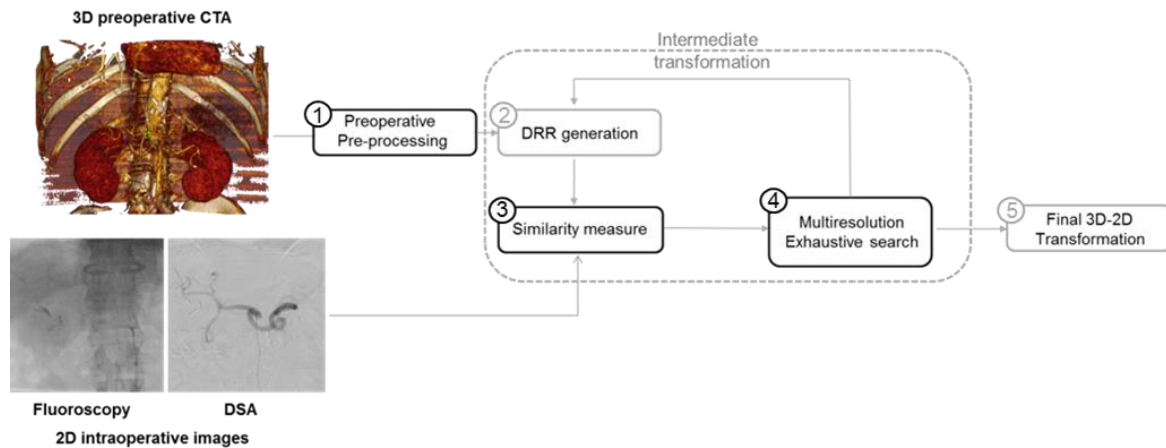


Figure 16 - Intensity-based registration framework with its main components. Preoperative arterial phase Computed Tomography (CTA) images are semi-automatically segmented using endosize®, obtaining either a 3D bony-structure or delimited vascular-structure (1). DRR image is generated from the preprocessed volume (2) and compared to the 2D intraoperative image through a similarity metric presenting a quantitative criterion describing how well the input images are similar (3). For optimization, the 3D volume is intermediately transformed following an exhaustive search and the transformation result is progressively refined following a multiresolution scheme (4). The final 3D/2D transformation corresponds to the transformation giving the best achieved similarity measure (5).

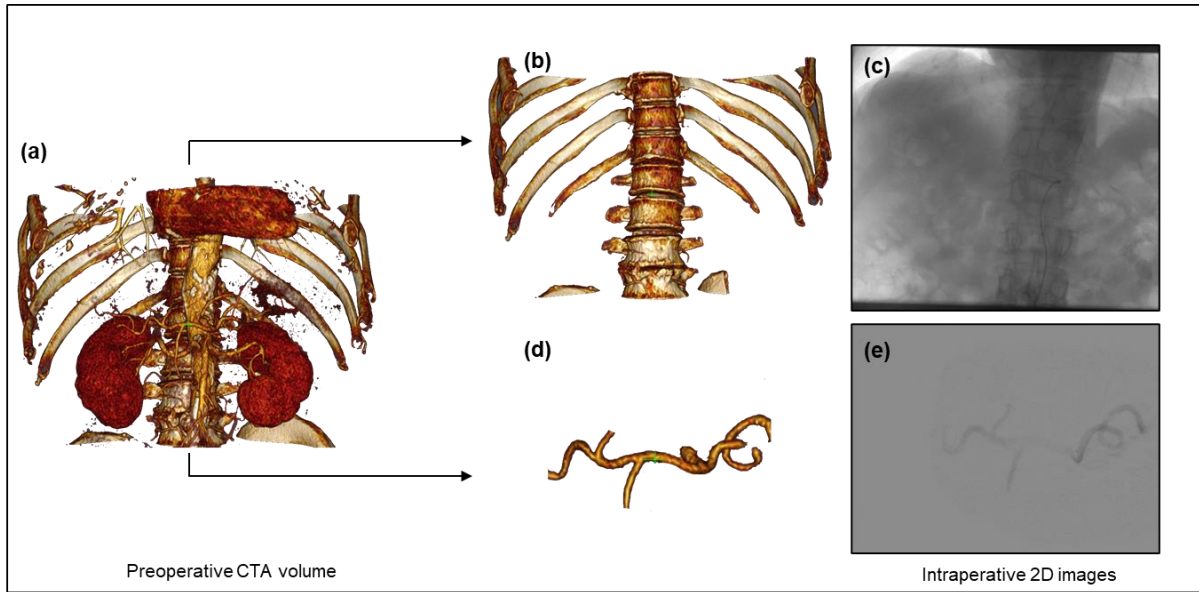


Figure 17 - An example of preoperative CTA (a) segmentation. The bone structure extracted from CTA (b) corresponds to the anatomical structure visible in intraoperative fluoroscopic image (c), while the vascular structure extracted from CTA (d) corresponds to the anatomical structure visible in intraoperative angiography (e).



Figure 18 - Preoperative CTA segmentation using Endosize®, sizing software, THERENVA. The segmentation process takes about 10 min.

The registration algorithm is based on an optimization by a reduced exhaustive search involving a multi-resolution scheme with a decomposition of the transformation in order to reduce the computation time, making it compatible with clinical workflow.

Considering predefined ranges of unknown parameters and a rough initialization by the user, the multi-resolution algorithm, originally introduced in the context of endovascular aortic aneurism repair [46] and successfully integrated in EndoNaut® device, is implemented to perform an exhaustive search of the pre/intraoperative transformation. The optimal 3D/2D transformation is obtained following a multi-resolution coarse-to-fine registration between synthetic 2D X-Ray images (i.e. DRRs) generated from the 3D preoperative volume and intraoperative real 2D X-Ray image (i.e. fluoroscopy or DSA) acquired by a C-arm. DRRs are generated from the preprocessed CTA by using the projection inherent to the fluoroscopic imaging system (known intrinsic parameters) and approximating X-ray absorption process by volume rendering with ray-tracing [80].

The multi-resolution scheme consists in progressively refining the transformation result. At each resolution level, the optimal transformation is estimated by performing a reduced exhaustive search while decomposing the transformation T into in-plane and out-planes transformations, as introduced in [72]. The parameter space of each transformation is sampled on a regularly discretized range and the different combinations of parameters T^i result in n transformations such that:

$$T^i = T(t_x^i, t_y^i, t_z^i, r_x^i, r_y^i, r_z^i); \quad i = 1, 2, \dots, n$$

where t_y^i, r_x^i, r_z^i correspond, respectively, to the translation and rotation parameters of the out-plane transformation applied on the 3D volume and t_x^i, t_z^i, r_y^i refer to the parameters of the in-plane transformation applied to obtain the resulting DRR (*Figure 19*). A similarity measure is computed between the intraoperative 2D image and the DRR for each combination of the parameters. The optimal transformation corresponds to the combination of parameters giving the best similarity measure outcome. It is used as the initial solution for the next resolution level.

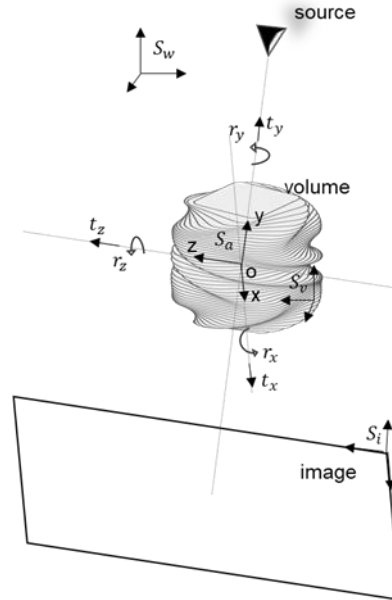


Figure 19 - Geometric configuration used for registration. S_w is the world coordinate system, S_i is the intraoperative image coordinate system, S_v is the preoperative volume coordinate system and S_a is the coordinate system where: O_{xz} is the plane parallel to the plane of intraoperative image and O_y is aligned with the main axis of c-arm. t_x and t_z correspond to in-plane translations and t_y corresponds to the out-plane translation (along the axes of S_a). r_x and r_z correspond to the out-plane rotations and r_y corresponds to the in-plane rotation (around the axes of S_a)

In the following, the implementation of this method and obtained results are presented for the celiac trunk access and the injection site access respectively.

2.2 Celiac trunk access

Given the celiac trunk catheterization complexity, radiologists often resort to repeated contrast product injection to visualize the vasculature that is close to the catheter (about 15 mL for each DSA acquisition). The celiac trunk origin visualization through real-time fluoroscopic images augmentation has the potential to ease the catheterization while reducing the contrast medium injection. According to a study performed by Sailer et al. [81] on 60 different CT scans acquired during inspiration and expiration, abdominal side branches (e.g.

the celiac trunk) undergo only a slight caudal motion of 1.3 ± 1.1 mm. Another study that was performed by Ali R. [82] et al. asserts that the main cause of the abdominal aorta (AA) displacement or deformation is the introduction of stiff instruments. As catheters used in the context of RE are flexible, we assume that they don't able to deform the vasculature.

Given these works and assumptions, and knowing that the celiac trunk catheterization is mainly performed under the guidance of 2D fluoroscopic images where only the inserted catheter as well as the bone structure are visible, we choose to segment and only retain the bone structure in preoperative 3D CTA to perform a rigid 3D/2D registration between preoperative CTA and intraoperative 2D fluoroscopy. Indeed, we have investigated the accuracy of the registration method that is described above on augmenting the 2D real-time fluoroscopic by projecting the AA and the celiac trunk origin.

2.2.1 Experiments

A preliminary step consisting in extracting the bony-structure from the CTA is foremost performed in order to generate appropriate DRRs. The vascular-structure to project is also segmented, simultaneously, using Endosize®. This software allows placing three reference points in the CTA volume in order to determine the structure to extract and from where the segmentation is automatically carried out. Before assessing the registration method accuracy, preliminary tests were performed to set the exhaustive search parameters (*Table 1*).

Table 1- Parameters used during the optimization phases (r = resolution of the discretized range of the parameters)

Step	In-plane translation (mm)		Out-plane translation (mm)		In-plane rotation (°)		Out-plane rotation (°)	
	Range	r	Range	r	Range	r	Range	r
1	[-16;16]	4	[-100;100]	25	-	-	[-8;8]	4
2	[-8;8]	4	[-40;40]	20	[-4;4]	4	[-4;4]	4
3	[-2;2]	2	[-20;20]	20	[-3;3]	3	[-3;3]	3
4	[-1;1]	0.5	[-10;10]	10	[-2;2]	2	[-2;2]	1
5	[-0.3;0.3]	0.3	[-4;4]	2	[-1;1]	1	[-1;1]	0.5
6	[-0.2;0.2]	0.2	[-2;2]	2	[-0.6;0.6]	0.3	[-0.6;0.6]	0.3

We have evaluated the impact of different similarity measures [70] on the registration outcome. Gradient information (GI), gradient difference (GD), gradient correlation (GC), normalized cross correlation (NCC) and Mutual information (MI) have been tested. For each patient case, evaluation process was performed in four steps: defining a gold standard (GS) registration, generating random initial transformations, performing corresponding registrations and computing a mean error. The steps are described in detail below. In the first step, the GS was obtained by a manual registration (between the preoperative CTA and the intraoperative fluoroscopic image) carefully performed by an expert and used as a reference transformation for the evaluation protocol. Fifteen initial transformations were randomly generated within a defined range away from the assumed GS in order to analyze the influence of the rough manual initialization required from the user. This defined range was fixed to ± 10 mm for each of the three translational axis and ± 4 degrees for each of the three angles. The registration was then performed from each random initial transformation. The registration accuracy was expressed by the mean error representing the mean 2D Euclidean distance calculated on the registrations of one patient case and the global mean error representing the mean 2D Euclidean distance calculated on all patient cases' registrations. The mean 2D Euclidean distance was computed from all the points belonging to the considered anatomical structure (i.e. bony-structure) obtained by applying the reference transformation and their homologues obtained by applying the resulting transformation. Registration success rate was defined as the number of registrations showing a mean 2D Euclidean distance below a certain threshold T . The threshold was fixed to 5 mm according to a visual assessment of the results. Following the registration, the 3D vascular-structure (i.e. the AA and its side branches origins) was transformed and projected onto the intraoperative fluoroscopic image in order to assist the catheterization. At this stage, a qualitative evaluation was carried out by an expert to assess the final rendering. We used 2D fluoroscopies captured after the catheterization of the celiac trunk origin for evaluation. For each patient, the expert visually inspected the position of the celiac trunk origin (ostium region visible in the projected 3D vascular structure) and the catheter (visible in the 2D fluoroscopy) by verifying if an overlap occurs between them. The underlying assumption was that this overlapping is a necessary condition for the proposed

approach to be efficient in reaching the celiac trunk origin with no need for intra-arterial contrast injection or DSA acquisition.

In the following, we present the clinical data used for the evaluation and report the 3D/2D registration results related to the celiac trunk access.

Clinical data

The overall approach was tested and evaluated on patient cases who underwent 90Y RE interventions between August 2014 and February 2019 at Centre Eugène Marquis (Rennes, France). Multiple factors were taken into consideration for patient selection as described in [83]. This was an observational study for which 20 patient cases were retrospectively included and randomly selected according to the data availability. Patient informed consent was obtained for being registered anonymously in the research database.

Contrast-enhanced CT scan (i.e. CTA) and 2D X-Ray images (i.e. fluoroscopy) are provided within the standard imaging protocol. The contrast-enhanced CTs were acquired on a SOMATOM Definition (Siemens Medical systems, Forchheim, Germany) with the following typical parameters: 203 slices number, 0.7890 x 0.7890 mm pixel size, 1.5 mm slice thickness, 1 pitch, 19 x 1.2 mm collimation, 1085 mm source to detector distance and 137 mA X-Ray tube Current. The 2D fluoroscopic images were acquired intraoperatively on a C-arm Artis Zeego (Siemens Healthcare, Forchheim, Germany) with 1149 mm source to detector distance and 0.3729 x 0.3729 mm pixel size. These intrinsic parameters have been used for the generation of DRRs.

2.2.2 Results

In (*Figure 20*), we show the bone-based rigid registration method results when varying initial conditions (i.e. 15 random initial transformations for each of the 20 considered patient cases) for the different similarity measures. The mean error varies from 1 mm to 60 mm. Best results are obtained by using GD, with a global mean error of 5.23 mm and a median at 1.40 mm.

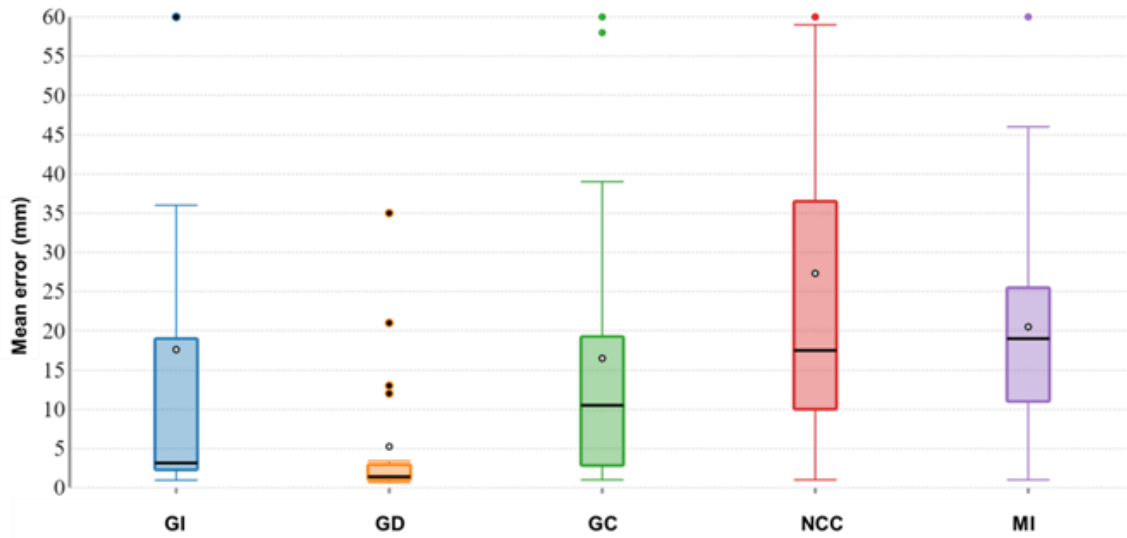


Figure 20 - Boxplot of the mean errors obtained with each SM for 20 patient cases

In Table 2, we show the results by considering the threshold $T = 5$ mm. Registration demonstrated a success rate of 274 registrations out of 300 using GD with a global mean error of 1.59 mm calculated on registrations achieving a mean 2D Euclidean distance below T . Results were less notable when using GI, GC, NCC or MI with a maximum success rate of 214/300 achieved when using GI. The average computation time for one registration was 5s on an integrated Intel graphic GPU Nvidia quadro k420 machine.

Table 2 - Bone-based registration results using different similarity measures. Global mean error is calculated on registrations obtaining a mean 2D Euclidean distance $< T$

Similarity measure	GI	GD	GC	NCC	MI
Success rate	214/300	274/300	125/300	129/300	76/300
Global mean error	1.88	1.59	2.32	2.34	3.03

The projection of the AA and side branches origins, which are resulted from the bone-based registration using the GD are however significant. In 83% of these registration cases, the expert confirmed that the visual result is substantial and the projected structure can

appreciably help radiologists on catheter manipulation (*Figure 21 (c)*). In the remaining 17 % of the cases, a shift between the catheter position and the ostium can eventually slightly hamper the navigation (*Figure 21 (f)*).

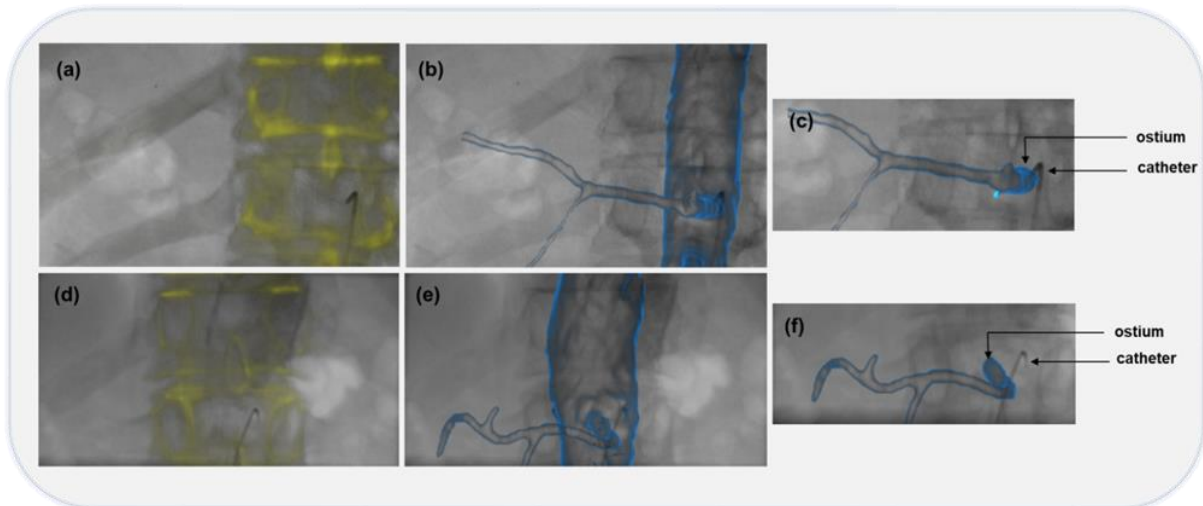


Figure 21 - Celiac trunk access assessment for two different patient cases. Preoperative CTAs are registered to intraoperative fluoroscopic images based on bony-structures (a) (d). The projection of AA and side branches (b) (e) results in a celiac trunk ostium and catheter overlap in the first case (c) whereas a slight shift between the two components is noticed in the second case (f).

2.3 Injection site access

At the level of the celiac trunk, a micro-catheter is generally passed through the common hepatic artery (CHA), advanced in the proper hepatic artery (PHA) and eventually inserted in the right or left hepatic artery (RHA or LHA respectively) depending on the location of the tumor. The hepatic arterial tree projection is chiefly proposed to augment the intraoperative fluoroscopic images and the low-contrast DSA generally acquired at the level of the celiac trunk, and to simplify the access to the injection site in the midst of the vasculature complexity (*Figure 22*). Accordingly, we have taken advantage of the 3D/2D rigid

registration method previously introduced to align the hepatic vascular-structure extracted from the CTA with the intraoperative DSA.

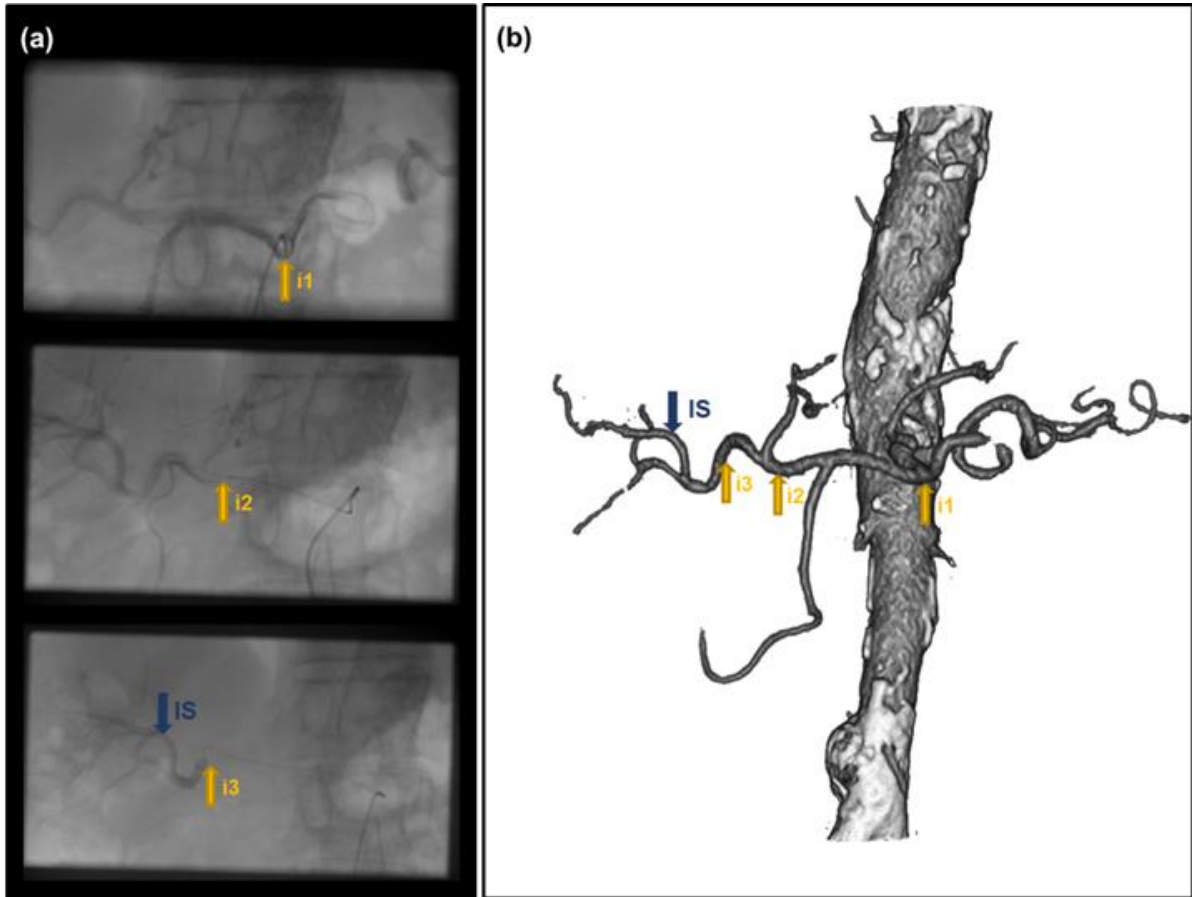


Figure 22 - Preoperative and intraoperative vascular-structure visualization for a typical patient case. To access the IS, several fluoroscopic images showing incomplete vasculature are acquired with contrast injection at different locations of the catheter tip: i1 (celiac trunk origin), i2 (proper hepatic artery) and i3 (right hepatic artery) (a). A more complete vasculature is visualized in the CTA extracted volume (b).

2.3.1 Experiments

We have firstly adapted the parameter settings of the multiresolution exhaustive search (*Table 3*) while taking into consideration the manual initialization of the structure and the hepatic arterial tree motion.

Table 3 - Parameters used during the optimization phases (r = resolution of the discretized range of the parameters)

Step	In-plane translation (mm)		Out-plane translation (mm)		In-plane rotation (°)		Out-plane rotation (°)	
	Range	r	Range	r	Range	r	Range	r
1	[-20;20]	5	[-25;25]	25	-	-	[-8;8]	4
2	[-8;8]	4	[-25;25]	25	[-4;4]	4	[-4;4]	4
3	[-2;2]	2	[-20;20]	10	[-3;3]	3	[-3;3]	3
4	[-1;1]	0.5	[-10;10]	10	[-2;2]	2	[-2;2]	1
5	[-0.3;0.3]	0.3	[-4;4]	2	[-1;1]	1	[-1;1]	0.5
6	[-0.2;0.2]	0.2	[-2;2]	2	[-0.6;0.6]	0.3	[-0.6;0.6]	0.3

Registration is performed by considering a specific preoperative vascular-structure. Two configurations were tested by considering: 1) hepatic vascular-structure (HVS) including: CHA, PHA, the departure of the gastroduodenal artery (GDA), LHA and RHA, and 2) HVS along with the splenic artery (HVSS) (*Figure 23*). Besides, we have investigated, as described in (subsection 2.2.1), the effect of the different similarity measures. Similarly to the bone-based registration, the method has been evaluated by comparing the estimated rigid transformation to the GS resulting one. The accuracy is expressed by the global mean error and the mean error. For vessel-based registration, the mean error represents the mean 2D Euclidean distance computed from all the points belonging to the vascular structure obtained by applying the reference transformation and their homologues obtained by applying the resulting transformation.

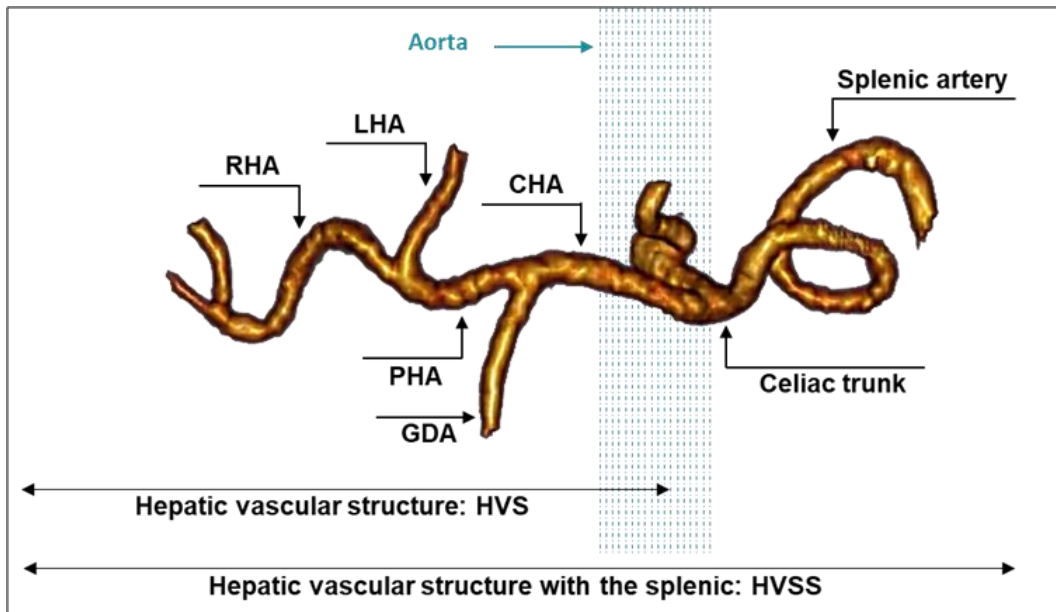


Figure 23 - Three dimensional volume-rendering (3D VR) generated from CTA showing the hepatic arterial anatomic structures. CHA = common hepatic artery, GDA = gastroduodenal artery, PHA = proper hepatic artery, LHA = left hepatic artery and RHA = right hepatic artery

In the following, we present the clinical data used for the evaluation and report the 3D/2D registration results related to IS access.

Clinical data

This was an observational study for which 19 patient cases were retrospectively included and randomly selected according to the data availability. Patient informed consent was obtained for being registered anonymously in the research database.

DSAs are provided within the standard imaging protocol and were acquired intraoperatively on a C-arm Artis Zeego (Siemens Healthcare, Forchheim, Germany) with 1149 mm source to detector distance and 0.3729 x 0.3729 mm pixel size. These intrinsic parameters have been used for the generation of DRRs. Each DSA is acquired after the injection of 15 mL iodine.

2.3.2 Results

The vessel-based rigid registration method is tested for two different configurations by considering the HVS and the HVSS. In *Figure 24*, we show the vessel-based rigid registration method results when varying initial conditions (i.e. 15 random initial transformations for each of the 19 considered patient cases) for the different similarity measures while keeping HVS as input vascular-structure.

By considering HVS, the mean error varies from 1 mm to 100 mm (obtained when the registration is unsuccessful). Best results are obtained by using GD, with a global mean error of 3.87 mm and a median at 2.35 mm.

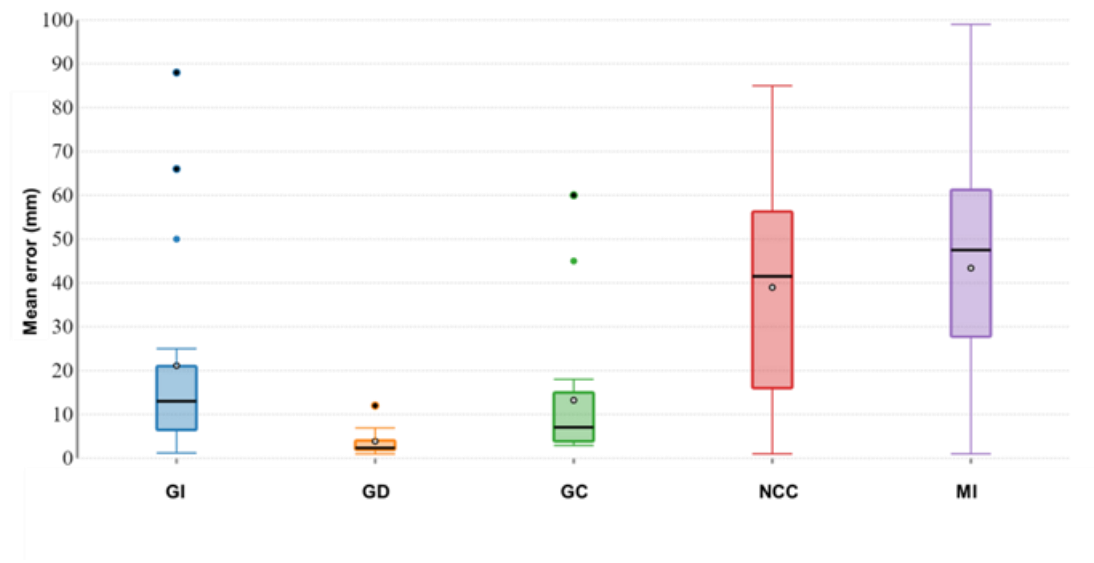


Figure 24 - Boxplot of the mean errors obtained with each SM considering only HVS for the 19 patient cases

Table 4 shows the registration results when varying the similarity measure by considering the threshold $T = 5$ mm, while keeping HVS as input structure.

Table 4 - Vessel-based registration results using different similarity measures. Global mean error is calculated on registrations obtaining a mean 2D Euclidean distance $< T$

Similarity measure	GI	GD	GC	NCC	MI
Success rate	138/285	239/285	99/285	27/285	45/285
Global mean error	2.94	2.32	3.34	3.53	3.46

The best results are obtained when using the GD with a success rate of 239 out of 285 registrations and a global mean error of 2.32 mm calculated on registrations achieving a mean 2D Euclidean distance below T , while NCC failed on achieving a significant success rate (27 out of 285 registrations). (*Figure 25*) shows the registration result when using GD and NCC. The average computation time for one registration, while using HVS with GD, was 25s.

The second experiment is performed to see how much the registration result can be influenced by the input vascular-structure. In this case the HVSS was used, along with the finest similarity measure (*i.e.* GD). By adding the splenic to the input vascular-structure, we have observed a decrease of the success rate to 68 out of 285 registrations, highlighting the dependence of the registration precision to the used input structure.

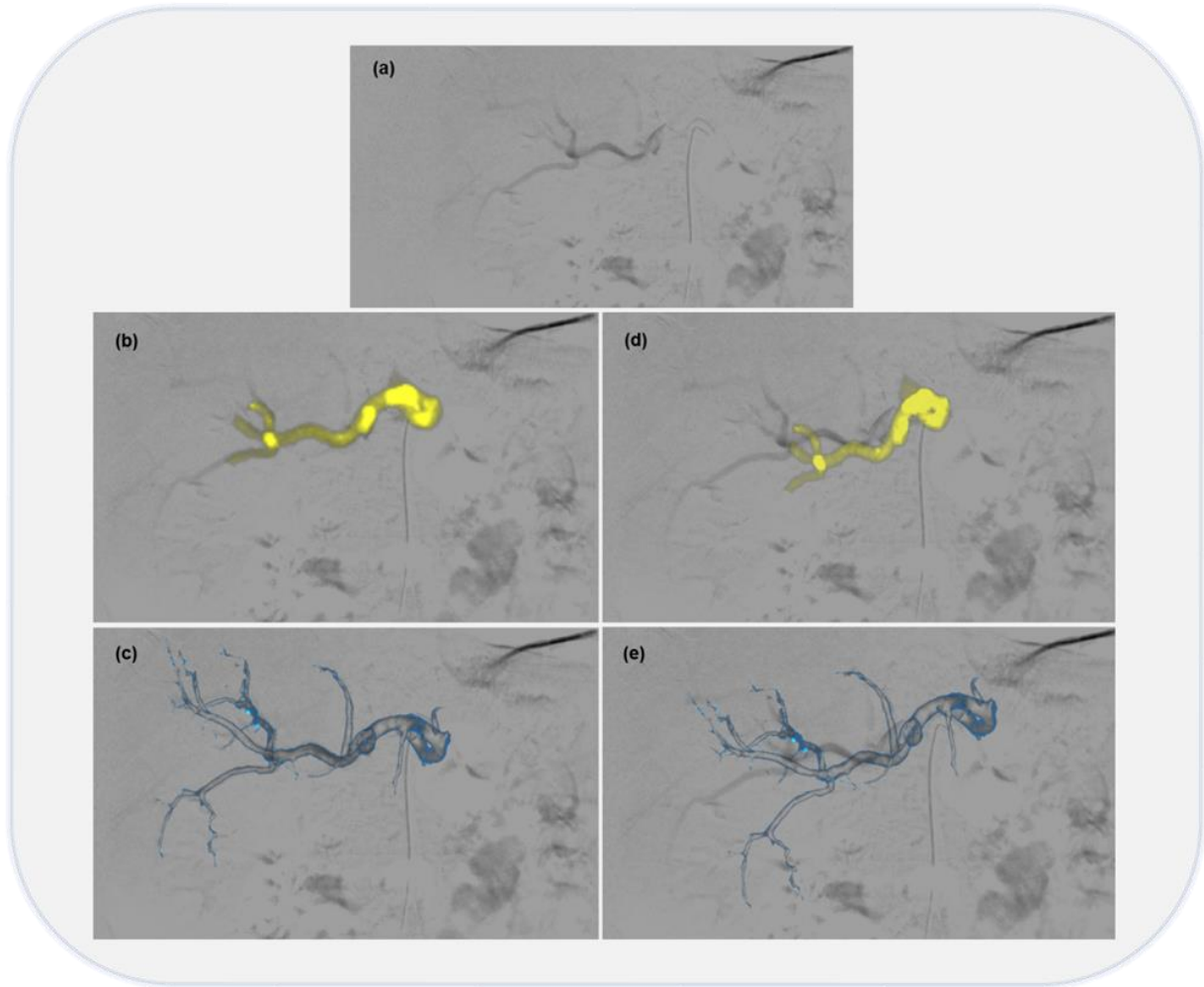


Figure 25 - Influence of the SM on vessel-based registration. The DSA (a) and the HVS are correctly registered with GD (b). A good anatomical correspondence is obtained when projecting the hepatic arterial tree (c). The registration result is degraded with NCC (d).

2.4 Discussion and conclusion

Manipulating the catheter and mapping the hepatic arterial tree remains a challenging task. Up to now, radiologists refer to their capacity to mentally construct a 3D vasculature from repeated 2D angiogram acquisitions in order to access the injection site. A poor perception of the anatomical structures can result in inadequate deposition of $^{90}\text{Y}/^{166}\text{Ho}$ agents in the considered lesion. In this chapter we have proposed a computer-assisted guidance strategy

designed to progressively augment the intraoperative X-Ray image. A structure-driven intensity-based rigid registration method is used at two different stages of the RE intervention to augment the intraoperative image with additional relevant information. First, the aorta and the origins of its side branches are projected on the intraoperative 2D fluoroscopy following a 3D/2D bone-based registration process, to assist the celiac trunk access. Subsequently, a similar approach consisting in projecting the hepatic vasculature on intraoperative DSA through 3D/2D vessel-based registration is performed to assist the injection site location. This approach is able to ensure a reliable catheter manipulation and has the potential to reduce the contrast product administration and the radiation exposure.

The two fusion steps (*i.e.* bone-based registration and vessel-based registration) presented in this chapter were independently evaluated on subsets of 20 and 19 patient cases, respectively. The approach resulted in qualitatively appropriate anatomical correspondences when projecting the preoperative structures on intraoperative images. With the best configuration, the registration steps showed accuracy and feasibility in aligning data, with global mean landmarks errors of 1.59 mm and 2.32 mm, respectively, a computation time that never exceeded 5 s and 25 s, respectively, and a user interaction limited to manual initialization of the 3D/2D registration. The preprocessing of the CTA can be performed before the scheduled procedure and may not require more than 10 min.

The accuracy and precision of the two fusion steps would benefit from the similarity measure selection. In this context, gradient information, gradient correlation, normalized cross correlation and mutual information, produced relatively dissatisfying results, whereas gradient difference (GD) yielded better robustness so far (*i.e.* success rate of 274/300 registrations where mean 2D Euclidean distance <5 mm for the bone-based registration and success rate of 239/285 registrations where mean 2D Euclidean distance <5 mm for the vessel-based registration).

Regarding the vessel-based registration, we assume that non-rigid deformations are negligible for two reasons: the central part of the liver (where the injection site is generally located) is almost rigid and the flexible micro-catheter pressure is not able to deform the arteries. Taking advantages of a vascular-structure that is the least likely to deform (*i.e.* HVS) enables the

Discussion and conclusion

registration method to be performed correctly. It was noticed that the use of HVSS as a preoperative input structure, containing the deformable splenic artery which does not generally appear in the DSA, deteriorates the registration. To properly define the preoperative structure, it is necessary to favor the rigid structures as well as the structures which appear in the intraoperative image, such as HVS.

3 Treatment intervention guidance: injection site reproduction

The treatment intervention is generally performed one to two weeks after the pretreatment assessment intervention for the delivery of $^{90}\text{Y}/^{166}\text{Ho}$ microspheres. These therapeutic microspheres are selectively injected into the hepatic feeding arteries of the tumor in order to retrograde the blood flow and emit a high radiation dose that is able to treat the cancer cells.

$^{90}\text{Y}/^{166}\text{Ho}$ injection site is located beforehand during the pretreatment assessment intervention and its position is validated by the administration of $^{99\text{m}}\text{Tc-MAA}$ and SPECT/CT acquisition, as evoked in Chapter 1. An optimal determination of the injection site results in an adequate deposition of $^{90}\text{Y}/^{166}\text{Ho}$ in the considered cancer tumor(s). Hence, the confirmed injection site has to be carefully reproduced during the treatment intervention for the delivery of a proper $^{90}\text{Y}/^{166}\text{Ho}$ activity.

Similar to pretreatment assessment intervention, the treatment intervention is performed in an interventional radiology suite under X-Ray image guidance acquired with a C-arm system, providing insufficient information for intraoperative catheter manipulation.

In addition to catheter manipulation challenges which we have dealt with in Chapter 2, radiologists find difficulties in reproducing the injection site. In fact, in order to prevent dose distribution deviations, the injection site should be reproduced as identically as possible.

In this chapter, we intend to introduce and evaluate the third fusion step integrated within our guidance strategy, proposed to simplify the catheter manipulation and automatically reproduce the injection site during the treatment intervention.

3.1 2D/2D Registration approach

During the treatment intervention, radiologists generally re-locate the injection site (IS) while mainly resorting to fluoroscopic images acquired during the pretreatment assessment intervention when the catheter is being inserted in the IS (*Figure 26*).

Besides catheter manipulation requiring, in this case, the radiologist's ability to understand the vasculature and efficiently manipulate the catheter inside, a misunderstanding of the anatomy can result in inappropriate IS reproduction and thus an inadequate deposition of $^{90}\text{Y}/^{166}\text{Ho}$ agents in the considered lesion.

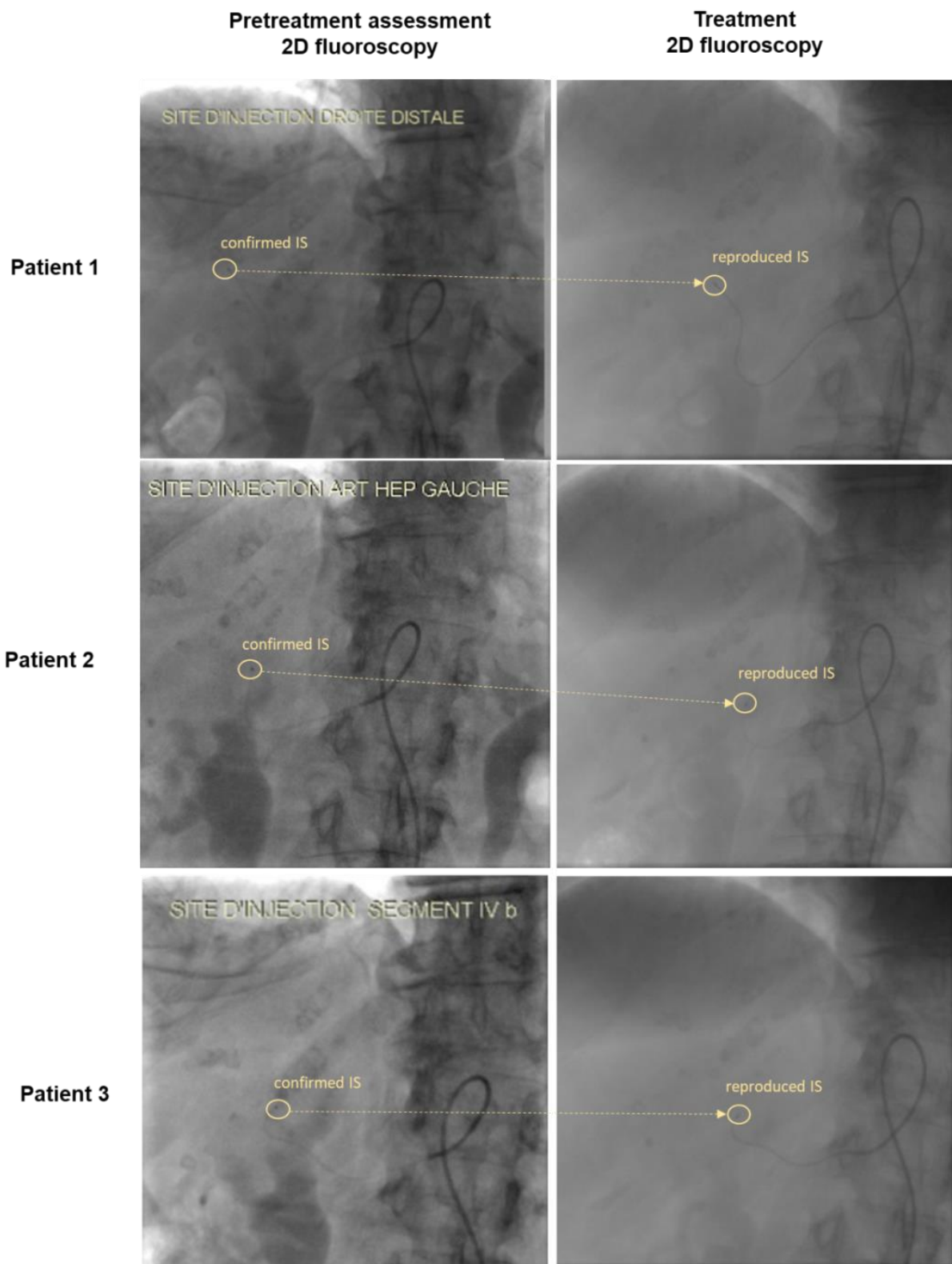


Figure 26 - Injection site reproduction in treatment intervention.

Catheter manipulation assistance can be performed by augmenting intraoperative 2D X-Ray images by the corresponding anatomical structures extracted from preoperative CTA through 2D/3D intensity-based registration as described in Chapter 2, especially that this approach showed accuracy and feasibility.

Localizing the IS in the 3D CT volume from the 2D pretreatment assessment fluoroscopic image through back-projection has the potential to effectively reproduce the IS.

Knowing that the C-arm angulation remains the same in the two interventions (pretreatment assessment, treatment delivery) and in order to avoid performing an additional back-projection step, in our work, we propose to align the 2D pretreatment fluoroscopic image with the intraoperative 2D treatment fluoroscopy by performing a 2D/2D registration (*Figure 27*). Subsequently, in order to have a more comprehensive rendering, the catheter is segmented from the moving image (i.e. pretreatment registered fluoroscopy) and reproduced onto the intraoperative image. At this stage, the catheter segmentation has been performed manually. The catheter visualization could simultaneously and in a reduced time help on specifying the catheter path, the celiac trunk origin position and the IS location, presenting a substantial added-information.

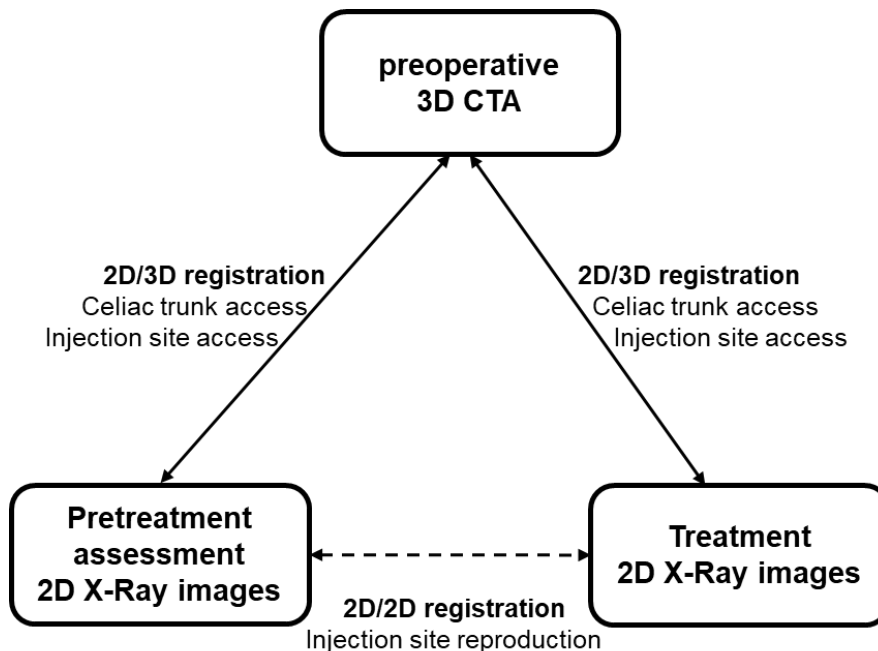


Figure 27 - Injection site reproduction strategy.

Several 2D/2D registration approaches can be performed in order to integrate information (i.e. catheter path) gained from 2D pre-treatment assessment fluoroscopic images to obtain an improved feedback and a more comprehensive understanding of the intraoperative treatment fluoroscopic images. In the literature, 2D registration approaches are widely introduced in the context of visual tracking, a computer vision research area that lie in estimating an object's motion and localizing it in an image sequence. Tracking-by-registration [84]–[86] consists in tracking the object of interest by iteratively registering pairs of consecutive images. In this context, 2D/2D registration approaches used for object tracking can be classified according to the type of information to be used: feature-based and intensity-based. Feature-based approaches consist in extracting a set of distinguishable geometrical features such as points of interest [87], dots [88], segments [88]–[90], straight lines, ellipses [91], contours [92] and angles from the current frame and matching them with features extracted from previous frame through a specific matching approach such as RANSAC. In some complex situations, more enhanced descriptors combining these features with other types of visual information can be used.

2D intensity-based registration approaches [93] consist in minimizing the error measurement (by either minimizing or maximizing a similarity measure) that is based on the intensity values to estimate the transformation that align each consecutive frame pair.

Thanks to the efficiency of the multi-resolution intensity-based approach previously demonstrated (chapter 2), in this chapter we propose to tailor the 3D/2D registration framework to align the 2D pretreatment fluoroscopic image with the intraoperative 2D treatment fluoroscopy (*Figure 28*).

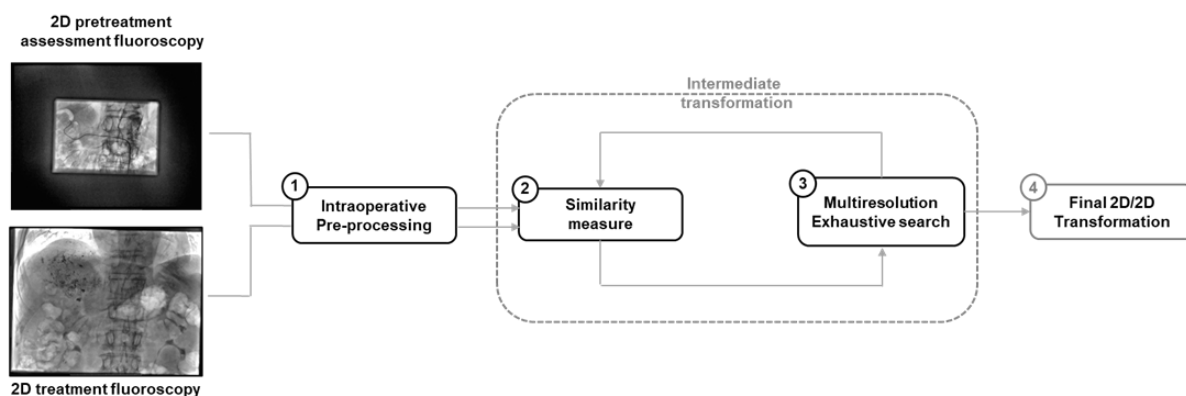


Figure 28 - Intensity-based registration framework with its main components. 2D pretreatment assessment and treatment fluoroscopic images are enhanced through preprocessing (1). 2D pretreatment assessment fluoroscopy is compared to the 2D intraoperative treatment fluoroscopy through a similarity metric presenting a quantitative criterion describing how well the input images are similar (2). For optimization, the 2D pretreatment assessment fluoroscopy is intermediately transformed following an exhaustive search and the transformation result is progressively refined following a multiresolution scheme (3). The final 2D/2D transformation corresponds to the transformation giving the best achieved similarity measure (4)

Similarly to the 3D/2D registration, we considered an optimized intensity-based 2D/2D registration approach performed following a multi-resolution scheme (Table 1). The algorithm is implemented to perform an exhaustive search of the pretreatment and treatment transformation. The optimal 2D/2D transformation is obtained following a multi-resolution coarse-to-fine registration between pretreatment and treatment fluoroscopic images acquired by a C-arm.

The multi-resolution scheme consists in progressively refining the transformation result. At each resolution level, the optimal transformation is estimated by performing a reduced exhaustive search that is limited to in plane transformation (with parameters t_x^i, t_z^i, r_y^i , subsection 2.1.2), that can be induced by the C-arm/patient positioning. Since the translation along y axis results in a scale factor in the 2D image plane, t_y^i is also considered to be an unknown parameter (scale parameter) in the registration process. It allows taking into account potential C-arm zoom actions or table height changes [45]. The parameter space of each transformation is sampled on a regularly discretized range and the different combinations of parameters T^i result in n transformations such that:

$$T^i = T(t_x^i, t_y^i, t_z^i, r_y^i); \quad i = 1, 2, \dots, n$$

A similarity measure is computed between the 2D pretreatment and treatment fluoroscopic images for each combination of the parameters. The optimal transformation corresponds to the combination of parameters giving the best similarity measure outcome. It is used as the initial solution for the next resolution level.

3.2 Experiments

2D fluoroscopic images contrast was enhanced primarily by applying a histogram equalization preprocessing. There was no manual initialization for the 2D/2D registration. The parameters of the initial transformation were fixed to 0.

Before assessing the registration method accuracy, preliminary tests were performed to set the exhaustive search parameters (*Table 5*).

Table 5 - Parameters used during the optimization phases (r = resolution of the discretized range of the parameters)

Step	In-plane translation (mm)		Scale parameter (mm)		In-plane rotation (°)	
	Range	R	Range	r	Range	r
1	[-20;20]	2	[-5;5]	2	[-5;5]	1
2	[-5;5]	1	[-5;5]	1	[-2;2]	0.5
3	[-3;3]	0.5	-	-	[-0.5;0.5]	0.5

In general, distance between corresponding points in the two registered images is a preferred measure of 2D rigid registration evaluation as it is considered as one of the most reliable ways of quantifying accuracy. Used points can be anatomical landmarks or tailor-made markers. As markers are not available in our context, we have recourse to anatomical landmarks-based analysis for evaluation. Consequently, we have asked experts to manually define eight corresponding points in each image pair to be registered with accuracy. All points belong to the spine structure, which is visible in both images.

In this context, we have evaluated the 2D registration accuracy while investigating the effect of different similarity measures [70] on the registration outcome. As for chapter 2 studies, Gradient information (GI), gradient difference (GD), gradient correlation (GC), normalized cross correlation (NCC) and Mutual information (MI) have been tested.

In order to measure the transformation result accuracy by considering a specific similarity measure, a global mean error corresponding to a mean Euclidean distance has been calculated between the corresponding defined 2D points.

In the following, we present the clinical data used for the evaluation and report the 2D/2D registration results related to IS reproduction.

Clinical data

The proposed approach was tested and evaluated on 5 patient cases who underwent 90Y RE interventions between August 2014 and February 2019 at Centre Eugène Marquis (Rennes, France). Multiple factors were taken into consideration for patient selection as described in [83]. The 2D X-Ray images (i.e. fluoroscopy) are provided within the standard imaging protocol. They were acquired intraoperatively during the pretreatment assessment intervention and the treatment intervention on a C-arm Artis Zeego (Siemens Healthcare, Forchheim, Germany) with 1149 mm source to detector distance and 0.3729 x 0.3729 mm pixel size.

3.3 Results

In order to evaluate the method performance, an available sub-dataset of five fluoroscopic image pairs has been used.

In (*Figure 29*), we show the 2D/2D image-based rigid registration method results when varying similarity measures. For all image pairs, and by calculating the Euclidean distance between corresponding marked points, we have observed that the global mean landmark error varies from 1.08 mm to 3.51 mm. The method was successful on registering images when using GD with a global mean landmark error of 1.08 mm, calculated on all patient cases. The average computation time for one registration was 11 s on an integrated Intel graphic GPU Nvidia quadro k420 machine.

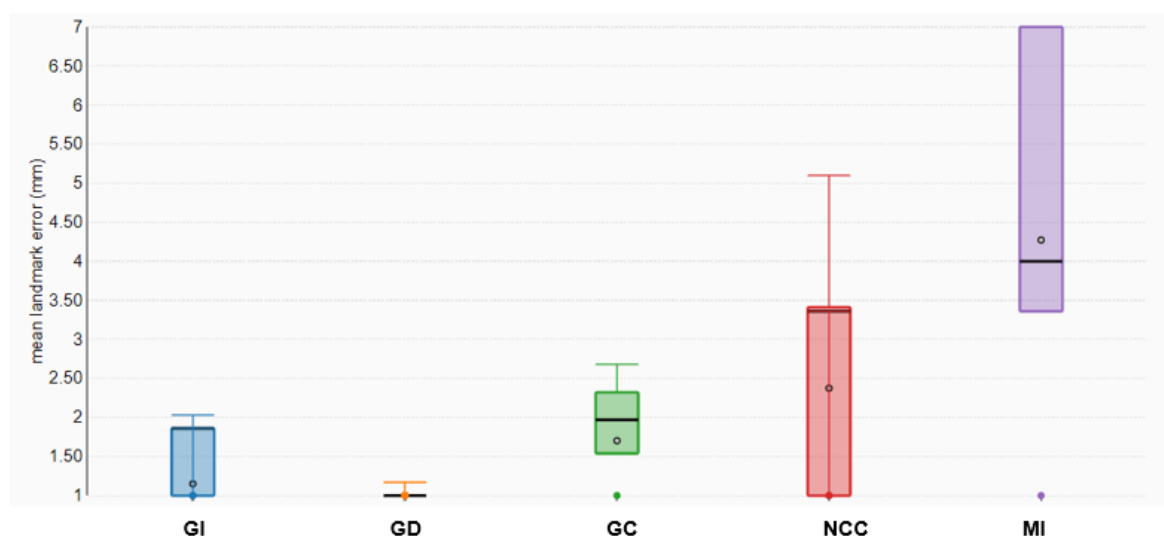


Figure 29 - Boxplot of the mean landmark errors obtained with GD for image-based registrations

As shown in (Figure 30) the registration does not seem to be disrupted by the presence of the catheter presenting in the pretreatment captured fluoroscopy.

In order to have a comprehensible rendering, we have manually segmented the catheter from the moving image (i.e. pretreatment registered fluoroscopy) and reproduced it onto the intraoperative image (Figure 31). The catheter visualization could help on specifying the catheter path, the celiac trunk origin position and the IS location, presenting a substantial added-information.

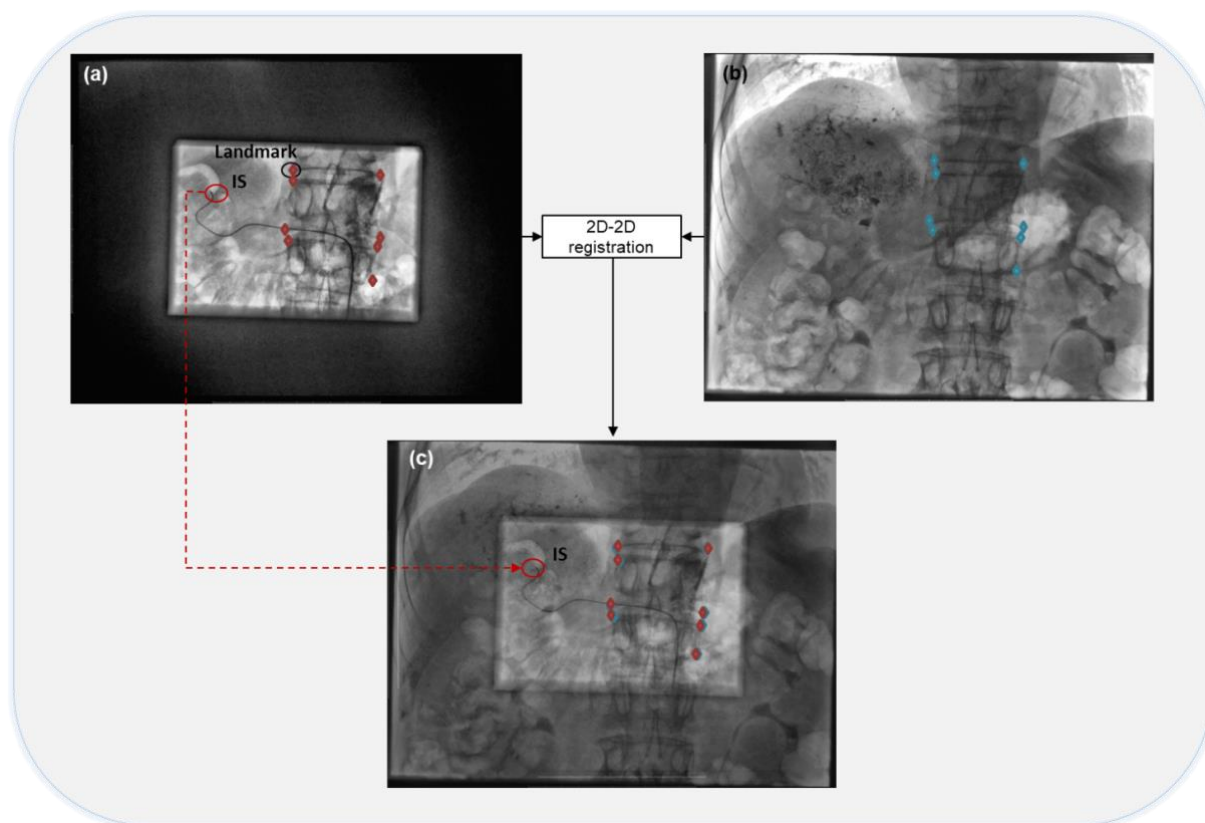


Figure 30 - Marked-based evaluation. Pretreatment assessment fluoroscopy captured once the catheter reached the injection site (a) is registered to the intraoperative real-time fluoroscopic image (b) during the treatment intervention. The registration results in a reproduction of the catheter path as well as the IS (c). Marked points (red colored points in (a) and blue colored points in (b)) which are defined by expert are highlighted in the images



Figure 31 - Pretreatment catheter path reproduced in treatment fluoroscopic image. Intraoperative real-time fluoroscopic image (left) is augmented with the pretreatment catheter segmented from the transformed preoperative fluoroscopy (right)

3.4 Discussion and conclusion

During the treatment intervention, reproducing the predefined injection site with precision is still a challenging task for radiologists till now. While automatically reproducing the IS has not been studied in the literature, in this chapter we have extended our guidance approach to propose an automatic IS reproduction by augmenting treatment intraoperative 2D fluoroscopic image with the catheter path extracted from pretreatment assessment fluoroscopy.

The augmentation of the intraoperative 2D fluoroscopic image with the catheter path extracted from pretreatment assessment fluoroscopy has been performed by employing 2D/2D image-based registration between pretreatment and treatment fluoroscopic images. This approach was evaluated on a subset of 5 patient cases. The fusion step showed accuracy and feasibility in aligning data, with global mean landmarks error of 2.17 mm, a computation time that never exceeded 11 s, and without any user interaction.

Through performed experiments, we observed that the accuracy and precision of 2D/2D registration would benefit from the similarity measure selection. Gradient information, gradient correlation, normalized cross correlation and mutual information, produced relatively dissatisfying results with our data, whereas gradient difference yielded better robustness so far (*i.e.* global mean landmark error of 1.08 calculated on five patient cases).

By using the gradient difference, the 2D/2D rigid transformation model has proven to be sufficient on registering pretreatment assessment and treatment fluoroscopic images. The projection of the catheter, as shown in this chapter, seems to be accurate to assist the catheter manipulation and reproduce the IS and therefore, reduce the contrast product administration, the radiation exposure and inadequate deposition of $^{90}\text{Y}/^{166}\text{Ho}$ risk.

To summarize the computer-assisted navigation approach developed in this thesis until now, *Figure 32* gives an overview of the different fusion steps involved in RE pretreatment assessment intervention (celiac trunk access, injection site access) and treatment intervention (injection site reproduction). Although for the treatment intervention guidance we have focused on the reproduction of the injection site, the celiac trunk access can be assisted through the representation of the pretreatment catheter path. It could be also assisted by the

augmentation of X-Ray fluoroscopy with the aorta and the celiac trunk origin as proposed for the pretreatment assessment intervention.

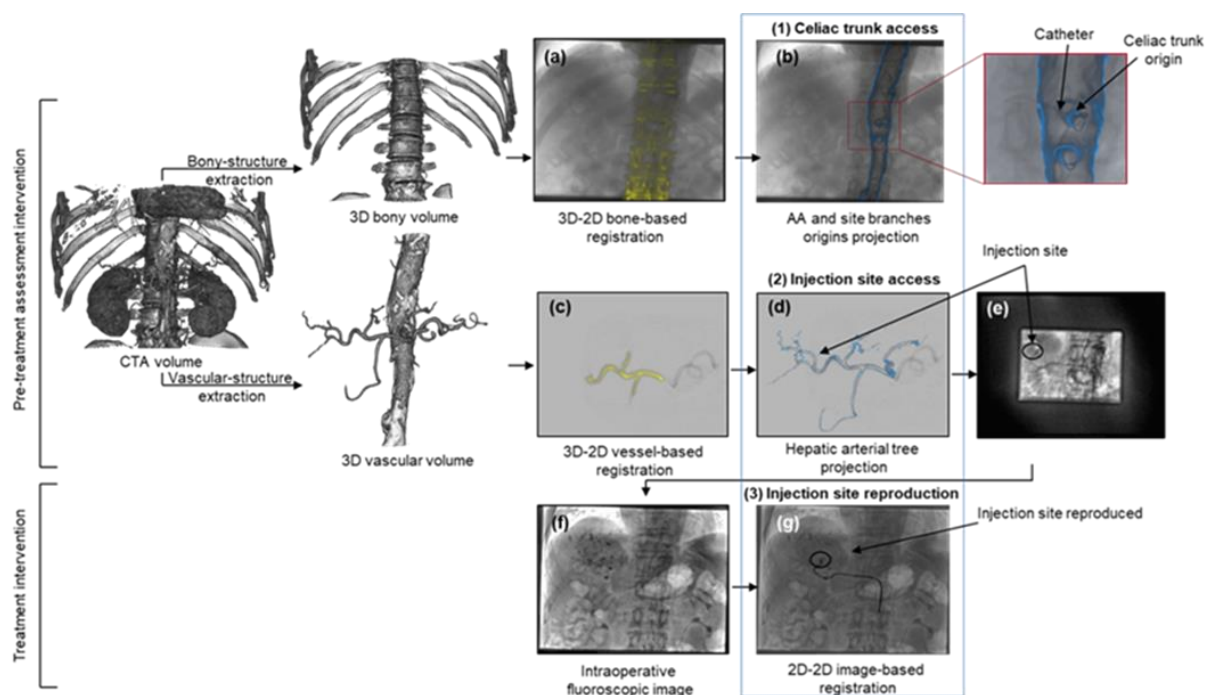


Figure 32 – Overview of proposed navigation approach. Preoperative arterial phase Computed Tomography (CTA) images are semi-automatically segmented using endosize®, obtaining either a 3D bony or delimited vascular volume. During pre-treatment intervention, the CTA is firstly registered to the real-time fluoroscopic image based on the bony-structure (a), and the abdominal aorta (AA) as well as the celiac trunk and the superior mesenteric origins are projected to assess the celiac trunk catheterization (b). At the level of the celiac trunk, a contrast product is injected and a DSA is acquired and registered to the CTA based on a delimited vascular-structure (c), and the hepatic arterial tree is projected to assess the IS access (d). Once reaching the IS, a fluoroscopic image is captured (e), and registered to the real time fluoroscopic image during the treatment intervention, to assess the IS reproduction (f, g).

4 Hepatic arterial tree repositioning

Static virtual roadmap of hepatic vasculature, *i.e.* resulting from the registration of preoperative CTA and intraoperative angiographic images (as described in chapter 2), may add relevant information and provide a more comprehensive feedback of the interventional scene in radioembolization procedures. Abdominal organs, including the liver, change their positions continuously due to the patient's respiration. The proposed radioembolization image-guided approach could be improved by a dynamic roadmap. It has to take into consideration the displacement through a continuous update of the spatial alignment of the preoperative hepatic vasculature with the intraoperative hepatic vasculature position (not visible in the fluoroscopic images).

The roadmap real-time repositioning can be handled in different manners. In this chapter, we provide an overview of dynamic roadmap approaches for improved image-guidance and we expose our proposed approach being used to reposition the hepatic arterial tree in the intraoperative 2D fluoroscopic sequence.

4.1 Dynamic roadmap correction

Radioembolization intervention is performed under live 2D X-Ray fluoroscopy guidance, displaying the catheter movement in real-time (7-8 frames per second) without the visualization of arteries, unless a contrast medium is injected. With the projection of a static roadmap of hepatic vasculature resulting from the registration of preoperative CTA and intraoperative angiographic images, the catheter is almost displayed outside the projected vasculature, due to the respiratory motion causing a continuous vasculature displacement. Despite the advantages of the static projection of the hepatic arterial tree, interventional radiologists still have to mentally reposition this roadmap while navigating the catheter.

Real-time visual integration of projected roadmap on live 2D X-Ray fluoroscopy can further facilitate the catheter navigation procedure by allowing for continuous visualization of the hepatic arterial tree without injection of contrast medium. Our method should estimate the vessels motion through appropriate information and correct the hepatic roadmap with accuracy and speed, as two important aspects of performance in the context of RE image guidance.

4.1.1 Related works

Continuous roadmapping approaches have been introduced for the guidance of interventions especially in which static roadmaps are hampered by respiratory motion. YingLiang Ma et al. [64] proposed initializing the cardiac anatomical roadmap by using manual calibration-based methods and correcting the respiratory motion by using some specific features such as: heart border, diaphragm, tracheal bifurcation and catheter. Except the catheter, only the diaphragm structure is visualized in radioembolization 2D X-Ray fluoroscopy. Yang et al. [94] have analyzed the correlation between the liver tumor and diaphragm motion in three directions (SI, AP, and ML). Their study led to the fact that the diaphragm motion can be a good surrogate of the liver tumor motion in only SI and AP directions, and this concordance is affected by the distance between the tumor and the diaphragm. In the other hand, Davies et al. [95] have calculated displacement values of the entire liver and the diaphragm in SI direction during the respiration and concluded that for a same patient the displacement value of the diaphragm is different from that of the liver (e.g. 12 ± 2 vs. 18 ± 3 mm, respectively). Through these studies, it can be concluded that the diaphragm provides inappropriate information for estimating the liver motion and correcting the hepatic roadmap in radioembolization context. The roadmap position update based on catheter information has been a center of interest for many researchers. In percutaneous coronary interventions, to perform dynamic coronary roadmapping on free breathing, Hua Ma et al. [96] proposed to compensate the respiratory-induced vessel motion via catheter tip tracking in X-Ray fluoroscopy. Their roadmapping approach was validated on clinical data, achieving accurate performance.

In the context of chemoembolization, Ambrosini et al. [29] have proposed a real-time catheter segmentation followed by 2D/3D registration for continuous roadmapping (*Figure 33*). Their registration approach is highly dependent on the segmentation accuracy, a complex task by definition especially for intraoperative variable scenes. Another source of error is related to that their registration is performed on a vessel centerline running from the aorta to the hepatic vessel extremity, unsuccessful for cases presenting a lack of information in 3DRA (missing aorta and hepatic artery) or 2D X-Ray (when only short part of the catheter is visible). In order to correct the roadmap for hepatic artery catheterizations, Atasoy et al. [62] proposed a semiautomatic method consisting in 1) performing a rigid 2D/3D pre-registration using

machine calibration, 2) tracking the catheter by following one moving region of interest belonging to the 2D catheter visualized in 2D X-Ray and manually selected by the physician, and 3) updating the registration with this information. The tracking is performed using template matching with a translational motion model (Figure 34). Despite the manual interaction which is imperfect by definition, their motion model limited to in-plane translation has been successful in correcting the displacements caused by the breathing motion.

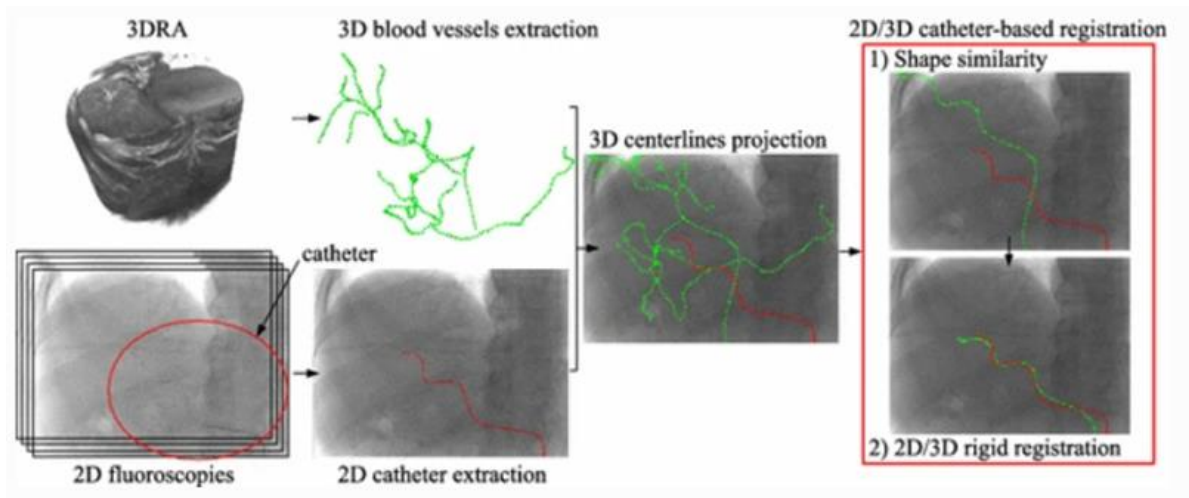


Figure 33 – Global overview: vessels/catheter extraction and 2D/3D registration. From [29].

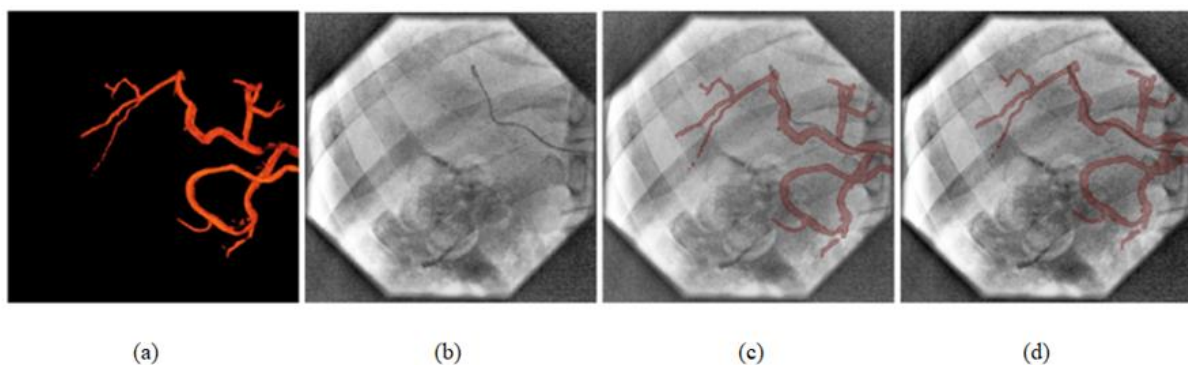


Figure 34 - roadmap correction for hepatic artery catheterizations. (a) displays the 3D static roadmap of the hepatic arteries. (b) shows a 2D fluoroscopy image. (c) illustrates the projection of 3D static roadmap onto a frame in the 2D fluoroscopy image sequence without motion correction. (d) indicates the projection of 3D static roadmap onto the frame with motion correction. From [62].

4.1.2 Liver motion and arterial deformation

The knowledge of a model for the liver displacement under respiratory motion can provide an important prior to estimate the motion of the liver vessels, and various studies have been performed to determine such a model.

Rohlfing et al.[50] inspected the transformation and deformation occurred during the respiration by performing rigid and non-rigid registration. They indicate that the dominant component of liver motion was cranio-caudal translation (12 to 26 mm). The same group reported that Left-Right translation was between 1 to 3 mm and the rotation did not exceed 1.5 degrees. By comparing the rigid and non-rigid registration, the same group estimated an average tissue deformation of 6 mm occurred in the liver periphery, while the rigid motion model accurately aligned the central part of the liver. Clifford et al. [47] provided an extensive assessment of the hepatic motion caused by respiration based on nine published studies. All mentioned studies agree that the most significant liver motion is cranio-caudal translation, with a translation ranging from 10 to 26 mm in quiet respiration. There exists a disagreement in the literature about the significance of Anterior-Posterior and Lateral translations. Although some studies indicate that the respiration causes a significant translation along the two axis, Korin et al. [97] suggested that clinically significant liver motion could be effectively approximated by only a cranio-caudal movement while completely neglecting other axis of motion. This assumption was sustained by Davies et al. [95].

Considering these studies and knowing that during radioembolization the patient is posed in supine position and the C-arm is set in anterior-posterior position (*Figure 35*), we approximate the displacement of the hepatic arterial tree due to the respiratory motion in 2D X-Ray fluoroscopy using a translational model that covers translations in x and y directions in the image plane. Assuming that the deforming effect of respiration on liver's central part is negligible, our approach does not take into consideration deformations.

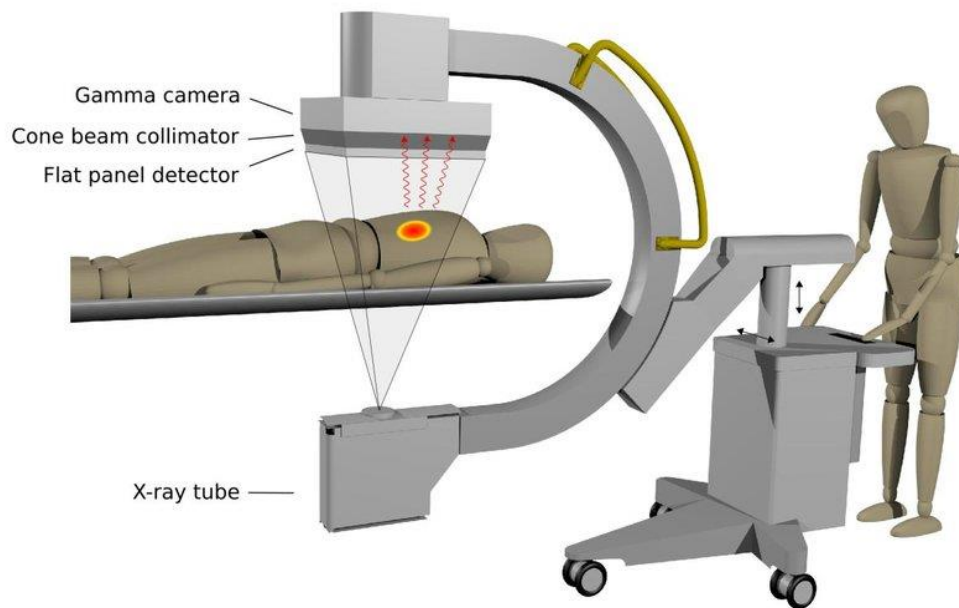


Figure 35 - Patient and C-arm positioning during radioembolization procedure. From [98].

4.2 Catheter tip tracking

4.2.1 Approximation of vessel motion by catheter motion

In radioembolization, as detailed in subsections 1.2.1 and 1.3.1, the trans-femoral catheter is threaded up to the aorta and selectively catheterizes the celiac trunk. The micro-catheter is then passed into the catheter, pushed through the common hepatic artery, and advanced eventually in the arterial supply of the tumor (*Figure 36*).

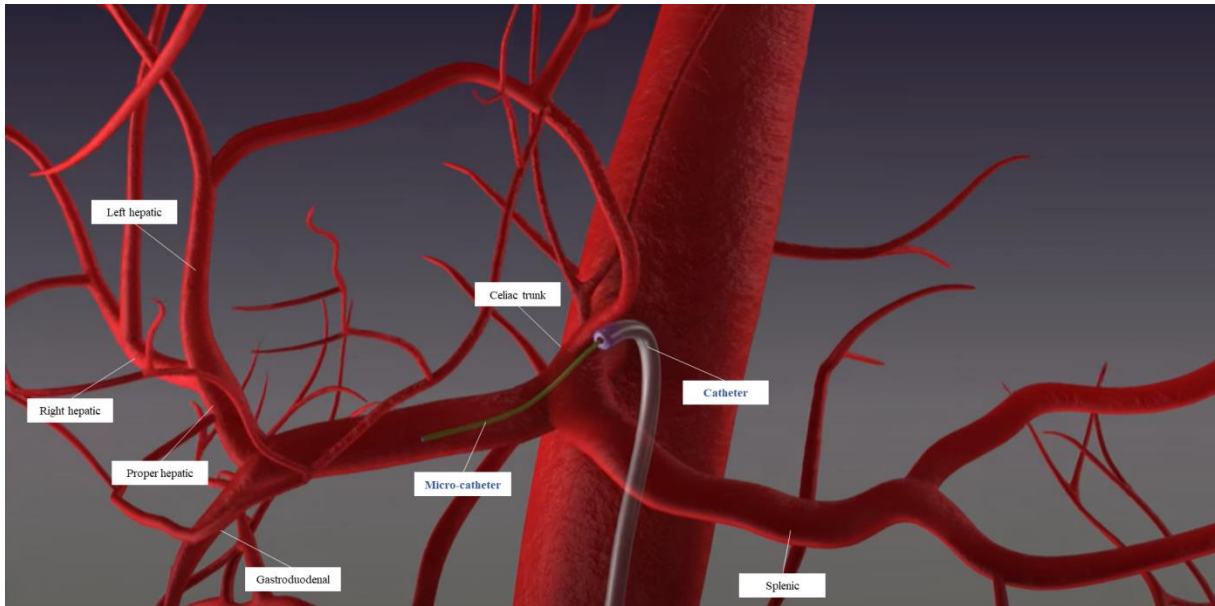


Figure 36 – Liver catheterization procedure in radioembolization

Since the catheter is located within the celiac trunk, we assume that its motion replicates the hepatic vasculature motion. In our study we attempt to approximate the hepatic vasculature motion in X-Ray fluoroscopy from the catheter displacement. Hence, in this work, we are interested in proposing a method that is able to track the catheter tip visualized in 2D fluoroscopic image sequences (*Figure 37*). The computed catheter motion can be then transferred to the projected static roadmap to adjust it and achieve more realistic vasculature visualization with respect to the current catheter position.

In this context we have to deal with two challenges: The proposed method must be robust to degraded imaging conditions (noise, low contrast) when tracking the catheter tip, and the location must be provided in real time with respect to the C-arm acquisition rate.

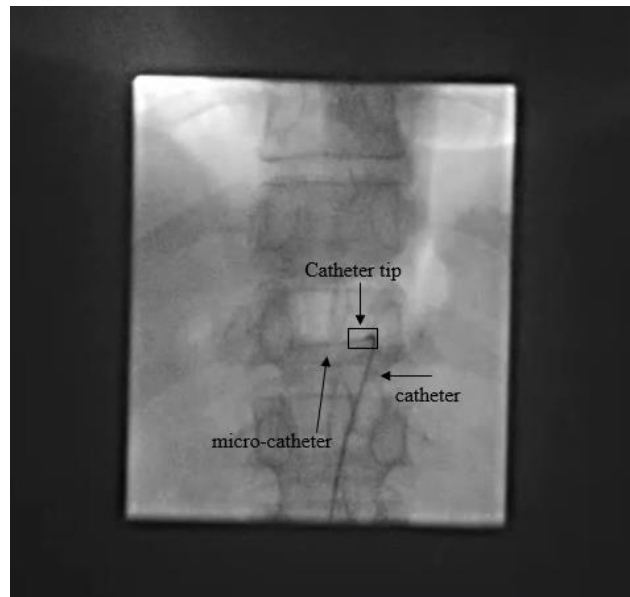


Figure 37 - X-Ray fluoroscopy visualizing the guiding catheter in radioembolization

4.2.2 Interventional tools tracking

Object tracking is one of the main research fields in computer vision, and is employed in many applications. The overall objective is to automatically identify and locate one or more targets from image sequence data. Since the application scenarios can be variable and sometimes complex, balancing the relationship between accuracy and computing time remains a difficult task.

Several studies have been performed to address the problem of interventional tools tracking in medical image sequences. Hua Ma et al. [96] have classified tracking methods into temporal tracking and tracking by detection approaches. Temporal tracking consists in locating an object or shape in an image by relying on its state in the previous images, by matching local features or global appearance between successive frames. In this context, Ambrosini et al [51] used a Hidden Markov Model (HMM) to track the catheter tip inside a 3D vasculature. Speidel et al. [99] have used particle filters to track surgical instruments in medical images. In order to track multiple instrument regions simultaneously, Speidel et al. [100] used multi-object particle filters, in which a particle represents a concatenation of several objects states. The main advantage of temporal tracking approaches relies on reducing the detection search

space in each frame, which makes tracking faster, whereas, a disadvantage of these methods rely on the error accumulation which can be produced by a tracking errors in each frame.

Instead, tracking by detections methods handle the problem as an object detection problem in each individual frame without considering previous frames outputs which prevent error accumulation caused by temporal tracking methods. In this context, Atasoy et al [62] have proposed template matching to track the catheter in X-Ray fluoroscopic sequence frames.

Convolution neural networks have emerged as solution for various visual tasks. They have received recently significant attention in medical image processing community due to their demonstrated potential for segmentation [101], recognition [102]. They have also proven to be effective in interventional instruments detection [103] [104] [105]in particular.

Some researchers suggest a combination of temporal tracking and tracking by detection. For example, in a recent work published in the context of PCI by Hua Ma et al. [96], authors combined particle filter with deep learning to track the catheter tip in X-Ray fluoroscopy.

In our context, the challenge especially lies in dealing with the appearance of the guiding catheter tip used in radioembolization fluoroscopic image, which consists in a thin dark tubular shape showing few prominent features (*Figure 37*). Hence, following the deep learning paradigm, we present, in this chapter, a novel hepatic arterial tree repositioning technique in intraoperative X-Ray fluoroscopy, based on real-time catheter tip tracking. In order to overcome these issues, our method relies on CNN to detect the catheter tip in each frame.

4.2.3 A CNN based tracking

The recent success of deep learning in computer vision has given rise to the development of methods based on Convolutional Neural Networks (CNN) for object detection, providing predictions of object class labels and bounding boxes in images. Among popular techniques can be mentioned the Region CNN based models (R-CNN [106], Fast R-CNN [107], Faster R-CNN [108]) (*Figure 38*) which rely on a set of extracted or learned and predicted relevant region proposals which are more likely to contain the object, and which have proven to be fast, especially Faster-RCNN. Classifying the object presence in these regions is performed

over features that are extracted by passing the regions through a CNN, while fitting a bounding box around the region proposals.

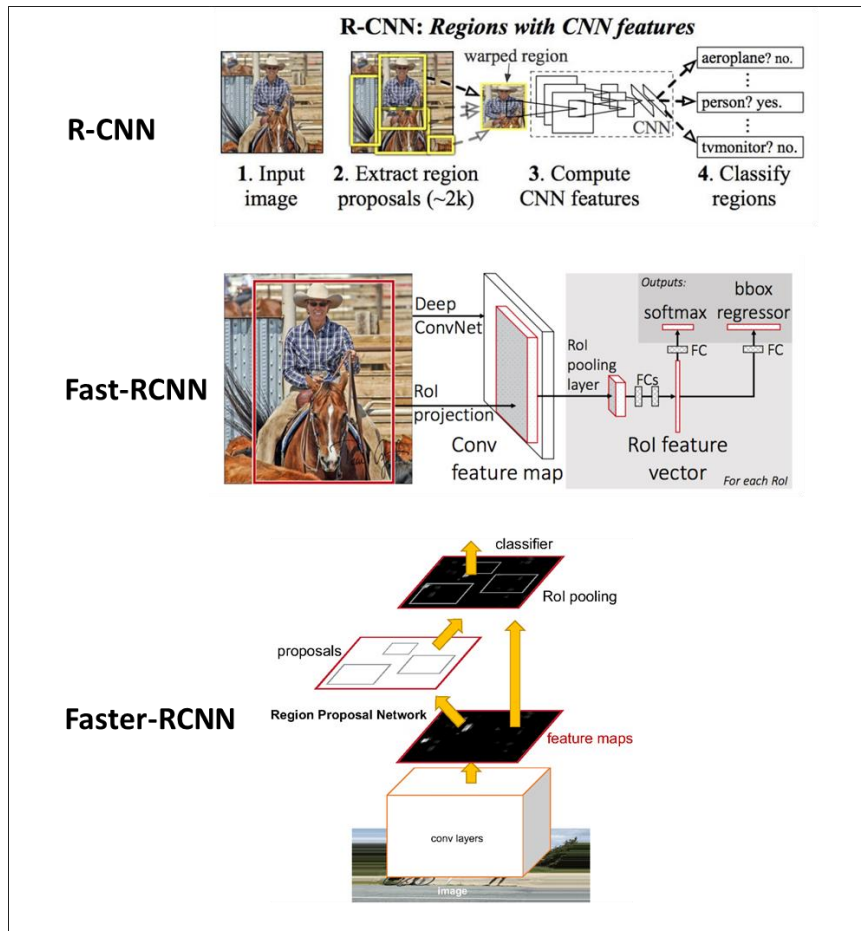


Figure 38 – R-CNN, Fast-RCNN and Faster-RCNN architectures [106]–[108].

Instead, the YOLO (You Only Look Once) approach, introduced by Redmon and al. [109] (Figure 39), does not process regions to localize the object but builds up a set of fixed anchor bounding boxes over each cell of a regular grid in the image, and provides a class probability and an offset for each bounding box, by passing through a single convolutional network. The object is then located by selecting the bounding boxes with probabilities over a certain threshold. W.r.t the R-CNN family, YOLO, as a single stage process, has proven to be faster and can be slightly more accurate [110]. It is however less robust in detecting neighbouring multiple instances, especially in the presence of background clutter. However, the problem consisting in detecting a single small catheter tip within an image showing few salient

background features, and in providing predictions in real-time within the sequence, we have employed the YOLO method in this work.

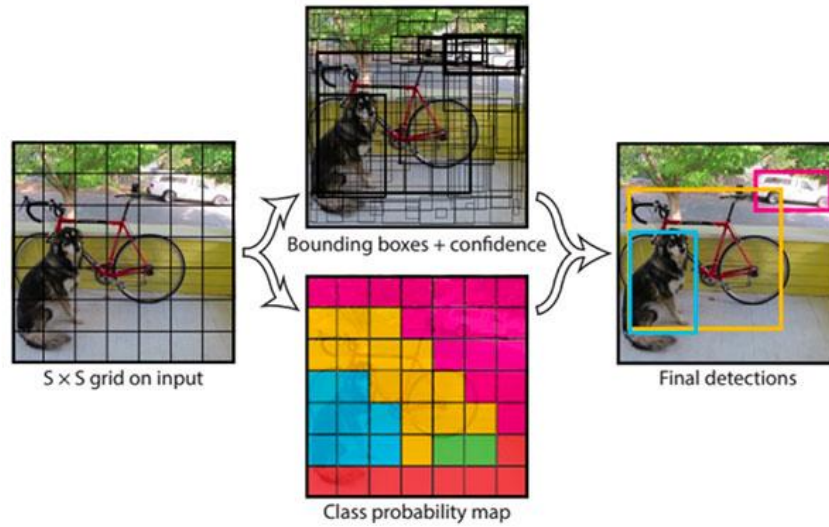


Figure 39 – Object detection using YOLO [109].

4.3 Experiments

We suppose that a continuous localization of the catheter tip may allow for continuous update of the hepatic arterial tree position. We assume that the link between the two structures (catheter tip and hepatic arterial tree) is maintained in the presence of the movement resulting from the respiratory motion. In this subsection, we present the qualitative and quantitative results obtained on real fluoroscopic image sequences for both catheter tip detection and hepatic arterial tree repositioning, in the context of radioembolization interventions.

4.3.1 Catheter tip detection evaluation metric

To evaluate the catheter tip tracking accuracy, we use Intersection over Union (IoU) (or Jaccard index) as it is considered as the most popular metric used for object detection evaluation. In the object detection scope, IoU is proposed to measure the similarity between the detection bounding box B_p and the ground-truth bounding box B_{gt} as illustrated in *Figure 40*, and defined by the following:

$$IoU = J(B_p, B_{gt}) = \frac{\text{area}(B_p \cap B_{gt})}{\text{area}(B_p \cup B_{gt})}$$

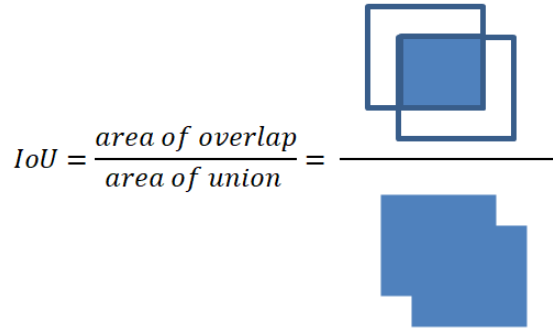


Figure 40 - Intersection over Union (IoU)

In our task, prediction boxes correspond to YOLO outputs and ground-truth boxes are hand-labeled bounding boxes from the validation set that enclose the target object (i.e. the catheter tip) to be detected. In order to get ground-truth, we have used annotation software.

The proposed catheter tip detection method is also evaluated by comparing the automatically tracked trajectories to the manual locations and computing the mean Euclidean distance between both.

4.3.2 Hepatic arterial tree repositioning assessment

Arterial tree repositioning is initialized with the 3D/2D structure-driven registration method described in chapter 2, performed between the preoperative 3D CTA and the intraoperative 2D DSA acquired when the catheter tip is positioned at the level of the celiac trunk. The resulting projection position is corrected and updated in the fluoroscopic image based on the catheter tip detection. Structure repositioning is evaluated by assessing if the micro-catheter is continuously superimposed by the projected displaced structure. For evaluation, we have recourse to an Inclusion Rate (IR) calculated on micro-catheter points. The IR corresponds to the ratio of points belonging to the micro-catheter in the image which are included within the projected boundaries of the hepatic arterial tree. Selected points belonging to the micro-

catheter are equidistant (distance between points = 10 pixels), an example is illustrated in *Figure 41*.

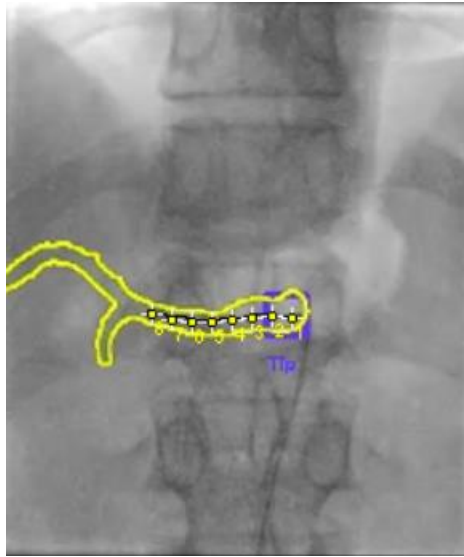


Figure 41 – Inclusion Rate (IR) calculation in a single frame: micro-catheter used points

4.4 Results

4.4.1 Clinical data and dataset composition

We have tested and evaluated the overall approach (catheter tip detection and hepatic arterial tree repositioning) on two real fluoroscopic sequences which were acquired intraoperatively during radioembolization for two different patient cases. Fluoroscopic sequences are anonymized and named RE 01 and RE 02, respectively. The acquired fluoroscopic frames have typical sizes of 512x512 pixels with an acquisition rate of 8 frames per second. The pixel size is 0.26 mm.

To create our YOLO training model, 900 image frames were extracted from other four different patient X-Ray fluoroscopic sequences, then the visualized catheter tip is labeled in each frame to provide its bounding box and position.

Dataset annotation was a crucial step in our task. It consists on manually locating the region of interest (catheter tip in our case) in each image frame by drawing bounding boxes and labeling those using annotating tools. We have used *Labelimg*, an open source annotation software (*Figure 42*). *Labelimg* provides two txt format files, the first file contains the object

classes defined by the annotators (several classes can be defined) and for each annotated image a file is generated containing a series of information as follows:

`<object-class> <x> <y> <width> <height>` where:

Object-class refers to the location number of the class defined in the first file, x and y correspond to the drawn bounding box (labeled object) center coordinates and $width$ and $height$ correspond to the bounding box dimensions.

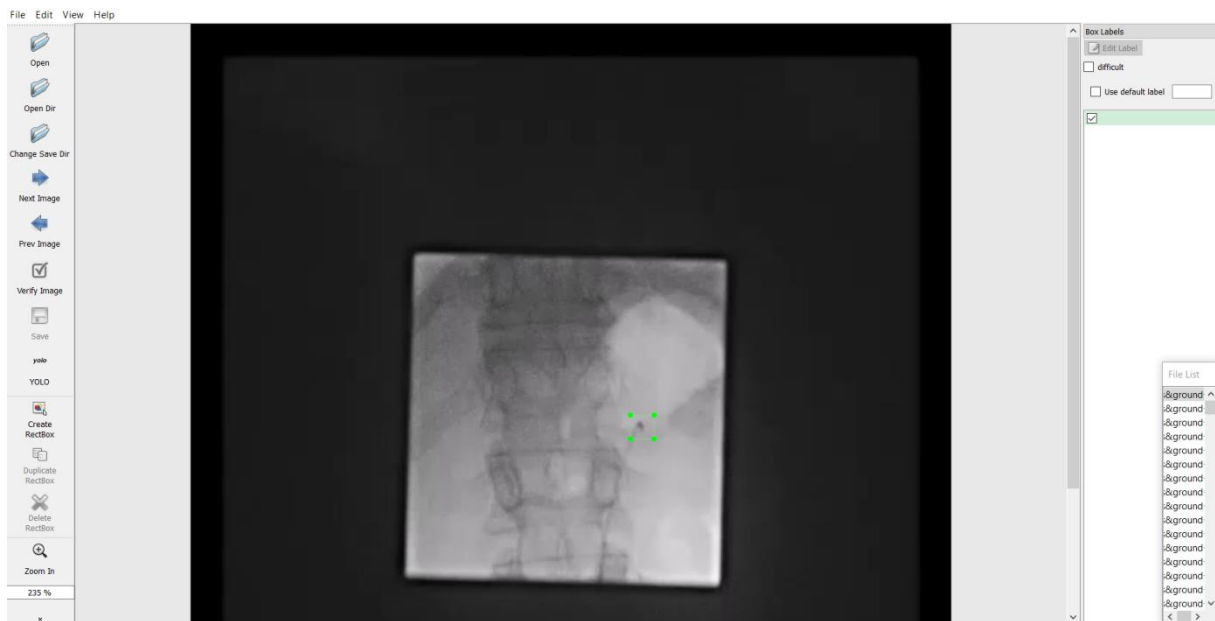


Figure 42 - image annotation using labelimg.

4.4.2 Catheter tip detection

The IoU values are calculated for the two sequences and represented in *Table 6*. For RE 01, the catheter tip detection has been successful in 359 out of the 409 frames (87%) (*Figure 43*). IoU values vary from 0.26 to 0.99 and the mean IoU is 0.74. For RE 02, the catheter tip detection has been successful in 292 out of the 440 frames (66%) (*figure 44*). For this same sequence, IoU values vary from 0.38 to 0.99 and the mean IoU is 0.69.

Results

Table 6 - catheter tip detection results

Sequence	Frames	Detection rate	IoU min	IoU max	IoU mean
RE 01	409	359 (87%)	0.26	0.99	0.74
RE 02	440	292 (66%)	0.38	0.99	0.69

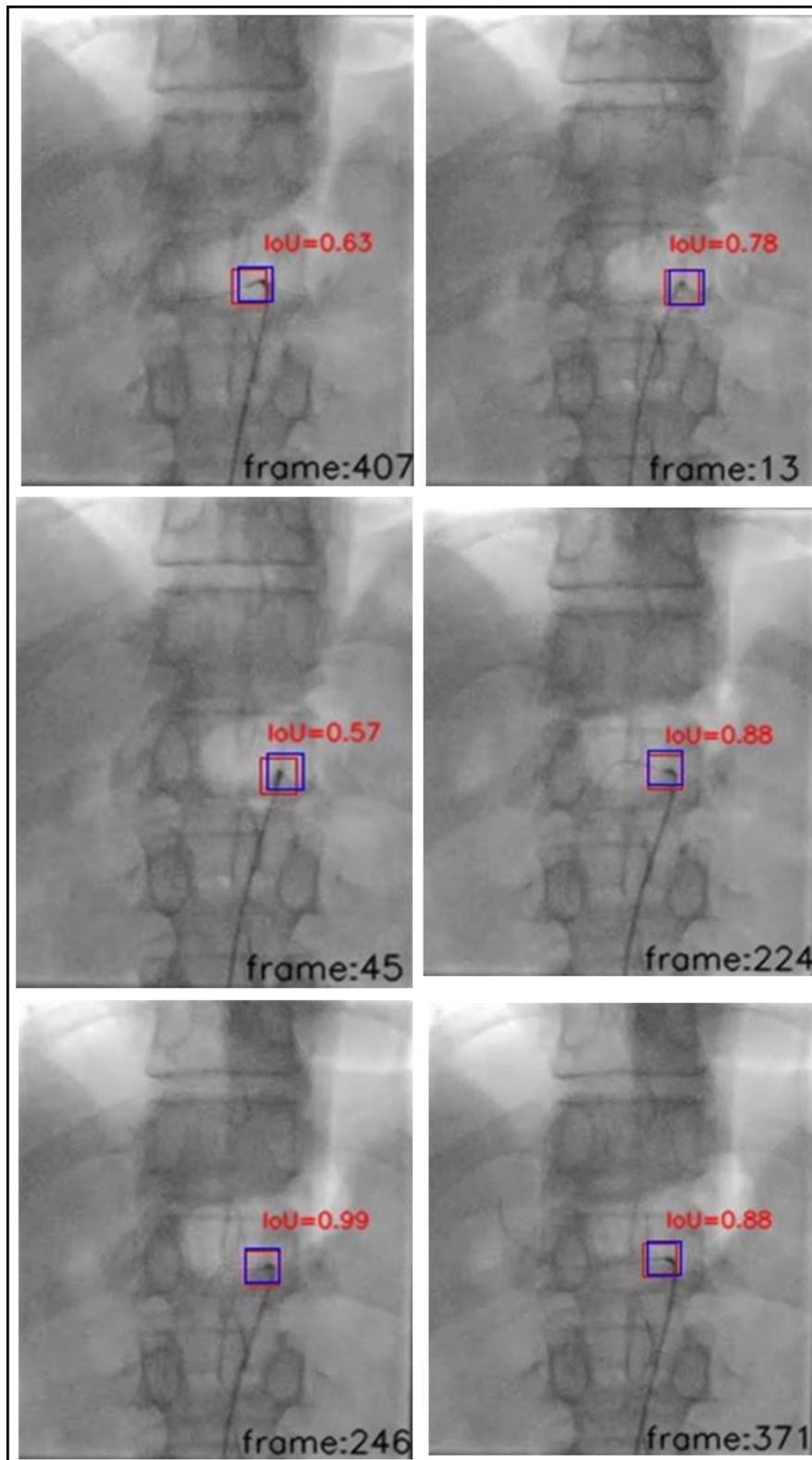


Figure 43 - IoU on different frames of sequence RE 01. Blue bounding boxes correspond to the ground truth whereas red bounding boxes correspond to the tracking output.

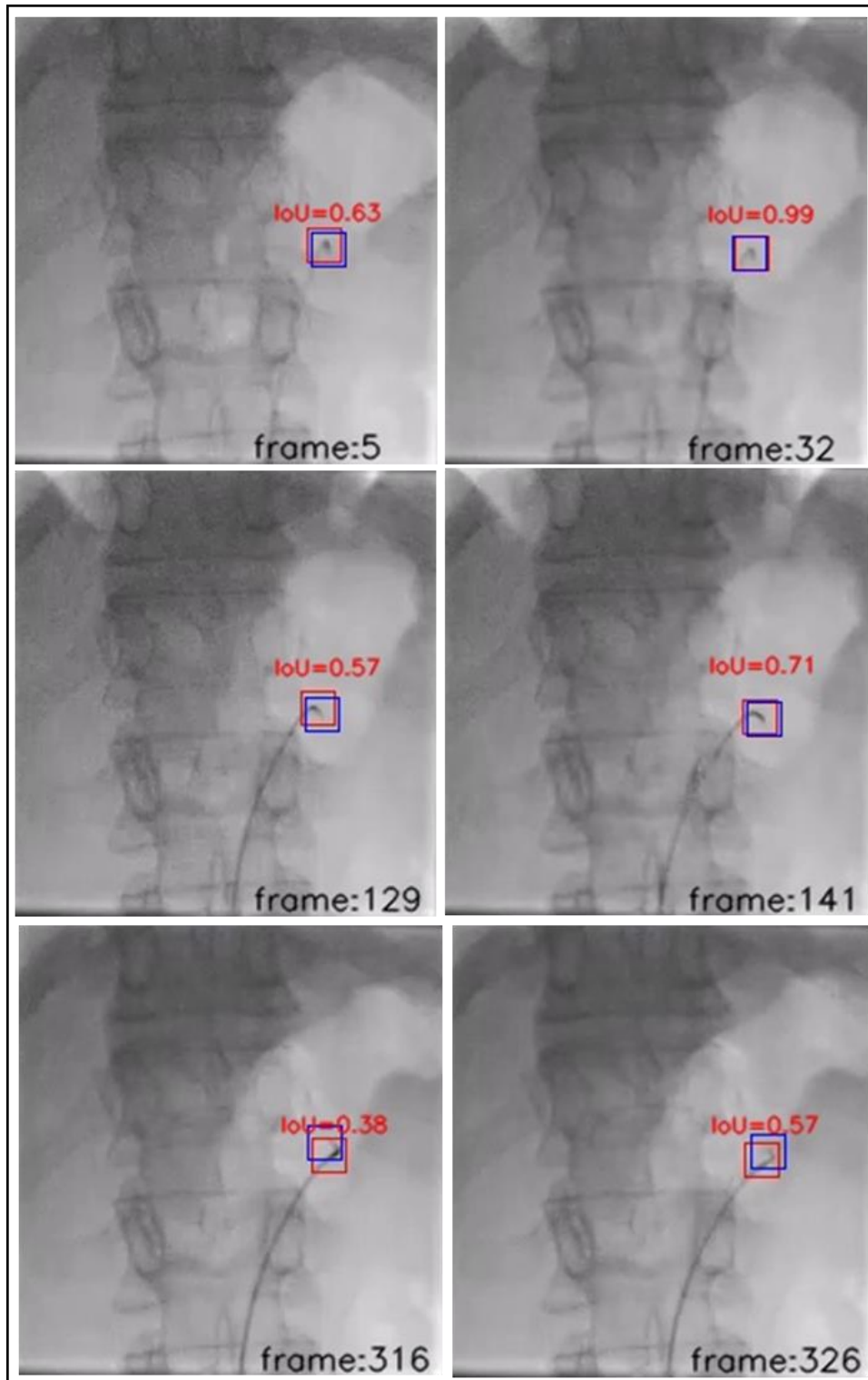


Figure 44 - IoU on different frames of sequence RE 02: Blue bounding boxes correspond to the ground truth whereas red bounding boxes correspond to the tracking output.

The tracking algorithm was not successful in detecting the catheter tip in some frames (13 % of the total number of frames in RE 01 and 34 % in RE 02). We mainly report these failures to the target low contrast (*Figure 45*). A possible solution to overcome this issue could consist in attaching a distinguishable radiopaque material to the catheter tip, so that it can be detected more easily in each frame.

Another source of error should be related to the limited annotated data used for the YOLO model training (i.e. only four sequences have been used for the training). More data would enable to better cover the variability of imaging conditions and catheter appearance.

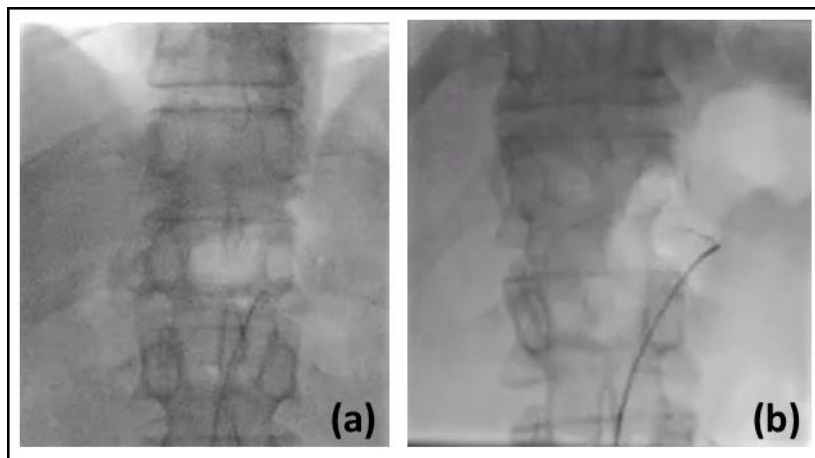


Figure 45 - examples of non-detected catheter tip in RE 01 (a) and RE 02 (b)

The catheter tip displacement curves shown in (*Figure 46*) and (*Figure 47*) illustrate an example of continuous detection in the first sequence RE 01. In (*Figure 46*), we compare the automatically tracked trajectory (blue color) to the manual locations (gold color) in the horizontal (x) direction in the image, whereas in (*Figure 47*) we compare the two trajectories in the vertical (y) direction.

The similarity between the automatic tracking curves and the manual tracking curves indicates the accuracy of the algorithm. YOLO detection method seems to be accurate in detecting the catheter tip in 87% of the sequence frames of RE 01. The mean Euclidean distance calculated over these frames is 0.6 mm with a maximum distance of 2.27 mm and minimum distance of 0 mm.

Results

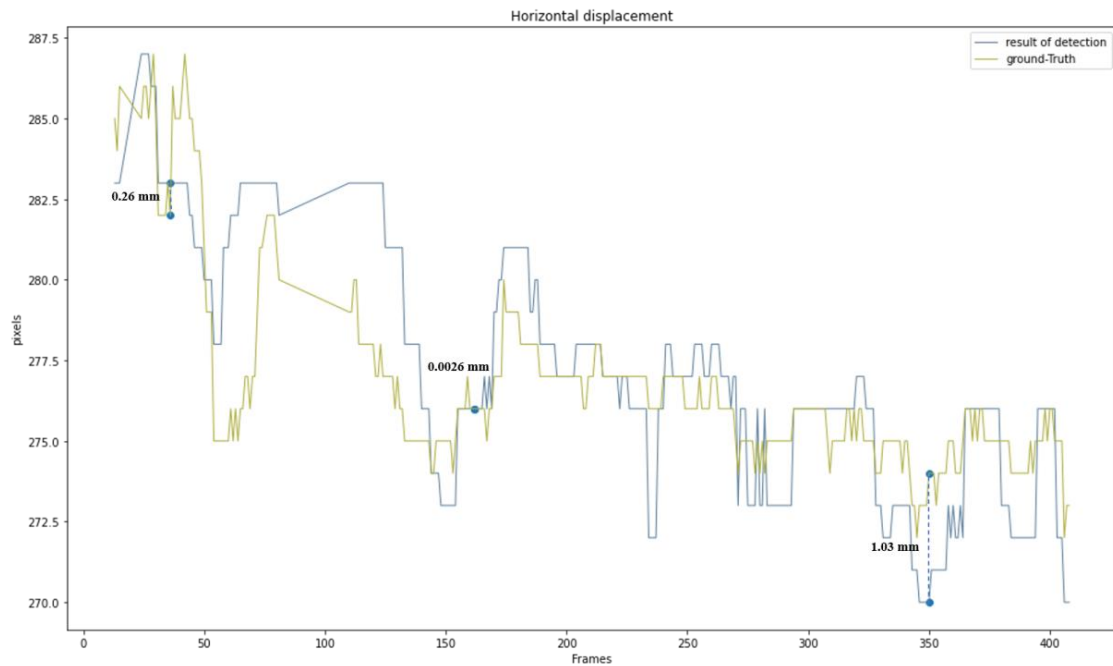


Figure 46 - Horizontal displacement of the catheter tip in sequence RE 01: « Frames » axis presents the frame index in which the catheter tip is detected and “pixels” axis presents the catheter tip horizontal position

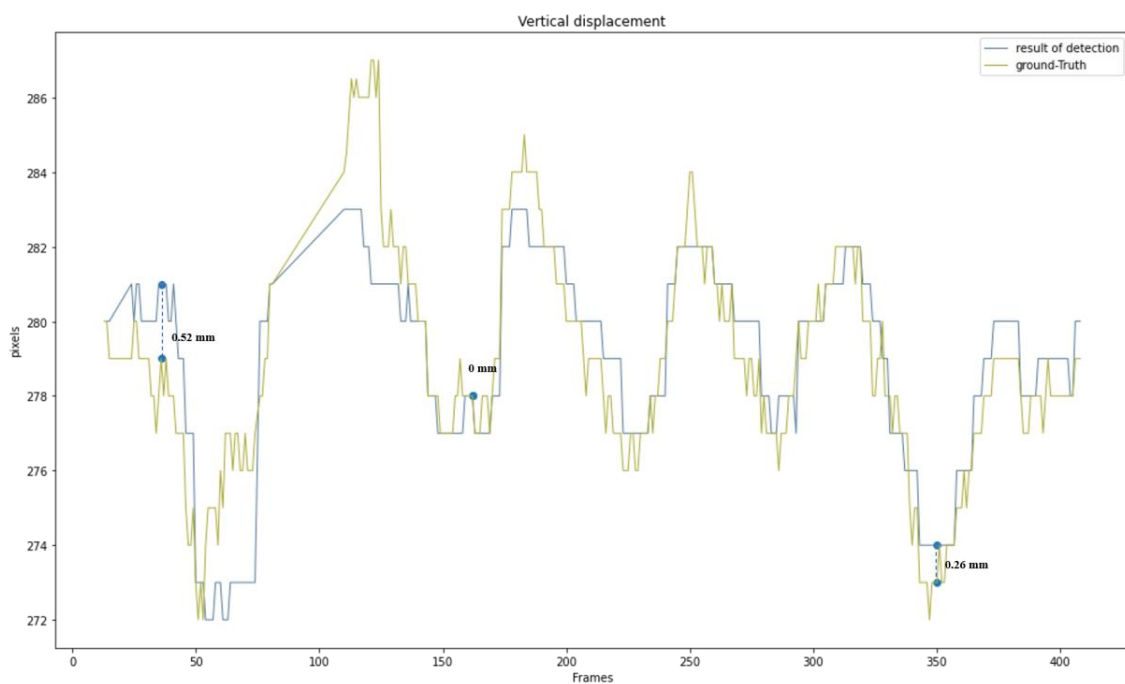


Figure 47 - Vertical displacement of the catheter tip in sequence RE 01: : « Frames » axis presents the frame index in which the catheter tip is detected and “pixels” axis presents the catheter tip vertical position

For catheter tip tracking in sequence RE 02, we obtained a mean Euclidean distance of 0.69 mm with a maximum distance of 1.87 mm and a minimum distance of 0 mm, calculated over the 292 frames of the sequence where the catheter tip has been detected. The detection framework seems to be precise in detecting the catheter tip in the 66% of the sequence frames. This detection precision is suggested by the similarity between the curve of automatically detected positions (blue) and the manually located positions corresponding to ground-truth (gold), in the x and y directions (*Figure 48* and *Figure 49* , respectively).

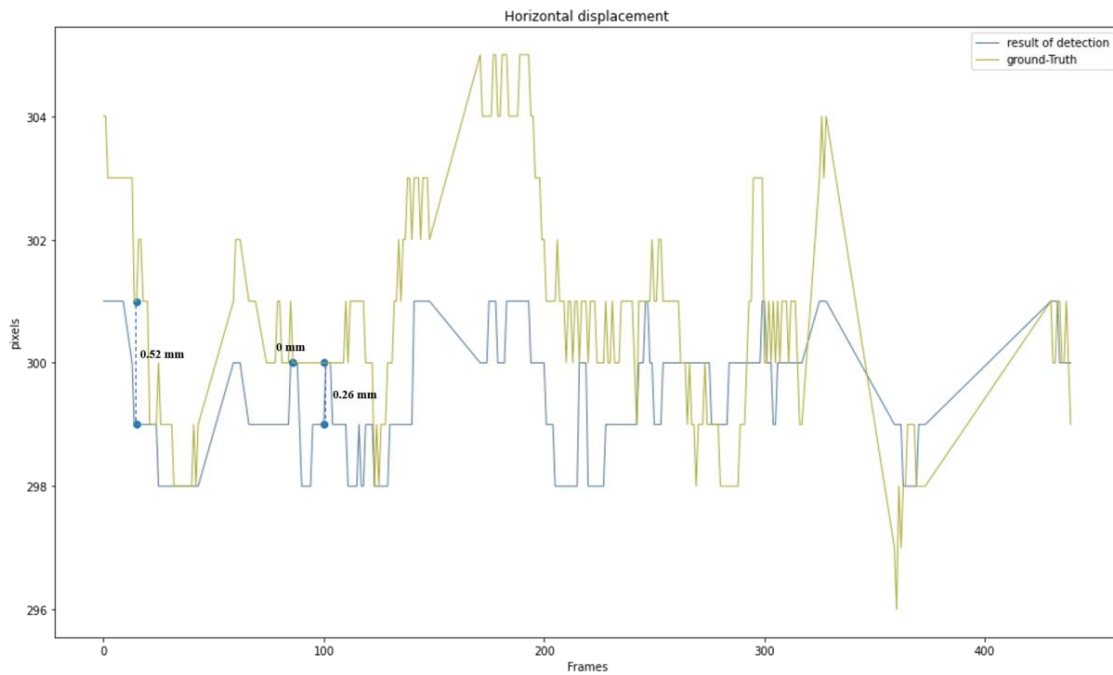


Figure 48 - Horizontal displacement of the catheter tip in sequence RE 02: « Frames » axis presents the frame index in which the catheter tip is detected and “pixels” axis presents the catheter tip horizontal position

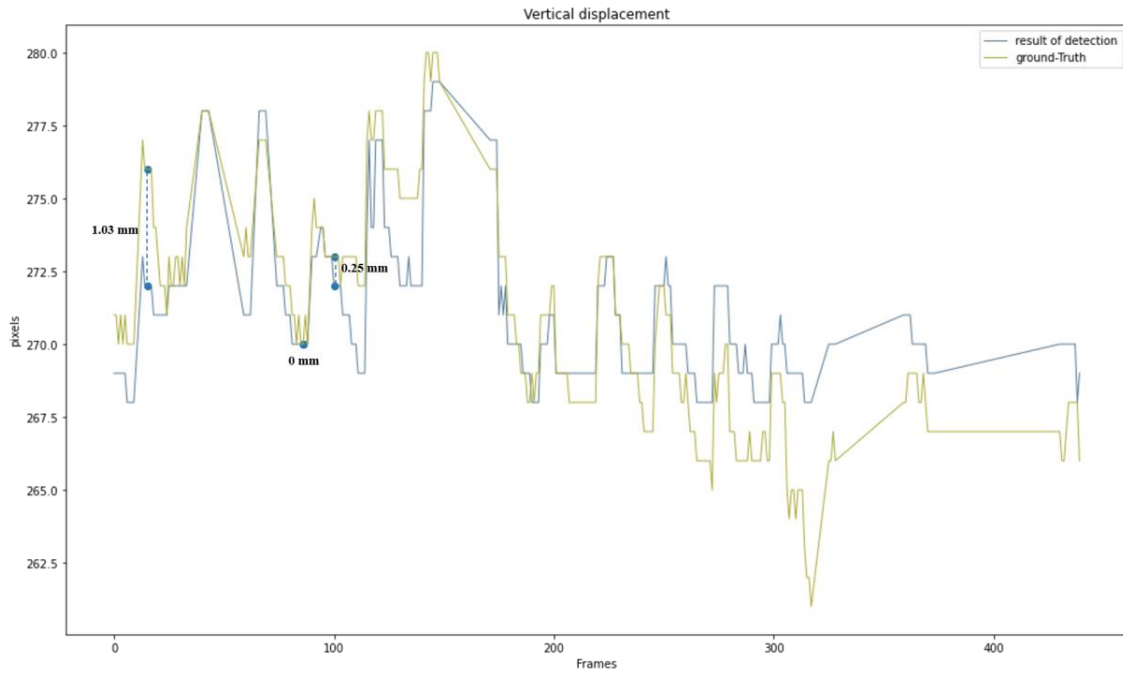


Figure 49 - Vertical displacement of the catheter tip in sequence RE 02: « Frames » axis presents the frame index in which the catheter tip is detected and “pixels” axis presents the catheter tip vertical position

4.4.3 Hepatic arterial repositioning

We have tested repositioning on the same two X-Ray fluoroscopy sequences used for the evaluation of the catheter tip (i.e. RE 01 and RE 02). For the 138 frames of RE 01 where the micro-catheter is introduced in the hepatic arterial tree, 899 inspected points are included in the repositioned vasculature out of 999 points, corresponding to an inclusion rate (IR) of 90% (Figure 50). For the 134 frames of RE 02 where the micro-catheter is introduced in the hepatic arterial tree, 767 points are included in the repositioned vasculature out of 928 points, corresponding to an inclusion rate (IR) of 82% (Figure 51).

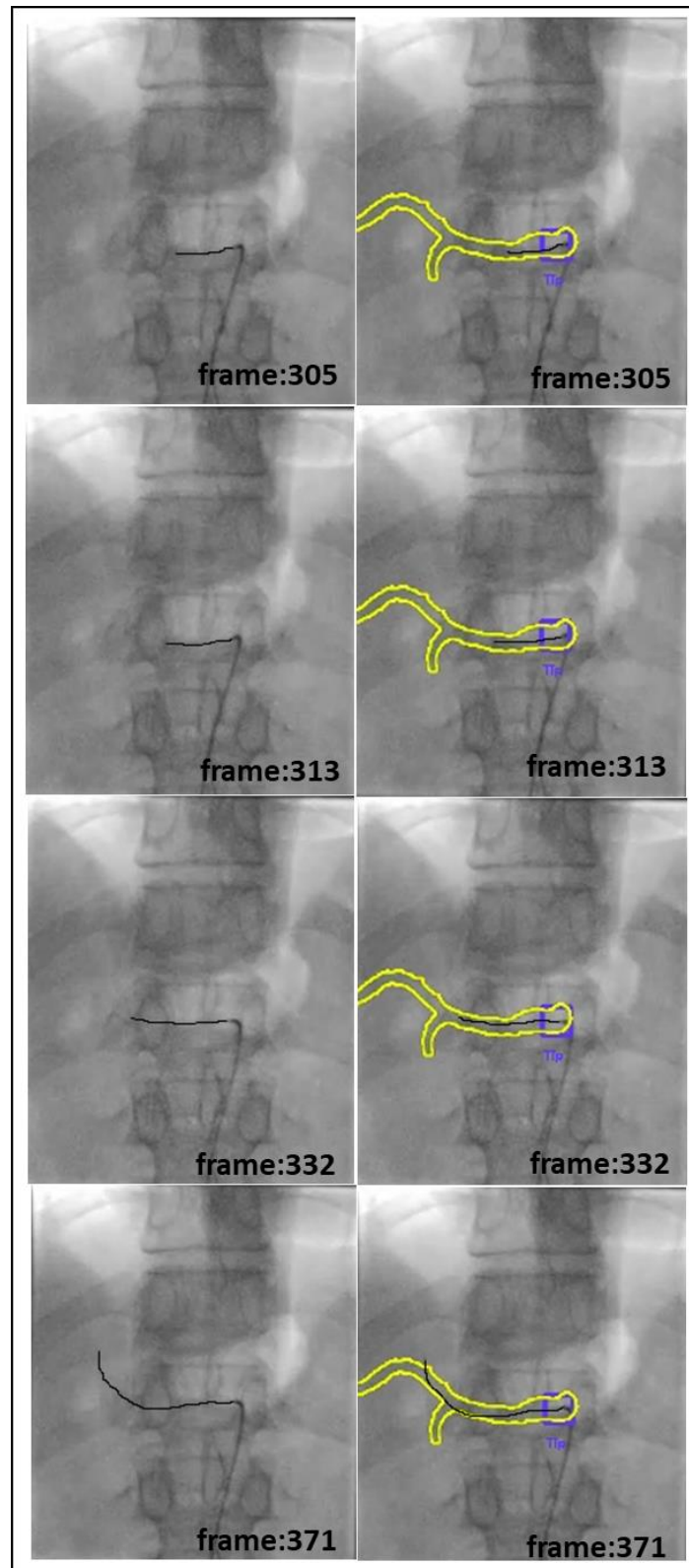


Figure 50 – Hepatic vasculature repositioning result on different frames of sequence RE 01

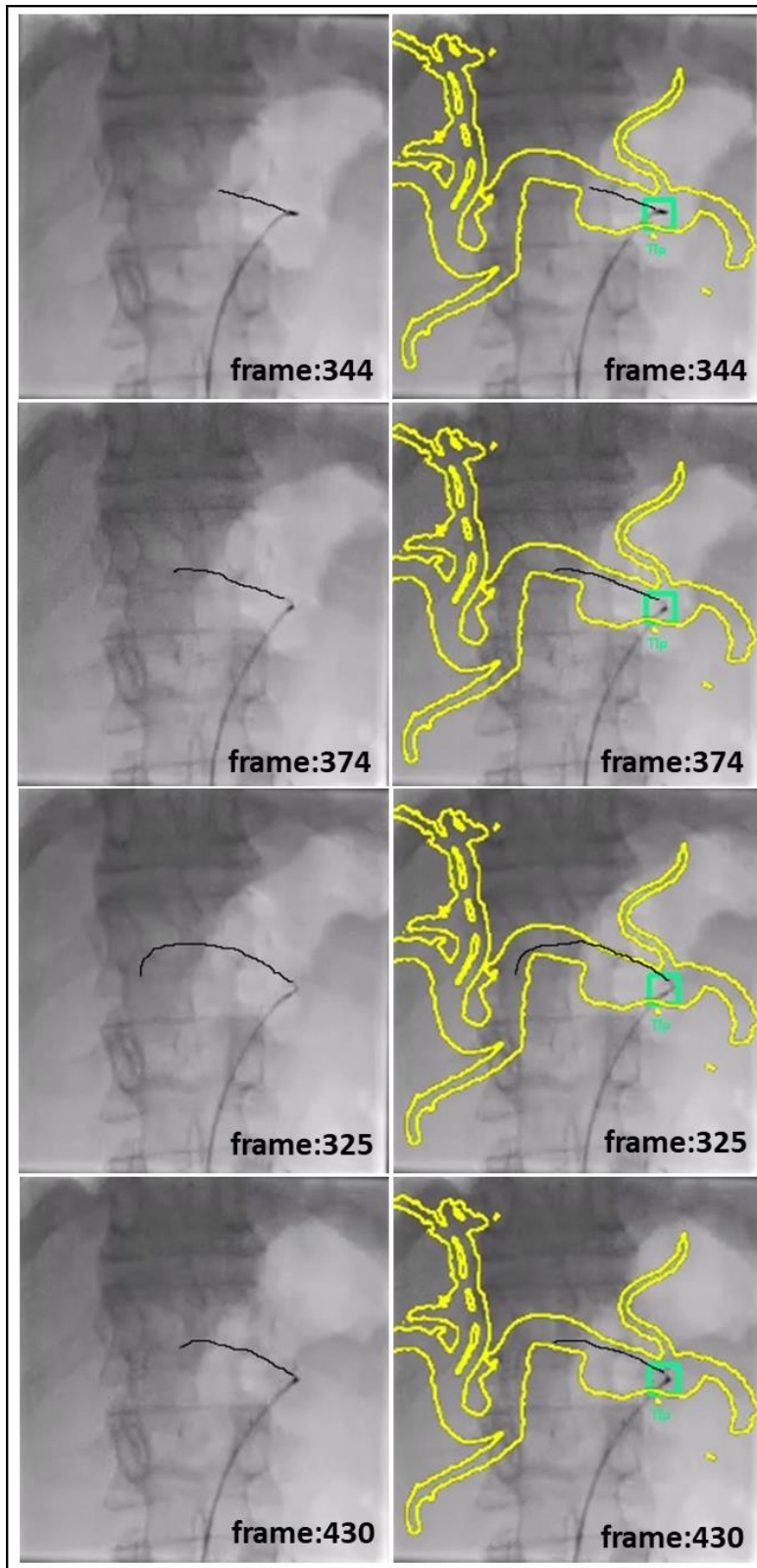


Figure 51 - Hepatic vasculature repositioning result on different frames of sequence RE 02

4.5 Conclusion

In this work, we have proposed an approach to reposition the hepatic arterial tree on 2D X-Ray fluoroscopic sequences in real-time during radioembolization procedures. Our approach allows for the continuous overlay of projected 3D preoperative hepatic structure onto live 2D fluoroscopy despite the respiratory motion. Evaluations of the overall approach were performed on two X-Ray fluoroscopic sequences of liver catheterization during radioembolization procedures, RE 01 and RE 02. The obtained results show that the framework used for the catheter tip detection showed accuracy and robustness on tracking the catheter tip in real time, despite the difficulties related to the lack of discriminating characteristics, low contrast, and low size of the catheter tip. For both cases, the CNN-based method has succeeded in detecting the catheter tip with a detection rate of 87% and 66%, a mean Intersection over Union (IoU) of 0.74 and 0.69, and a mean Euclidean distance of 0.6 mm and 0.69 mm, respectively. The hepatic arterial tree repositioning has also shown efficiency in including the micro-catheter with an IR of 90% and 82% for RE 01 and RE 02, respectively.

Our proposed approach could be applied to integrate the motion related to respiration when augmenting the intraoperative image, and thus provide better micro-catheter localization inside the hepatic vascular structure.

Our proposed approach does not require contrast medium injection / 2D angiographic images nor user interaction.

Conclusion and perspectives

The work presented in this thesis focused on the augmentation of intraoperative 2D X-Ray images during transarterial radioembolization for the treatment of liver cancer. Even if this treatment is already established, the complexity of this type of procedure associated with the limits of interventional imaging, still pose difficulties, in particular for the hepatic arterial tree catheterization.

In the intraoperative phase, regardless the sophistication of imaging devices, notably the C-arm, radiologists used to perform transarterial catheterization with the assistance of two-dimensional X-Ray images. This currently used intraoperative imaging modality provides basic information about the patient's anatomy (*i.e.* bone structure) and inserted interventional tools (*i.e.* catheter and micro-catheter). However the nonpermanent vascular structure visualization is still dependent on contrast medium injection and angiographic images acquisition, resulting in a contrast product whose excessive injection may cause severe reactions for the patient. To our knowledge, no computer-aided image guidance solutions dedicated to the RE interventional guidance and its specific issues have been introduced in the literature so far.

Our goal was to provide a radioembolization assistance solution in order to increase the precision and reliability of the procedure and minimize the contrast medium use and radiation exposure. In particular, our approach provides a more comprehensive feedback of the surgical scene by augmenting intraoperative 2D X-Ray images (*i.e.* fluoroscopic and angiographic images) with preoperative 3D CTA images or pretreatment assessment 2D X-Ray images, medical imaging modalities acquired as part of the clinical routine.

A first line of research focused on proposing a multi-modality image registration strategy for radioembolization pretreatment assessment and treatment sessions. Indeed, we have investigated the performance of a structure-driven intensity-based rigid registration method, which could be used in three main phases of the interventional procedure: 1) celiac trunk access 2) Injection site access and 3) reproducing the injection site during the treatment session.

The three fusion steps were independently evaluated on real clinical data. The approach resulted in qualitatively appropriate anatomical correspondences when projecting the preoperative structures on intraoperative images. With best configurations, the registration steps showed accuracy and feasibility in aligning data, with a limited user interaction and a computation time compatible with the clinical workflow.

Abdominal organs, including the liver, change their positions continuously due to the patient's respiration. Our second line of research dealt with the issue of continuous repositioning of the preoperative hepatic vasculature on the intraoperative fluoroscopy sequence.

We have indeed proposed a CNN based approach to reposition the hepatic arterial tree on 2D X-Ray fluoroscopic sequences in real-time, in order to perform a more fluent and effective catheterization. Our approach allows for the overlay of projected 3D preoperative hepatic structure onto live 2D fluoroscopy despite the respiratory motion. As the hepatic arterial tree displacement can be described by the catheter movement, we propose to update the roadmap position based on the tracking of the 2D catheter tip visualized in intraoperative live 2D X-Ray fluoroscopic sequence. Preliminary results show that the overall approach was robust and could be applied to integrate the respiration induced motion when augmenting the intraoperative image, and thus provide better micro-catheter localization inside the hepatic vascular structure.

The work carried out during this thesis opens up different perspectives for each line of research.

Regarding the 3D/2D registration framework, although results obtained are generally satisfactory, the introduced method presents some limits which might deteriorate the registration process or hamper the catheter manipulation. An initial transformation that is distant from the gold standard increases the failure probability of the registration, resulting in inappropriate anatomical correspondences. A technique using virtual fiducial markers (VFM) could be integrated for the automation of the initial transformation definition [111]. Moreover, although the processing time is compatible with the clinical workflow, it could still be reduced through further algorithmic optimization.

Even though bone-based registration is performed with a relatively low global mean registration error, the projection of the celiac trunk origin can be inaccurate in some cases. We noticed occasionally a slight misalignment between the projected celiac trunk and the inserted catheter observed in the fluoroscopic image. It can be explained by the patient repositioning resulting in a vasculature shift. This resulting projection error has the potential to decrease the precision of the catheter tip localization. A possible solution might consist in estimating an average misalignment range of the celiac trunk origin by calculating, for several patients, the distance between the projected ostium (belonging to the abdominal aorta) and the 2D catheter visualized in the 2D fluoroscopic image. The obtained margin could then be used to better highlight the area of the celiac trunk origin where the catheter should be inserted.

For the vessel-based registration, the approach could be improved by providing an automatic solution for appropriate preoperative data segmentation to remove ambiguities present when an extra vascular segment is included to the HVS volume. For some patients, the HVS is a more likely to be deformed, which might restrict the interest of the proposed strategy for injection site access. For those cases, taking into account this deformation would permit improving the preoperative and intraoperative structures matching.

Regarding the hepatic arterial tree repositioning, our approach relies on the assumption that there is a link between the catheter tip and the hepatic arterial tree. More exhaustive experiments need to be carried out for this purpose to confirm the interest of the catheter tip detection in updating the hepatic arterial tree position.

Published Papers

The following papers have been published as part of this thesis:

1. H. Hammami, F. Lalys, Y. Rolland, A. Petit, and P. Haigron, “Catheter navigation support for liver radioembolization guidance: feasibility of structure-driven intensity-based registration,” *Int. J. Comput. Assist. Radiol. Surg.*, vol. 15, no. 11, pp. 1881–1894, Nov. 2020, doi: 10.1007/s11548-020-02250-8.
2. H. Hammami, F. Lalys, Y. Rolland, P. Haigron, “Feasibility of 2D-3D intensity-based rigid registration for liver radioembolization guidance,” 33rd International Congress on Computer Assisted Radiology and Surgery, Rennes, June 2019. *IJCARS* vol 14.

Bibliography

- [1] G. Gandaglia *et al.*, “Effect of minimally invasive surgery on the risk for surgical site infections: results from the National Surgical Quality Improvement Program (NSQIP) Database,” *JAMA Surg.*, vol. 149, no. 10, pp. 1039–1044, Oct. 2014, doi: 10.1001/jamasurg.2014.292.
- [2] S. R. Z. Abdel-Misih and M. Bloomston, “Liver Anatomy,” *Surg. Clin. North Am.*, vol. 90, no. 4, pp. 643–653, Aug. 2010, doi: 10.1016/j.suc.2010.04.017.
- [3] F. Sutherland and J. Harris, “Claude Couinaud: A Passion for the Liver,” *Arch. Surg.*, vol. 137, no. 11, pp. 1305–1310, Nov. 2002, doi: 10.1001/archsurg.137.11.1305.
- [4] F. C. Brunickardi, D. K. Andersen, T. R. Billiar, D. L. Dunn, and J. G. Hunter, Eds., *Schwartz’s principles of surgery*, Tenth edition. New York: McGraw-Hill Education, 2014.
- [5] “Overview of Blood Vessel Disorders of the Liver - Liver and Gallbladder Disorders,” *Medicine.com*. <https://www.medicine.com/topic/overview-of-blood-vessel-disorders-of-the-liver> (accessed Oct. 18, 2021).
- [6] “Key Statistics About Liver Cancer.” <https://www.cancer.org/cancer/liver-cancer/about/what-is-key-statistics.html> (accessed Mar. 26, 2021).
- [7] W. Stewart B, B. W. Stewart, C. Wild, International Agency for Research on Cancer, and World Health Organization, *World cancer report 2014*. 2014.
- [8] A. K. Singh, R. Kumar, and A. K. Pandey, “Hepatocellular Carcinoma: Causes, Mechanism of Progression and Biomarkers,” *Curr. Chem. Genomics Transl. Med.*, vol. 12, pp. 9–26, Jun. 2018, doi: 10.2174/2213988501812010009.
- [9] E. Dhamija, S. B. Paul, and S. Kedia, “Non-alcoholic fatty liver disease associated with hepatocellular carcinoma: An increasing concern,” *Indian J. Med. Res.*, vol. 149, no. 1, pp. 9–17, Jan. 2019, doi: 10.4103/ijmr.IJMR_1456_17.
- [10] J. M. Llovet, C. Brú, and J. Bruix, “Prognosis of hepatocellular carcinoma: the BCLC staging classification,” *Semin. Liver Dis.*, vol. 19, no. 3, pp. 329–338, 1999, doi: 10.1055/s-2007-1007122.

- [11] S. B. Edge and C. C. Compton, “The American Joint Committee on Cancer: the 7th edition of the AJCC cancer staging manual and the future of TNM,” *Ann. Surg. Oncol.*, vol. 17, no. 6, pp. 1471–1474, Jun. 2010, doi: 10.1245/s10434-010-0985-4.
- [12] K. Okuda, H. Obata, Y. Nakajima, T. Ohtsuki, N. Okazaki, and K. Ohnishi, “Prognosis of primary hepatocellular carcinoma,” *Hepatol. Baltim. Md*, vol. 4, no. 1 Suppl, pp. 3S-6S, Feb. 1984, doi: 10.1002/hep.1840040703.
- [13] “A new prognostic system for hepatocellular carcinoma: a retrospective study of 435 patients: the Cancer of the Liver Italian Program (CLIP) investigators,” *Hepatol. Baltim. Md*, vol. 28, no. 3, pp. 751–755, Sep. 1998, doi: 10.1002/hep.510280322.
- [14] S. McDermott and D. A. Gervais, “Radiofrequency Ablation of Liver Tumors,” *Semin. Interv. Radiol.*, vol. 30, no. 1, pp. 49–55, Mar. 2013, doi: 10.1055/s-0033-1333653.
- [15] C. Zavaglia, A. Mancuso, A. Foschi, and A. Rampoldi, “High-intensity focused ultrasound (HIFU) for the treatment of hepatocellular carcinoma: is it time to abandon standard ablative percutaneous treatments?,” *Hepatobiliary Surg. Nutr.*, vol. 2, no. 4, pp. 184–187, Aug. 2013, doi: 10.3978/j.issn.2304-3881.2013.05.02.
- [16] “Radiotherapy for liver cancer.” <https://www.ncbi.nlm.nih.gov/pmc/articles/PMC5689403/> (accessed May 06, 2021).
- [17] “Chemotherapy studies in primary liver cancer. A prospective randomized clinical trial - Falksom - 1978 - Cancer - Wiley Online Library.” [https://acsjournals.onlinelibrary.wiley.com/doi/abs/10.1002/1097-0142\(197811\)42:5%3C2149::AID-CNCR2820420510%3E3.0.CO;2-5](https://acsjournals.onlinelibrary.wiley.com/doi/abs/10.1002/1097-0142(197811)42:5%3C2149::AID-CNCR2820420510%3E3.0.CO;2-5) (accessed May 06, 2021).
- [18] R. Lencioni, P. Petruzzi, and L. Crocetti, “Chemoembolization of Hepatocellular Carcinoma,” *Semin. Interv. Radiol.*, vol. 30, no. 1, pp. 3–11, Mar. 2013, doi: 10.1055/s-0033-1333648.

- [19] B. Sangro, M. Iñarrairaegui, and J. I. Bilbao, “Radioembolization for hepatocellular carcinoma,” *J. Hepatol.*, vol. 56, no. 2, pp. 464–473, Feb. 2012, doi: 10.1016/j.jhep.2011.07.012.
- [20] T. F. Greten and B. Sangro, “Targets for immunotherapy of liver cancer,” *J. Hepatol.*, vol. 68, no. 1, pp. 157–166, Jan. 2018, doi: 10.1016/j.jhep.2017.09.007.
- [21] H. R. Bierman, R. L. Byron, K. H. Kelley, and A. Grady, “Studies on the blood supply of tumors in man. III. Vascular patterns of the liver by hepatic arteriography in vivo,” *J. Natl. Cancer Inst.*, vol. 12, no. 1, pp. 107–131, Aug. 1951.
- [22] C. Breedis and G. Young, “The Blood Supply of Neoplasms in the Liver,” *Am. J. Pathol.*, vol. 30, no. 5, pp. 969–985, Oct. 1954.
- [23] J. Balogh *et al.*, “Hepatocellular carcinoma: a review,” *J. Hepatocell. Carcinoma*, vol. 3, pp. 41–53, Oct. 2016, doi: 10.2147/JHC.S61146.
- [24] B. Sangro *et al.*, “Survival after yttrium-90 resin microsphere radioembolization of hepatocellular carcinoma across Barcelona clinic liver cancer stages: a European evaluation,” *Hepatol. Baltim. Md*, vol. 54, no. 3, pp. 868–878, Sep. 2011, doi: 10.1002/hep.24451.
- [25] J. F. Prince *et al.*, “Efficacy of Radioembolization with ¹⁶⁶Ho-Microspheres in Salvage Patients with Liver Metastases: A Phase 2 Study,” *J. Nucl. Med. Off. Publ. Soc. Nucl. Med.*, vol. 59, no. 4, pp. 582–588, Apr. 2018, doi: 10.2967/jnumed.117.197194.
- [26] P. C.-H. Kwok *et al.*, “Survival benefit of radioembolization for inoperable hepatocellular carcinoma using yttrium-90 microspheres,” *J. Gastroenterol. Hepatol.*, vol. 29, no. 11, pp. 1897–1904, Nov. 2014, doi: 10.1111/jgh.12621.
- [27] S. Puppala, “Technical update on transcatheter arterial chemoembolization,” 2019, doi: 10.20517/2394-5079.2019.28.
- [28] E. Garin *et al.*, “Personalized dosimetry and intensification concept with ⁹⁰Y-loaded glass microsphere radioembolization induce prolonged overall survival in hepatocellular

carcinoma patients with portal vein thrombosis,” *J. Nucl. Med.*, p. jnumed.114.145177, Feb. 2015, doi: 10.2967/jnumed.114.145177.

[29] P. Ambrosini, D. Ruijters, W. J. Niessen, A. Moelker, and T. van Walsum, “Continuous roadmapping in liver TACE procedures using 2D–3D catheter-based registration,” *Int. J. Comput. Assist. Radiol. Surg.*, vol. 10, no. 9, pp. 1357–1370, Sep. 2015, doi: 10.1007/s11548-015-1218-x.

[30] E. Jafargholi Rangraz, W. Coudyzer, G. Maleux, K. Baete, C. M. Deroose, and J. Nuyts, “Multi-modal image analysis for semi-automatic segmentation of the total liver and liver arterial perfusion territories for radioembolization,” *EJNMMI Res.*, vol. 9, no. 1, p. 19, Feb. 2019, doi: 10.1186/s13550-019-0485-x.

[31] N. Spahr, S. Thoduka, N. Abolmaali, R. Kikinis, and A. Schenk, “Multimodal image registration for liver radioembolization planning and patient assessment,” *Int. J. Comput. Assist. Radiol. Surg.*, vol. 14, no. 2, pp. 215–225, Feb. 2019, doi: 10.1007/s11548-018-1877-5.

[32] “Key Considerations for Your Interventional Radiology Suite,” *Digirad*, Oct. 02, 2020. <https://www.digirad.com/must-haves-for-the-interventional-radiology-suite/> (accessed Oct. 18, 2021).

[33] E. Garin, Y. Rolland, S. Laffont, and J. Edeline, “Clinical impact of ^{99m}Tc -MAA SPECT/CT-based dosimetry in the radioembolization of liver malignancies with ^{90}Y -loaded microspheres,” *Eur. J. Nucl. Med. Mol. Imaging*, vol. 43, pp. 559–575, 2016, doi: 10.1007/s00259-015-3157-8.

[34] M. Kafrouni *et al.*, “Analysis of differences between ^{99m}Tc -MAA SPECT- and ^{90}Y -microsphere PET-based dosimetry for hepatocellular carcinoma selective internal radiation therapy,” *EJNMMI Res.*, vol. 9, no. 1, p. 62, Jul. 2019, doi: 10.1186/s13550-019-0533-6.

[35] E. Garin *et al.*, “Dosimetry based on ^{99m}Tc -macroaggregated albumin SPECT/CT accurately predicts tumor response and survival in hepatocellular carcinoma patients treated with ^{90}Y -loaded glass microspheres: preliminary results,” *J. Nucl. Med. Off. Publ. Soc. Nucl. Med.*, vol. 53, no. 2, pp. 255–263, Feb. 2012, doi: 10.2967/jnumed.111.094235.

- [36] V. Morán *et al.*, “Impact of the dosimetry approach on the resulting 90Y radioembolization planned absorbed doses based on 99mTc-MAA SPECT-CT: is there agreement between dosimetry methods?,” *EJNMMI Phys.*, vol. 7, no. 1, p. 72, Dec. 2020, doi: 10.1186/s40658-020-00343-6.
- [37] A. A. Alsultan, M. L. J. Smits, M. W. Barentsz, A. J. A. T. Braat, and M. G. E. H. Lam, “The value of yttrium-90 PET/CT after hepatic radioembolization: a pictorial essay,” *Clin. Transl. Imaging*, vol. 7, no. 4, pp. 303–312, Aug. 2019, doi: 10.1007/s40336-019-00335-2.
- [38] D. Ruijters, R. Homan, P. Mielekamp, P. van de Haar, and D. Babic, “Validation of 3D multimodality roadmapping in interventional neuroradiology,” *Phys. Med. Biol.*, vol. 56, no. 16, pp. 5335–5354, Aug. 2011, doi: 10.1088/0031-9155/56/16/017.
- [39] A. Krishnaswamy, E. M. Tuzcu, and S. R. Kapadia, “Integration of MDCT and fluoroscopy using C-arm computed tomography to guide structural cardiac interventions in the cardiac catheterization laboratory,” *Catheter. Cardiovasc. Interv. Off. J. Soc. Card. Angiogr. Interv.*, vol. 85, no. 1, pp. 139–147, Jan. 2015, doi: 10.1002/ccd.25392.
- [40] J. J. Thaden *et al.*, “Echocardiographic and Fluoroscopic Fusion Imaging for Procedural Guidance: An Overview and Early Clinical Experience,” *J. Am. Soc. Echocardiogr.*, vol. 29, no. 6, pp. 503–512, Jun. 2016, doi: 10.1016/j.echo.2016.01.013.
- [41] J. B. A. Maintz and M. A. Viergever, “A survey of medical image registration,” *Med. Image Anal.*, vol. 2, no. 1, pp. 1–36, Mar. 1998, doi: 10.1016/S1361-8415(01)80026-8.
- [42] F. P. M. Oliveira and J. M. R. S. Tavares, “Medical image registration: a review,” *Comput. Methods Biomech. Biomed. Engin.*, vol. 17, no. 2, pp. 73–93, 2014, doi: 10.1080/10255842.2012.670855.
- [43] A. Sotiras, C. Davatzikos, and N. Paragios, “Deformable Medical Image Registration: A Survey,” *IEEE Trans. Med. Imaging*, vol. 32, no. 7, pp. 1153–1190, Jul. 2013, doi: 10.1109/TMI.2013.2265603.

- [44] M. A. Viergever, J. B. A. Maintz, S. Klein, K. Murphy, M. Staring, and J. P. W. Pluim, "A survey of medical image registration - under review," *Med. Image Anal.*, vol. 33, pp. 140–144, Oct. 2016, doi: 10.1016/j.media.2016.06.030.
- [45] F. Lalys *et al.*, "A hybrid image fusion system for endovascular interventions of peripheral artery disease," *Int. J. Comput. Assist. Radiol. Surg.*, vol. 13, no. 7, pp. 997–1007, Jul. 2018, doi: 10.1007/s11548-018-1731-9.
- [46] A. Duménil, A. Kaladji, M. Castro, C. Göksu, A. Lucas, and P. Haigron, "A versatile intensity-based 3D/2D rigid registration compatible with mobile C-arm for endovascular treatment of abdominal aortic aneurysm," *Int. J. Comput. Assist. Radiol. Surg.*, vol. 11, no. 9, pp. 1713–1729, Sep. 2016, doi: 10.1007/s11548-016-1416-1.
- [47] M. A. Clifford, F. Banovac, E. Levy, and K. Cleary, "Assessment of hepatic motion secondary to respiration for computer assisted interventions," *Comput. Aided Surg. Off. J. Int. Soc. Comput. Aided Surg.*, vol. 7, no. 5, pp. 291–299, 2002, doi: 10.1002/igs.10049.
- [48] V. Venkatraman, M. H. Van Horn, S. Weeks, and E. Bullitt, "Liver Motion Due to Needle Pressure, Cardiac, and Respiratory Motion During the TIPS Procedure," in *Medical Image Computing and Computer-Assisted Intervention – MICCAI 2004*, Berlin, Heidelberg, 2004, pp. 66–72. doi: 10.1007/978-3-540-30136-3_9.
- [49] J. M. Blackall, A. P. King, G. P. Penney, A. Adam, and D. J. Hawkes, "A Statistical Model of Respiratory Motion and Deformation of the Liver," in *Medical Image Computing and Computer-Assisted Intervention – MICCAI 2001*, Berlin, Heidelberg, 2001, pp. 1338–1340. doi: 10.1007/3-540-45468-3_219.
- [50] T. Rohlfing, C. R. Maurer, W. G. O'Dell, and J. Zhong, "Modeling liver motion and deformation during the respiratory cycle using intensity-based nonrigid registration of gated MR images," *Med. Phys.*, vol. 31, no. 3, pp. 427–432, Mar. 2004, doi: 10.1118/1.1644513.
- [51] P. Ambrosini, I. Smal, D. Ruijters, W. J. Niessen, A. Moelker, and T. Van Walsum, "A Hidden Markov Model for 3D Catheter Tip Tracking With 2D X-ray Catheterization Sequence and 3D Rotational Angiography," *IEEE Trans. Med. Imaging*, vol. 36, no. 3, pp. 757–768, 2017, doi: 10.1109/TMI.2016.2625811.

- [52] I. Bargellini *et al.*, “Image fusion of preprocedural CTA with real-time fluoroscopy to guide proper hepatic artery catheterization during transarterial chemoembolization of hepatocellular carcinoma: a feasibility study,” *Cardiovasc. Intervent. Radiol.*, vol. 36, no. 2, pp. 526–530, Apr. 2013, doi: 10.1007/s00270-012-0495-9.
- [53] J. Garcia Guevara, I. Peterlik, M.-O. Berger, and S. Cotin, “Biomechanics-based graph matching for augmented CT-CBCT,” *Int. J. Comput. Assist. Radiol. Surg.*, vol. 13, no. 6, pp. 805–813, Jun. 2018, doi: 10.1007/s11548-018-1755-1.
- [54] A. M. Sailer, M. W. de Haan, A. G. Peppelenbosch, M. J. Jacobs, J. E. Wildberger, and G. W. H. Schurink, “CTA with fluoroscopy image fusion guidance in endovascular complex aortic aneurysm repair,” *Eur. J. Vasc. Endovasc. Surg. Off. J. Eur. Soc. Vasc. Surg.*, vol. 47, no. 4, pp. 349–356, Apr. 2014, doi: 10.1016/j.ejvs.2013.12.022.
- [55] D. Ruijters, B. M. ter Haar Romeny, and P. Suetens, “Vesselness-based 2D–3D registration of the coronary arteries,” *Int. J. Comput. Assist. Radiol. Surg.*, vol. 4, no. 4, pp. 391–397, Jun. 2009, doi: 10.1007/s11548-009-0316-z.
- [56] S. Gorges, E. Kerrien, and M.-O. Berger, “3D Augmented Fluoroscopy in Interventional Neuroradiology: Precision Assessment and First Evaluation on Clinical Cases,” p. 10.
- [57] I. Bargellini *et al.*, “Image Fusion of Preprocedural CTA with Real-time Fluoroscopy to Guide Proper Hepatic Artery Catheterization During Transarterial Chemoembolization of Hepatocellular Carcinoma: A Feasibility Study,” *Cardiovasc. Intervent. Radiol.*, vol. 36, Oct. 2012, doi: 10.1007/s00270-012-0495-9.
- [58] W. Ahmad, H.-C. Hasselmann, N. Galas, P. Majd, S. Brunkwall, and J. S. Brunkwall, “Image fusion using the two-dimensional-three-dimensional registration method helps reduce contrast medium volume, fluoroscopy time, and procedure time in hybrid thoracic endovascular aortic repairs,” *J. Vasc. Surg.*, vol. 69, no. 4, pp. 1003–1010, Apr. 2019, doi: 10.1016/j.jvs.2018.07.043.
- [59] P. Markelj, D. Tomaževič, B. Likar, and F. Pernuš, “A review of 3D/2D registration methods for image-guided interventions,” *Med. Image Anal.*, vol. 16, no. 3, pp. 642–661, Apr. 2012, doi: 10.1016/j.media.2010.03.005.

- [60] R. Liao, P. Li, Y. Sun, and S. Miao, "A Review of Recent Advances in Registration Techniques Applied to Minimally Invasive Therapy," *Multimed. IEEE Trans. On*, vol. 15, pp. 983–1000, Aug. 2013, doi: 10.1109/TMM.2013.2244869.
- [61] S. Matl, R. Brosig, M. Baust, N. Navab, and S. Demirci, "Vascular image registration techniques: A living review," *Med. Image Anal.*, vol. 35, pp. 1–17, Jan. 2017, doi: 10.1016/j.media.2016.05.005.
- [62] S. Atasoy *et al.*, "Real-time respiratory motion tracking: roadmap correction for hepatic artery catheterizations," in *Medical Imaging 2008: Visualization, Image-Guided Procedures, and Modeling*, Mar. 2008, vol. 6918, p. 691815. doi: 10.1117/12.760985.
- [63] S. A. Pawiro *et al.*, "Validation for 2D/3D registration. I: A new gold standard data set," *Med. Phys.*, vol. 38, no. 3, pp. 1481–1490, Mar. 2011, doi: 10.1118/1.3553402.
- [64] Y. Ma *et al.*, "Clinical evaluation of respiratory motion compensation for anatomical roadmap guided cardiac electrophysiology procedures," *IEEE Trans. Biomed. Eng.*, vol. 59, no. 1, pp. 122–131, Jan. 2012, doi: 10.1109/TBME.2011.2168393.
- [65] M. Groher, F. Bender, R.-T. Hoffmann, and N. Navab, "Segmentation-driven 2D-3D registration for abdominal catheter interventions," *Med. Image Comput. Comput.-Assist. Interv. MICCAI Int. Conf. Med. Image Comput. Comput.-Assist. Interv.*, vol. 10, no. Pt 2, pp. 527–535, 2007, doi: 10.1007/978-3-540-75759-7_64.
- [66] D. Rivest-Hénault, H. Sundar, and M. Cherié, "Nonrigid 2D/3D registration of coronary artery models with live fluoroscopy for guidance of cardiac interventions," *IEEE Trans. Med. Imaging*, vol. 31, no. 8, pp. 1557–1572, Aug. 2012, doi: 10.1109/TMI.2012.2195009.
- [67] H. Sundar, A. Kamen, C. Xu, F. Sauer, and C. Davatzikos, "A novel 2D-3D registration algorithm for aligning fluoro images with 3D pre-op CT/MR images," *Proc SPIE*, vol. 6141, pp. 760–766, Mar. 2006, doi: 10.1117/12.654251.
- [68] J. Hipwell *et al.*, "Intensity-based 2-D - 3-D registration of cerebral angiograms," *IEEE Trans. Med. Imaging*, vol. 22, pp. 1417–26, Dec. 2003, doi: 10.1109/TMI.2003.819283.

- [69] U. Mitrović, F. Pernuš, B. Likar, and Ž. Špiclin, “Simultaneous 3D-2D image registration and C-arm calibration: Application to endovascular image-guided interventions,” *Med. Phys.*, vol. 42, no. 11, pp. 6433–6447, Nov. 2015, doi: 10.1118/1.4932626.
- [70] G. P. Penney, J. Weese, J. A. Little, P. Desmedt, D. L. G. Hill, and D. J. Hawkes, “A comparison of similarity measures for use in 2D-3D medical image registration,” in *Medical Image Computing and Computer-Assisted Intervention — MICCAI’98*, Berlin, Heidelberg, 1998, pp. 1153–1161. doi: 10.1007/BFb0056305.
- [71] I. V. D. Bom, S. Klein, M. Staring, R. Homan, L. Bartels, and J. Pluim, “Evaluation of optimization methods for intensity-based 2D-3D registration in x-ray guided interventions,” *undefined*, 2011, Accessed: May 17, 2021. [Online]. Available: /paper/Evaluation-of-optimization-methods-for-2D-3D-in-Bom-Klein/afdaafca20f2e158078f0b0253047c04b7d28b4d
- [72] A. Kubias, F. Deinzer, T. Feldmann, and D. Paulus, “Extended Global Optimization Strategy for Rigid 2D/3D Image Registration,” in *Computer Analysis of Images and Patterns*, Berlin, Heidelberg, 2007, pp. 759–767. doi: 10.1007/978-3-540-74272-2_94.
- [73] J. P. W. Pluim, S. E. A. Muenzing, K. A. J. Eppenhof, and K. Murphy, “The truth is hard to make: Validation of medical image registration,” in *2016 23rd International Conference on Pattern Recognition (ICPR)*, Cancun, Dec. 2016, pp. 2294–2300. doi: 10.1109/ICPR.2016.7899978.
- [74] J. M. Fitzpatrick, D. L. Hill, Y. Shyr, J. West, C. Studholme, and C. R. Maurer, “Visual assessment of the accuracy of retrospective registration of MR and CT images of the brain,” *IEEE Trans. Med. Imaging*, vol. 17, no. 4, pp. 571–585, Aug. 1998, doi: 10.1109/42.730402.
- [75] E. R. Denton *et al.*, “Comparison and evaluation of rigid, affine, and nonrigid registration of breast MR images,” *J. Comput. Assist. Tomogr.*, vol. 23, no. 5, pp. 800–805, Oct. 1999, doi: 10.1097/00004728-199909000-00031.
- [76] A. Roche, X. Pennec, G. Malandain, and N. Ayache, “Rigid registration of 3-D ultrasound with MR images: a new approach combining intensity and gradient information,”

IEEE Trans. Med. Imaging, vol. 20, no. 10, pp. 1038–1049, Oct. 2001, doi: 10.1109/42.959301.

[77] K. Rohr, M. Fornefett, and H. S. Stiehl, “Spline-based elastic image registration: integration of landmark errors and orientation attributes,” *Comput. Vis. Image Underst.*, vol. 90, no. 2, pp. 153–168, May 2003, doi: 10.1016/S1077-3142(03)00048-1.

[78] J. H. Song, “Methods for evaluating image registration,” Doctor of Philosophy, University of Iowa, 2017. doi: 10.17077/etd.v0vailob.

[79] A. Kaladji, A. Lucas, G. Kervio, P. Haigron, and A. Cardon, “Sizing for endovascular aneurysm repair: clinical evaluation of a new automated three-dimensional software,” *Ann. Vasc. Surg.*, vol. 24, no. 7, pp. 912–920, Oct. 2010, doi: 10.1016/j.avsg.2010.03.018.

[80] Kyeheun Kim, Sungjin Park, Helen Hong, and Yeong Gil Shin, “Fast 2D-3D registration using GPU-based preprocessing,” in *Proceedings of 7th International Workshop on Enterprise networking and Computing in Healthcare Industry, 2005. HEALTHCOM 2005.*, Jun. 2005, pp. 139–143. doi: 10.1109/HEALTH.2005.1500424.

[81] A. M. Sailer *et al.*, “Quantification of Respiratory Movement of the Aorta and Side Branches,” *J. Endovasc. Ther. Off. J. Int. Soc. Endovasc. Spec.*, vol. 22, no. 6, pp. 905–911, Dec. 2015, doi: 10.1177/1526602815605325.

[82] A. H. Raheem, T. Carrell, B. Modarai, and G. P. Penney, “Non-rigid 2 D-3 D image registration for use in Endovascular repair of Abdominal Aortic Aneurysms,” 2010. /paper/Non-rigid-2-D-3-D-image-registration-for-use-in-of-Raheem-Carrell/fe0b70f585bb74375b6813a8223d9e4c4a4bde07 (accessed Aug. 02, 2020).

[83] E. Wehrenberg-Klee, R. T. Gandhi, and S. Ganguli, “Patient Selection and Clinical Outcomes of Y90 in Hepatocellular Carcinoma,” *Tech. Vasc. Interv. Radiol.*, vol. 22, no. 2, pp. 70–73, Jun. 2019, doi: 10.1053/j.tvir.2019.02.006.

[84] E. Muñoz Corral, “Efficient Model-based 3D Tracking by Using Direct Image Registration,” phd, Facultad de Informática (UPM), 2012. Accessed: Jul. 18, 2021. [Online]. Available: <http://oa.upm.es/11113/>

-
- [85] B. Delabarre, “Contributions to dense visual tracking and visual servoing using robust similarity criteria,” phdthesis, Université Rennes 1, 2014. Accessed: Jul. 18, 2021. [Online]. Available: <https://tel.archives-ouvertes.fr/tel-01101642>
- [86] A. Dame, “A unified direct approach for visual servoing and visual tracking using mutual information,” phdthesis, Université Rennes 1, 2010. Accessed: Jul. 18, 2021. [Online]. Available: <https://tel.archives-ouvertes.fr/tel-00558196>
- [87] C. Harris and M. Stephens, “A Combined Corner and Edge Detector,” in *Proceedings of the Alvey Vision Conference 1988*, Manchester, 1988, p. 23.1-23.6. doi: 10.5244/C.2.23.
- [88] E. Marchand, “VISP: a software environment for eye-in-hand visual servoing,” in *Proceedings 1999 IEEE International Conference on Robotics and Automation (Cat. No.99CH36288C)*, Detroit, MI, USA, 1999, vol. 4, pp. 3224–3229. doi: 10.1109/ROBOT.1999.774089.
- [89] G. D. Hager and K. Toyama, “X Vision: A Portable Substrate for Real-Time Vision Applications,” *Comput. Vis. Image Underst.*, vol. 69, no. 1, pp. 23–37, Jan. 1998, doi: 10.1006/cviu.1997.0586.
- [90] S. Boukir, P. Bouthemy, F. Chaumette, and D. Juvin, “A local method for contour matching and its parallel implementation,” *Mach. Vis. Appl.*, vol. 10, no. 5, pp. 321–330, Apr. 1998, doi: 10.1007/s001380050082.
- [91] M. Vincze, “Robust tracking of ellipses at frame rate,” *Pattern Recognit.*, vol. 34, no. 2, pp. 487–498, Feb. 2001, doi: 10.1016/S0031-3203(99)00230-7.
- [92] M.-O. Berger, “How to track efficiently piecewise curved contours with a view to reconstructing 3D objects,” in *Proceedings of 12th International Conference on Pattern Recognition*, Oct. 1994, vol. 1, pp. 32–36 vol.1. doi: 10.1109/ICPR.1994.576221.
- [93] C. Martinez, P. Campoy, I. Mondragón, J. Sanchez-Lopez, and M. Olivares-Mendez, “HMPMR strategy for real-time tracking in aerial images, using direct methods,” *Mach. Vis. Appl.*, vol. 25, pp. 1283–1308, Jul. 2014, doi: 10.1007/s00138-014-0617-2.

- [94] J. Yang *et al.*, “Is Diaphragm Motion a Good Surrogate for Liver Tumor Motion?,” *Int. J. Radiat. Oncol. Biol. Phys.*, vol. 90, no. 4, pp. 952–958, Nov. 2014, doi: 10.1016/j.ijrobp.2014.07.028.
- [95] S. C. Davies, A. L. Hill, R. B. Holmes, M. Halliwell, and P. C. Jackson, “Ultrasound quantitation of respiratory organ motion in the upper abdomen,” *Br. J. Radiol.*, vol. 67, no. 803, pp. 1096–1102, Nov. 1994, doi: 10.1259/0007-1285-67-803-1096.
- [96] H. Ma, I. Smal, J. Daemen, and T. van Walsum, “Dynamic coronary roadmapping via catheter tip tracking in X-ray fluoroscopy with deep learning based Bayesian filtering,” *Med. Image Anal.*, vol. 61, p. 101634, Apr. 2020, doi: 10.1016/j.media.2020.101634.
- [97] H. W. Korin, R. L. Ehman, S. J. Riederer, J. P. Felmlee, and R. C. Grimm, “Respiratory kinematics of the upper abdominal organs: a quantitative study,” *Magn. Reson. Med.*, vol. 23, no. 1, pp. 172–178, Jan. 1992, doi: 10.1002/mrm.1910230118.
- [98] W. J. C. Koppert, M. M. A. Dietze, S. van der Velden, J. H. L. Steenbergen, and H. W. A. M. de Jong, “A comparative study of NaI(Tl), CeBr₃, and CZT for use in a real-time simultaneous nuclear and fluoroscopic dual-layer detector,” *Phys. Med. Biol.*, vol. 64, no. 13, p. 135012, Jul. 2019, doi: 10.1088/1361-6560/ab267c.
- [99] S. Speidel, M. Delles, C. Gutt, and R. Dillmann, “Tracking of Instruments in Minimally Invasive Surgery for Surgical Skill Analysis,” Aug. 2006, vol. 4091, pp. 148–155. doi: 10.1007/11812715_19.
- [100] S. Speidel *et al.*, “Visual tracking of da Vinci instruments for laparoscopic surgery,” in *Medical Imaging 2014: Image-Guided Procedures, Robotic Interventions, and Modeling*, Mar. 2014, vol. 9036, pp. 47–52. doi: 10.1117/12.2042483.
- [101] O. Ronneberger, P. Fischer, and T. Brox, “U-Net: Convolutional Networks for Biomedical Image Segmentation,” *ArXiv150504597 Cs*, May 2015, Accessed: Oct. 08, 2021. [Online]. Available: <http://arxiv.org/abs/1505.04597>
- [102] A. P. Twinanda, S. Shehata, D. Mutter, J. Marescaux, M. de Mathelin, and N. Padoy, “EndoNet: A Deep Architecture for Recognition Tasks on Laparoscopic Videos,”

ArXiv160203012 Cs, May 2016, Accessed: Oct. 08, 2021. [Online]. Available: <http://arxiv.org/abs/1602.03012>

[103] M. Sahu, A. Mukhopadhyay, A. Szengel, and S. Zachow, “Addressing multi-label imbalance problem of surgical tool detection using CNN,” *Int. J. Comput. Assist. Radiol. Surg.*, vol. 12, no. 6, pp. 1013–1020, Jun. 2017, doi: 10.1007/s11548-017-1565-x.

[104] X. Du *et al.*, “Articulated Multi-Instrument 2-D Pose Estimation Using Fully Convolutional Networks,” *IEEE Trans. Med. Imaging*, vol. 37, no. 5, pp. 1276–1287, May 2018, doi: 10.1109/TMI.2017.2787672.

[105] “CathNets: Detection and Single-View Depth Prediction of Catheter Electrodes | SpringerLink.” https://link.springer.com/chapter/10.1007/978-3-319-43775-0_4 (accessed Oct. 08, 2021).

[106] R. Girshick, J. Donahue, T. Darrell, and J. Malik, “Rich feature hierarchies for accurate object detection and semantic segmentation,” *ArXiv13112524 Cs*, Oct. 2014, Accessed: Oct. 28, 2021. [Online]. Available: <http://arxiv.org/abs/1311.2524>

[107] R. Girshick, “Fast R-CNN,” *ArXiv150408083 Cs*, Sep. 2015, Accessed: Oct. 28, 2021. [Online]. Available: <http://arxiv.org/abs/1504.08083>

[108] S. Ren, K. He, R. Girshick, and J. Sun, “Faster R-CNN: Towards Real-Time Object Detection with Region Proposal Networks,” *ArXiv150601497 Cs*, Jan. 2016, Accessed: Oct. 28, 2021. [Online]. Available: <http://arxiv.org/abs/1506.01497>

[109] J. Redmon, S. Divvala, R. Girshick, and A. Farhadi, “You Only Look Once: Unified, Real-Time Object Detection,” Jun. 2016, pp. 779–788. doi: 10.1109/CVPR.2016.91.

[110] J. Du, “Understanding of Object Detection Based on CNN Family and YOLO,” *J. Phys.: Conf. Ser.*, vol. 1004, p. 012029, Apr. 2018, doi: 10.1088/1742-6596/1004/1/012029.

[111] A. Varnavas, T. Carrell, and G. Penney, “Increasing the automation of a 2D-3D registration system,” *IEEE Trans. Med. Imaging*, vol. 32, no. 2, pp. 387–399, Feb. 2013, doi: 10.1109/TMI.2012.2227337.

Titre : Guidage et assistance aux procédures de radioembolisation dans le contexte de l'oncologie interventionnelle

Mots clés : Radioembolisation hépatique, guidage interventionnel, recalage 3D/2D, imagerie augmentée

Résumé : La radioembolisation est une intervention mini-invasive réalisée pour traiter le cancer du foie en administrant des microsphères radioactives. Afin d'optimiser les résultats du traitement, la procédure est réalisée en deux sessions : une intervention de prétraitement, principalement réalisée pour localiser le site d'injection, évaluer la distribution et effectuer une évaluation dosimétrique, et une intervention de traitement réalisée pour injecter la dose appropriée de microsphères radioactives dans le site d'injection localisé. En raison de la complexité de la vascularisation hépatique, les radiologues interventionnels manipulent soigneusement le cathéter, lors des deux interventions, sous guidage radiographique et recourent à l'injection de produit de contraste afin de

visualiser les vaisseaux. Dans cette thèse, nous proposons une nouvelle stratégie de guidage qui promet une simplification et une précision de la navigation du cathéter lors des deux interventions. Le système de navigation proposé traite les images préopératoires et peropératoires pour réaliser une fusion d'images grâce à une technique de recalage rigide. Cette approche est conçue pour 1) aider l'accès au tronc cœliaque, 2) aider l'accès au site d'injection et 3) reproduire le site d'injection lors de l'intervention de traitement. Sachant que le foie subit un déplacement lié au mouvement respiratoire, nous proposons également une approche qui permet d'obtenir une superposition dynamique des vaisseaux 3D projetés sur la fluoroscopie.

Title : Guidance of radioembolization procedures in the context of interventional oncology

Keywords : Liver radioembolization, interventional guidance, 3D/2D registration, augmented imaging

Abstract : Radioembolization is a minimally-invasive intervention performed to treat liver cancer by administering radioactive microspheres. In order to optimize radioembolization outcomes, the procedure is carried out in two sessions: pretreatment assessment intervention, mainly performed to locate the injection site, assess microspheres distribution and perform dosimetry evaluation, and treatment intervention performed to inject the estimated proper dose of radioactive microspheres in the located injection site. Due to the hepatic vasculature complexity, interventional radiologists carefully manipulate the catheter, during the two interventions, under X-Ray image guidance and resort to contrast media injection in order to highlight

vessels. In this thesis, we propose a novel guidance strategy that promises a simplification and accuracy of the catheter navigation during the pretreatment assessment, as well as during the treatment interventions. The proposed navigation system processes pre- and intraoperative images to achieve intraoperative image fusion through a rigid registration technique. This approach is designed to 1) assist the celiac trunk access, 2) assist the injection site access and 3) automatically reproduce the injection site during the proper intervention. Knowing that the liver undergoes a motion induced by the breathing, we also propose an approach that allows obtaining a dynamic overlay of the projected 3D vessels onto fluoroscopy.

